Modeling Of Radiative Heat Transfer In Solid Oxide Fuel Cells

Jelle Nicolaas Stam

Master Of Science Thesis

TU Delft Delft University of Technology

Challenge the future

Modeling Of Radiative Heat Transfer In Solid Oxide Fuel Cells

by

Jelle Nicolaas Stam

in partial fulfillment of the requirements for the degree of

Master of Science
in Mechanical Engineering

at the Delft University of Technology,
to be defended publicly on Wednesday 11 March, 2015 at 14:00.

Supervisors:	Prof. dr. D.J.E.M. Roekaerts,	TU Delft
	Dr. P.V. Aravind,	TU Delft
Thesis committee:	Prof. dr. ir. B. J. Boersma,	TU Delft
	Dr. ir. M. J. B. M. Pourquie,	TU Delft

Report number: 2669
AHD number: 286

An electronic version of this thesis is available at `http://repository.tudelft.nl/`.

TU Delft Delft University of Technology

ABSTRACT

Solid Oxide Fuel Cells operate at high temperatures, which places stringent requirements on the ceramic materials in these devices. Optimizing the design by thermal stress minimization could increase the life expectancy of a fuel cell. In order to do this it is important to have a detailed understanding of the heat flows and temperature profiles in SOFCs.

Because of the high temperatures it is expected that radiative heat transfer plays an important role in the thermal behavior of the cell. This phenomenon is however often neglected in SOFC modeling. Arguments often used for neglecting thermal radiation is the lack of knowledge of material properties or to save computational time. A literature study on thermal radiation in solid oxide fuel cells shows that the results from past research are not always in agreement. Some articles about radiation in the anode, cathode and electrolyte (or PEN-structure) even show completely contradictory results.

Modeling studies have been performing in multiple steps, all simulations are performed using Ansys Fluent. The SOFC models are all hydrogen fueled. To study the effects of thermal radiation in the anode, cathode and electrolyte simplified 2D representations of the PEN-structure were developed. Because the material properties are not well known the results are obtained for a wide range of optical properties, on two different geometries. The results show that in the limit of high optical thickness of the anode and cathode the entire PEN-structure can be considered opaque, which means only radiation emitting from the anode and cathode surface will be important. Thermal radiation in the electrolyte has a negligible effect on the temperature profiles in the PEN-structure.

To study the effect of surface-to-surface radiation a 2D model of a planar SOFC is developed. In this model uniform heat sources are used to account for the heat released due to electrochemical reactions and irreversibilities. Since the surface properties are not well known the temperature profiles throughout the domain are obtained for a wide range of optical properties, for both a co-flow and a counter-flow arrangement. The results show that thermal radiation has a very small effect on the temperature profiles in the domain. It was also found that the results are not very sensitive to the surface emissivities. The results are also obtained with the PEN-structure participating in radiative heat transfer, which verifies the statement that these materials can be considered opaque.

To obtain more accurate results and to check the assumption of uniform heat sources a 3D-model of a single channel planar SOFC is developed. This model is also used to study the influence of participating gases. Instead of assuming uniform heat sources the 'Fuel Cell and Electrolysis' add-on module is used to model the relevant fuel cell phenomena. The model outputs show that using uniform heat sources is not an accurate assumption. The results also show that radiation has a very small effect on the temperature profiles in the domain, and that the ratio of radiative heat flux to total heat flux is not higher than 9%. Similar to the 2D planar cell model, the results are not sensitive to surface emissitivies. The effect of participating gases is studied by considering water vapor as a participating component for the radiative transfer equation. The results show this participating gas has a negligible effect on the temperature profiles in the domain. The reason for small radiation effects is because temperature gradients are small in the direction were radiation has the most effect. Temperature gradients are shown to be dominant in axial direction, or in the direction of the flow, which is important for further studies on thermal stress minimization.

To study the effect of radiative heat transfer in a completely different fuel cell design, a 3D model of an anode supported tubular SOFC is developed. The 'SOFC with Unresolved Electrolyte' add-on module is used to model the relevant fuel cell phenomena. It is expected that radiation effects are slightly more important in this tubular SOFC model. However this model does not work optimal yet, and no results with radiative heat transfer have been obtained yet.

The results in this thesis show that radiative heat transfer in single channel SOFCs can be neglected when the temperature field has to be determined for thermal stress minimization.

PREFACE

My first real encounter with fuel cells was during the course Fuel Cell Systems. During this coarse I discovered that the solid oxide fuel cell is a very promising candidate for clean energy production. It was clear that there are still some challenges ahead before successful commercialization of this technology.

During general heat transfer courses thermal radiation is often one of the last topics of discussion. In my opinion it is also the most fascinating mode of heat transfer, which is why I choose to do an entire course specific about radiative heat transfer.

This master thesis project was a challenging opportunity to combine those two disciplines. I could not have completed this project without help from both these disciplines. I would like to express sincere appreciation to my supervisors Dirk Roekaerts and P.V. Aravind for their valuable comments and guidance during this master thesis project. I would also like to thank P.J. Coelho from Technical University of Lisbon for advising me on the use of radiation models in CFD. I am also grateful for the help of Ming Liu, who gave me advice on CFD modeling of fuel cells, and pointed me in the right direction in the first stages of my master thesis. And of course I want to thank my fellow students, for interesting conversations at the coffee machine and mutual support during each others work.

Jelle Nicolaas Stam
Delft, February 2015

CONTENTS

List Of Symbols

Roman Symbols

$\dot{m}_{cons,i}$	Net consumed mass of species i	[kg/s]
$\overrightarrow{J}_i$	Diffusive flux species i	[kg/m^2/s]
$\overrightarrow{n}$	Unit surface normal	[-]
$\overrightarrow{r}$	Position vector	[-]
$\overrightarrow{S}$	Momentum source term	[N/m^3]
$\overrightarrow{s}$	Unit vector in given direction	[m]
$\overrightarrow{v}$	Velocity vector	[m/s]
$a_{\epsilon,i}$	Emissivity weighting factor	[-]
c_0	Speed of light	[m/s]
$C_{p,i}$	Isobaric heat capacity	[kJ/kg/K]
$D_{i,m}$	Binary Diffusion coefficient	[m^2/s]
$D_{i,T}$	Thermal Diffusion coefficient	[m^2/s]
D_{ij}	Binary diffusion coefficient	[m^2/s]
D_{ij}^{eff}	Corrected diffusion porous media	[m^2/s]
E	Potential	[V]
F	Faraday constant, 96485	[C/mol]
f	Fugacity	[bar]
G	Gibbs energy	[J/kg]
G	Incident radiation	[W/m^2]
h	Planck's constant, 6.626×10^{-34}	[Js]
h	Specific enthalpy	[J/kg]
h_f	Enthalpy of formation	[J/mol]
h_i	Enthalpy species i	[J/kg]
h_{react}	Enthalpy change of reaction	[J/m^3]
I	Electric current	[A]
I	Radiative intensity	[W/(m^2 sr)]
i	Current Density	[A/m^2]
I_b	Blackbody radiative intensity (Planck function)	[W/(m^2 sr)]
$i_{0,ref}^{an/cat}$	Exchange Current Density	[A/m^2]

k_B	Boltzmann constant, 1.3806×10^{-23}	[J/K]
k_{eff}	Effective thermal conductivity	[W/m/K]
k_f	Fluid thermal conductivity	[W/m/K]
k_s	Solid thermal conductivity	[W/m/K]
$M_{w,i}$	Molecular weight species i	[g/mole]
n	Refractive index	[-]
P	Pressure	[Pa]
P_i	Partial pressure species i	[Pa]
R	Universal Gas Constant, 8.314	[J/mol/K]
R_{ohm}	Ohmic resistance	[Ωm]
$R_{solid/ionic}$	Volumetric transfer current in reaction areas	[A/m^3]
s	Radiation path length	[m]
S_h	Energy source term	[W/m^3]
S_m	Mass source term	[kg/m^{3}s]
T	Temperature	[K]
v	Velocity	[m/s]
V_{OC}	Open Cell Voltage	[V]
W	Work	[J/kg]
X_i	Mole fraction species i	[−]
$X_{i,ref}$	Reference mole fraction species i	[−]
Y_i	Mass fraction species i	[−]

Abbreviations

HHV	Higher Heating Value
LHV	Lower Heating Value
AFC	Alkaline Fuel Cell
DMFC	Direct Methanol Fuel Cell
irr-an	irreversible (anode side)
irr-cat	reversible (cathode side)
MCFC	Molten Carbonate Fuel Cell
PAFC	Phosphoric Acid Fuel Cell
PEMFC	Polymer Electrolyte Fuel Cell
PEN	Positive Electrode - Electrolyte - Negative Electrode
SOFC	Solid Oxide Fuel Cell
TPB	Triple Phase Boundary

Greek Symbols

α	Permeability	[m^2]
$\alpha_{an/cat}$	Transfer coefficient anode/cathode side	[-]
β	Extinction coefficient	[m^{-1}]
ϵ	Emissivity	[-]
ϵ	Porosity	[-]
ϵ_{LJ}	Lennard-Jones Energy Parameter	[K]
η	Wavenumber	[cm^{-1}]
$\eta_{an/cat}$	Overpotential anode/cathode side	[V]
η_{ele}	Ohmic overpotential electrolyte	[V]
γ_i	Concentration exponent species i	[-]
κ	Absorption coefficient	[m^{-1}]
Λ	Wavelength	[μm]
μ	Dynamic viscosity	[Pa·s]
Ω	Solid angle	[sr]
$\overline{\tau}$	Stress tensor	[N/m^2]
Φ	Scattering phase function	[sr^{-1}]
ϕ^0	Nernst potential at standard conditions	[V]
ϕ_{ideal}	Nernst Potential	[V]
ϕ_{ionic}	Electric potential in oxygen ion conducting materials	[V]
ϕ_{solid}	Electric potential in electron conducting materials	[V]
ρ	Density	[kg/m^3]
σ	Scattering coefficient	[m^{-1}]
σ_i	Lennard-Jones characteristic length	[Å]
σ_{ionic}	Ionic Conductivity	[1/(Ωm]
σ_{sb}	Stefan-Boltzmann constant, 5.670×10^{-8}	[$W/m^2/K$]
σ_{solid}	Electrical Conductivity	[1/Ωm]
τ	Tortuosity	[-]
$\zeta_{an/cat}$	Area to volume ratio	[1/m]

1

INTRODUCTION

There are two topics that need introduction in this thesis, namely radiative heat transfer and solid oxide fuel cells (SOFCs). The first section will introduce and give background information on solid oxide fuel cells, the section thereafter will give a brief introduction into radiative heat transfer. After introducing these topics it will be clear what the motivation is for this master thesis project. The approach and organization of this thesis is discussed at the end of this chapter.

1.1. BACKGROUND FUEL CELLS

A fuel cell is a device that electrochemically converts fuel into electric power without the need of combustion. Electricity, water and heat are the only output products for a fuel cell system running on hydrogen. In conventional thermodynamic cycles intermediate steps such as producing heat and mechanical work are necessary to produce electrical power. Because this is not necessary in fuel cells the systems are not limited by the Carnot efficiency which is the case for heat engines. Hence, fuel cells are able to deliver higher electrical conversion efficiencies when compared with traditional technologies.

There is a variety of different fuel cell types which are in different stages of development. The basic building block of a fuel cell consists of an electrolyte in contact with a porous anode and cathode layer on both sides, schematically shown in Fig. 1.1. Fuel is transported to the anode and oxygen or air is transported to the cathode. Electrons are produced on the anode side and consumed on the cathode side, resulting in a current. This principle was discovered nearly two centuries ago, the first fuel cell demonstration was by Sir William Grove ('The father of fuel cells') in 1839 [1] when he was experimenting with electrolysis and discovered that a current was created when adding the hydrogen and oxygen on opposite sides. Since then it has taken an unusually long time for this technology to be fully exploited, and this is still an ongoing process.

Fuel cell types can be subdivided according to operating temperature, type of electrolyte or the way charge is conducted. The main fuel cell types are shown in table 1.1. As shown in table 1.1 there is a large difference in operating temperature between different fuel cell types. This operating temperature is roughly determined by the choice of electrolyte [1].

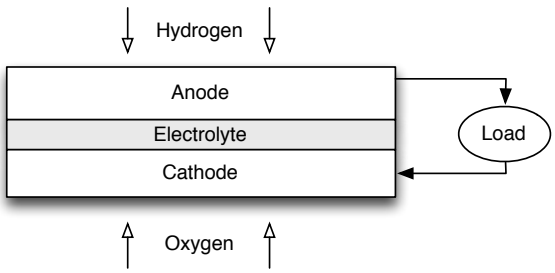

Figure 1.1: Basic working principle of a fuel cell

Table 1.1: Different types of fuel cells

Fuel Cell Type	Abbreviation	Operating Temperature	Charge Carrier	Catalyst
Proton Exchange Membrane Fuel Cell	PEMFC	$80°C$	H^+	Platinum
Alkaline Fuel Cell	AFC	$100°C$	OH^-	Platinum
Phosporic Acid Fuel Cell	PAFC	$200°C$	H^+	Platinum
Molten Carbonate Fuel Cell	MCFC	$650°C$	$CO_3^=$	Nickel
Solid Oxide Fuel Cell	SOFC	$650-1000°C$	$O^=$	Nickel, Lanthanum, etc.

The first practical hydrogen-oxygen fuel cell was of the AFC type, developed in the 1950s by Francis Thomas Bacon. Following this fuel cells were successfully developed for the American manned space program. There were substantial development programs of fuel cells in America and Japan in the 1970s and 1980s, both primarily focusing on the development of PAFCs. This resulted in considerable technical progress, but somehow these fuel cells never really became commercially viable. In the 1990s attention turned more towards PEMFCs and SOFCs. The material that laid the foundation for the SOFC electrolyte was however discovered much longer ago. This material consisting of 85%ZrO_2 and 15%Y_2O_3, the so called "Nernst Mass", was discovered by Walther Nernst in the late 1890s [2]. This Nernst Mass is a ceramic material that is able to conduct oxygen ions at high temperatures. It was an important first step in the development of solid oxide fuel cells. Focused studies on SOFCs started after pioneering work of Carl Wagner in 1943, who explained the electrical conductivity of mixed oxides. In 1962 a paper titled 'A Solid Oxide Fuel cell' was published by Westinghouse Electrical Coorporation [3], an effort which layed the foundation for Westinghouse's cathode supported SOFC. Since the 1990s interest in this type of fuel cell kept increasing.

The working principle of an SOFC is shown in figure 1.2. Oxygen diffuses from the air flow through the

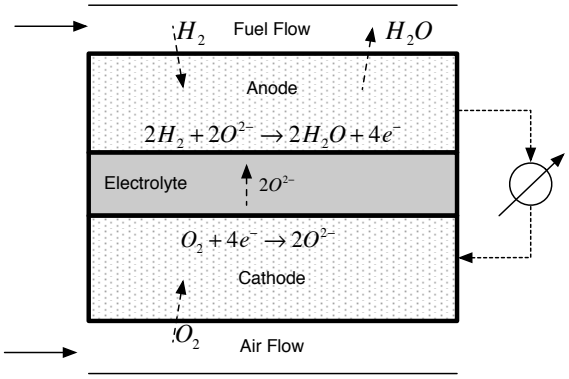

Figure 1.2: General principle of a Solid Oxide Fuel Cell (SOFC)

porous cathode and is ionized at the electrolyte. Oxygen ions diffuse through the electrolyte to the anode. At the anode side hydrogen diffuses to the electrolyte and reacts with the oxygen ions, thereby releasing electrons. These electrons flow through an external circuit back to the cathode. Depending on both fuel/air flow and electrode kinetics there will be a certain potential difference between both electrodes. When zero current is withdrawn from the cell this is called the open cell voltage (OCV). The theoretical maximum OCV is the Nernst voltage. More information on the electrochemistry can be found in appendix A.

In table 1.1 can be observed that SOFC operating temperatures are among the highest of all fuel cells, generally above 800°C. SOFCs operating in the range of 600 to 800°C are considered intermediate temperature (IT) SOFC [4]. The reason for a high operating temperature is the conductivity of the electrolyte material to oxygen ions, which increases with temperature. Currently yttrium stabilized zirconia (3, 8 or 10 percent yttria, abbreviated to YSZ) is the most commonly used electrolyte for SOFC [1]. An advantage of a high operating temperature is faster chemical kinetics, which means SOFCs don't need an expensive catalyst as platinum which is used in other fuel cell types. This gives the advantage that SOFCs can utilize CO as a fuel, which would not be possible for electrodes containing platinum. Also hydrocarbons such as methane can be utilized, in small amounts even internally reformed. The schematic in figure 1.2 shows hydrogen as example but

SOFCs allow conversion of a wider range of fuels, including various hydrocarbon fuels [1]. One disadvantage of the high operating temperatures is thermal stresses, which among other things causes the need for a very long start-up time.

1.1.1. HEAT SOURCES

Both air and fuel stream are preheated to prevent low temperature areas in the fuel cell system. Within the fuel cell a lot of heat is generated due to different mechanisms. Heat is released due to electrochemical reactions and irreversibilities. In all conducting materials joule heating will occur, due to resistance against the flow of charge carriers. This is sometimes called ohmic polarization.

The actual potential difference between the electrodes is lower than the ideal potential difference. This is caused by overpotential, a necessary deviation from the ideal potential to drive the electrochemical reactions. This means the actual work is lower than the ideal work , so more heat is generated. This effect is sometimes referred to as activation polarization.

Another irreversible loss is due to so called concentration overpotential. This means that the reaction rate is faster than the rate with which the species can diffuse to and from the reaction sites. In other words, the reactions are diffusion-limited. Since this will decrease the ideal work expected from the cell, even more at increasing current densities, this effect must be correctly accounted for.

1.1.2. DESIGN

The electrolyte material is generally YSZ, which consists of a crystal structure of zirconium oxide which is made stable by addition of yttrium oxide. This material has a low electron conductivity and good oxygen ion conductivity at high temperatures. The materials for both anode and cathode must have a high electrical conductivity. The combination of anode, cathode and electrolyte is often referred to as PEN-structure (Positive Electrode - Electrolyte - Negative Electrode). Electrochemical reactions take place at the 'triple phase boundaries', abbreviated to TPBs. These reaction areas are called this way because three materials must be in contact for the reactions to occur. These materials are the anode or cathode, the electrolyte material and the reacting gas components. To minimize thermal stress it is important that the thermal expansion coefficients of the anode, cathode, electrolyte are similar to each other. Typically the anode is a Ni – YSZ cermet, a composite material of nickel and YSZ particles. For cathodes mostly lanthanum-based perovskite materials are used, for high temperature SOFCs Sr-doped $LaMnO_3$ is the most common material [4].

The current collectors, or interconnectors, connect the fuel cell to an external circuit. Interconnect materials can be conductive ceramic materials for high temperature operation (900 to 1000°C) or metallic alloys for lower temperature operation. The thermal expansion coefficients of the current collector and anode/-cathode electrode must also be similar to each other. The shape of these components depends heavily on the fuel cell design. A schematic of a cathode supported tubular SOFC is shown in 1.3. This schematic is based on the cathode supported tubular SOFC of Siemens Westinghouse. The cathode is on inner side of the cylinder,

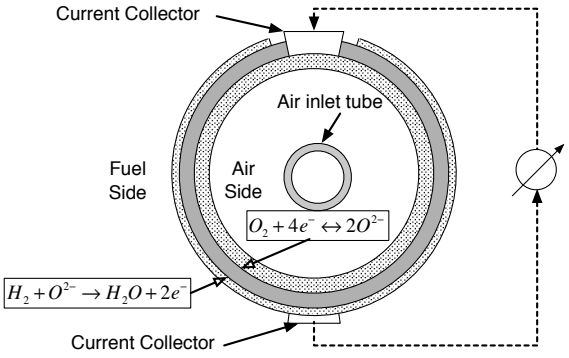

Figure 1.3: Cross section tubular SOFC

with an layer of electrolyte and anode on the outside. The advantage of this design is that there are no sealing problems, and the cells can easily be connected parallel or in series. One of the major disadvantages is the long current path of the electrons, which can result in high ohmic losses.

Another popular design is the anode supported planar SOFC, of which a schematic is shown in figure 1.4. The figure shows that the current collectors enclose the flow channels in this design. This design has short

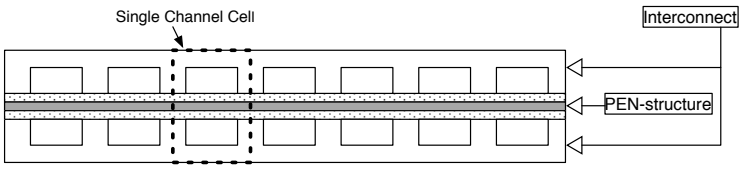

Figure 1.4: Planar SOFC unit

current paths, and the cell is easier to fabricate. Another advantage is that the current density of planar cells is much higher than that of tubular cells. The biggest disadvantage is that this cell needs high temperature sealing materials to separate the fuel from the oxidant. More advantages and disadvantages of both designs can be found in literature. A review article on mathematical modeling of SOFCs by [5] summarizes some of the important pro's and con's.

In technical development of SOFCs low cost materials and fabrication are key challenges. For this it is important to have an optimal design first. One way of optimizing the design is by focusing on minimizing thermal stresses in the ceramic materials. From literature it is known that thermal stresses can be an important problem in SOFCs [6, 7]. In Nakajo et al. [7] it is mentioned that lack of knowledge of mechanical material properties as well as uncertainties about the phenomena occurring in the cell is a limitation in determining thermal stresses accurately. To minimize thermal stresses, it is important to have detailed knowledge about heat flows and temperature profiles in the systems. Because of the high temperatures it is expected that radiative heat transfer will play an important role here, in addition to heat transfer by conduction and convection.

1.2. BACKGROUND RADIATIVE HEAT TRANSFER

There are three fundamental modes of heat transfer; conductive, convective and radiative heat transfer. Heat transfer by thermal radiation is highly non-linear, whereas conductive and convective heat transfer in ideal cases scale linear with temperature. Conductive heat transfer is described by Fourier's law, which shows the amount of heat transferred is equal to a thermal conduction coefficient times the temperature gradient in the medium. This is schematically shown in figure 1.5a. Convective heat transfer is caused by the movement of a

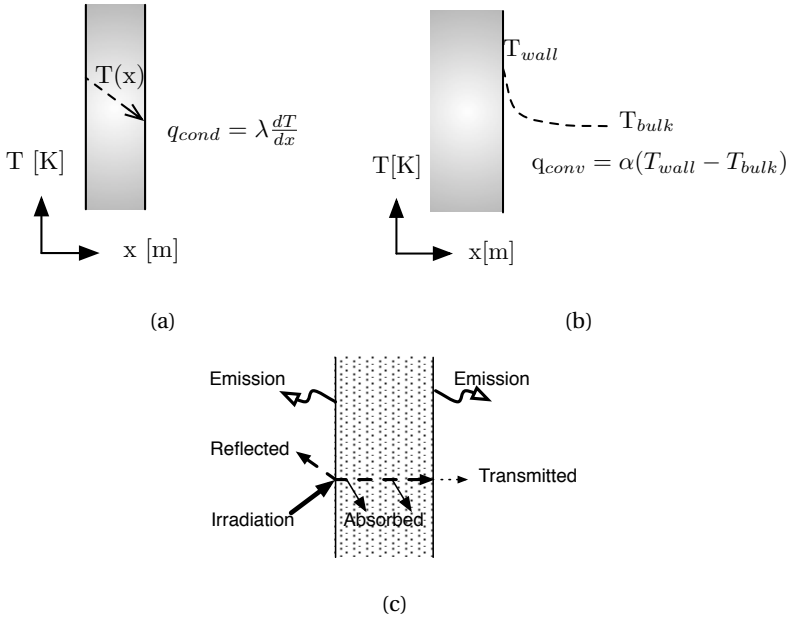

Figure 1.5: The three fundamental modes of heat transfer. (a) Conductive heat transfer. (b) Convective heat transfer. (c) Radiative heat transfer.

fluid along a certain medium. A thermal boundary layer will develop at the surface and according to Newton's law the heat transfer can be described by determining a heat transfer coefficient and multiplying it with the temperature difference between the wall and the bulk temperature. This is shown in figure 1.5b. This heat transfer coefficient and the conduction coefficient can be a function of temperature. Since this dependence is not very strong it is often said that conductive and convective heat flow are linear proportional to temperature difference. This makes these phenomena easy to work with when developing a model.

Radiative heat transfer or thermal radiation is the science of heat transfer caused by electromagnetic waves. Electromagnetic waves, or photons, may travel over a long distance without interacting with a medium, which makes it of great importance at vacuum or space applications [8]. In figure 1.5c heat transfer by radiation is schematically shown. Irradiation is all the radiative energy reaching the surface. A part of this energy can be reflected at the surface, it can be absorbed in the material, and what is left is transmitted trough the material. The material itself will also emit radiation in all temperatures. The energy emitted by a black surface bounded by a transparent medium with refractive index n, the *blackbody emissive power*, known as *Plank's law*, is given by

$$E_{b\lambda} = \frac{C_1}{n^2\lambda^5\left[e^{C_2/(n\lambda T)}-1\right]}\,. \tag{1.1}$$

Where the constants C_1 and C_2 are given by:

$$C_1 = 2\pi hc_0^2 = 3.7419\times10^{-16} \quad [\mathrm{Wm}^2] \tag{1.2}$$

$$C_2 = \frac{hc_0}{k_B} = 14388 \quad [\mu\mathrm{mK}] \tag{1.3}$$

The total emissive power of a black body can be obtained by integration of Plank's law over all frequencies, resulting in:

$$E_b(T) = n^2\sigma_{sb}T^4. \tag{1.4}$$

With $\sigma_{sb} = 5.670\cdot10^{-8}\left[\frac{W}{m^2K^4}\right]$, which is the Stefan-Boltzmann constant. Unlike conduction and convection, radiation shows a strong non-linear relation with temperature. From equation (1.4) can be concluded that the role of radiative heat transfer becomes more and more important as temperature increases.

Not all surfaces have the blackbody emissive power distribution given by Plank's law. The emitted radiation can be dependent on a number of surface properties, which describe deviations from blackbody behavior. The most basic radiative property of a surface is the emittance, which represents the ratio of actual emission compared to black body emission. Another property is the absorptance, which describes the fraction of the irradiation that is absorbed. A more complicated one is the reflectance of a surface, which is the fraction of the irradiation that is reflected. These properties can be dependent on direction of the radiation beam, on wavelength, temperature and location on the surface. For reflectance both the incoming and outgoing direction can be variables.

It becomes even more complicated when there is a gaseous or liquid medium enclosed by walls which is 'participating' in radiative heat transfer. An energy balance along a beam of radiation in a participating medium is described by the radiative transfer equation. This energy balance will be described in more detail in the model description. For most cases there is no analytical solution to this equation, but there are numerous numerical solution methods. Be that as it may, even with a numerical solution method there still exists the problem of accurately approximating material properties (absorption coefficient, scattering coefficient). Radiative properties can be difficult to measure and often display very complicated behavior. A large computational time or not having accurate properties available are often used as argument for neglecting thermal radiation in heat transfer problems.

1.3. RESEARCH FOCUS

The high operating temperature places stringent requirements on the ceramic materials in solid oxide fuel cells. Optimizing the design by thermal stress minimization could increase the life expectancy of a fuel cell. In order to achieve this it is important to have a detailed insight in the heat flows and temperature profiles in SOFCs. Including thermal radiation in a SOFC model can increase the computational time by many orders of magnitude. This research will show what the consequences are of neglecting this phenomenon in fuel cell models, which will help in making decisions in future SOFC modeling.

This research will show what effect thermal radiation has on temperature profiles, heat flows and fuel cell performance. Since optical properties show very complicated behavior is it important to know which

properties are actually important, and which properties have little influence on the modeling results. For thermal stress minimization it is important to know where high temperature gradients occur in the cell, and how these gradients are influenced by thermal radiation.

Different phenomena will be investigated, surface to surface radiation, the effect of participating gases, and the effect of radiation in porous media. This is done by developing fully functional SOFC models including thermal radiation. To show the effects of thermal radiation the model computations are also made neglecting radiation.

1.4. OUTLINE OF THIS THESIS

A literature study of past research on radiative heat transfer in solid oxide fuel cells is included in chapter 2. The conclusions from this literature study are used for the modeling approach applied in this thesis.

The modeling approach that is chosen is presented in chapter 3, the complete system of equations necessary to mode solid oxide fuel cells is discussed here.

Chapter 4 shows the development of simplified 2D SOFC models to study the effects of radiation in the PEN-structure and the effect of surface-to-surface radiation.

Chapter 5 shows the development of a complete 3D single channel SOFC model using the 'Fuel Cell and Electrolysis' add-on module. This model is used to obtain more accurate results considering radiation, and to show the distribution of different heat sources.

Chapter 6 shows the development of a complete 3D tubular SOFC using the 'SOFC with Unresolved Electrolyte' module. This model can be used in future research to show the effect of radiative heat transfer in this type of fuel cell design.

In chapter 7 the conclusions of this research are presented and recommendations are made for future research.

2

LITERATURE REVIEW

2.1. INTRODUCTION

Before developing any models a literature study is performed to determine what already has been found in the past on radiative heat transfer in fuel cells. Numerous articles where found that include thermal radiation in their SOFC study. Some articles show the effect of thermal radiation on temperatures and fuel cell performance, while other mention that it is included but do not discuss the effects of it at the conclusion. The two most common SOFC designs were discussed in the introduction(chapter 1), namely the tubular and planar design. These different designs and the combination of different modeling strategies can make it difficult to compare results from literature. The conclusions obtained from different model strategies and fuel cell designs are presented here as clear as possible.

First the influence of radiation in the PEN-structure will be discussed. This concerns radiation in the electrolyte and in the porous anode and cathode. This is followed by a discussion on surface-to-surface radiation in different SOFC designs. The section thereafter will discuss the influence of participating gases. This literature study is concluded by showing the influence of radiative heat transfer to the surroundings on an entire fuel cell stack.

2.2. THERMAL RADIATION IN THE ELECTRODE-ELECTROLYTE ASSEMBLY

Both the anode and cathode are generally 40-50% porous which means thermal radiation could be scattered in and out of those layers. A cross section of the PEN-structure of a Siemens Westinghouse cell is shown in figure 2.1. There are several studies which specifically focus on radiative heat transfer in porous layers and characterization of radiative properties in those materials [9–13]. In Rubiolo and Gatt [10] a model is devel-

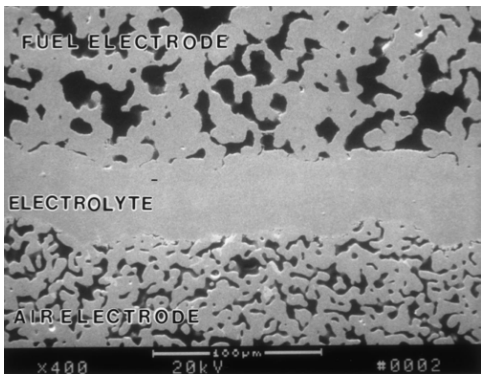

Figure 2.1: Microstructure of a cross-section of a Siemens Westinghouse cell [14]

oped to capture thermal radiation in a porous material composed of spheres of cylinders. From figure 2.1 can be concluded that this might not be a good approximation to capture the porous materials in SOFCs.

The model developed in this study captures thermal radiation effects accurately for highly porous materials, which is not the case here. In Taine et al. [11] it was shown that most porous media do not show 'Beerian' behavior. This means radiation is not attenuated exponentially according to Beer's law. In this article a generalized radiative transfer equation (GRTE) is developed based on an extinction cumulative distribution function, absorption and scattering cumulative probabilities and the scattering phase function established for this optical thickness range. These properties are determined by Monte Carlo simulations of a detailed geometry. Before developing such advanced and complicated models to capture thermal radiation in porous media correctly a qualitative analysis is necessary to determine whether this is necessary in the anode and cathode material.

From past research on thermal radiation in the anode, cathode and electrolyte it can be concluded that generally more simple models are used to approximate radiative heat transfer. Radiation in the anode, cathode and electrolyte is however often neglected. This is because the materials properties are not well known, because the materials are assumed to be optical thick or to save complexity from the fuel cell model. Three articles where found that specifically focus on thermal radiation in the electrodes and electrolyte[15–17].

The electrolyte material, YSZ, is not porous like the anode and cathode. Currently this material is the most commonly used material for the SOFC electrolyte[1]. The optical properties of this material are much better characterized than the anode and cathode materials. The reason for this is that YSZ is also used as a thermal barrier coating on gas turbine blades [18]. The material properties show that the electrolyte layer in SOFCs can be considered optical thin.

In a study by Murthy and Fedorov [15] a monolith type fuel cell model is used to study thermal radiation in the PEN-structure. Both the anode and cathode have an optical thickness of 10^4, and are 2500 μm thick. The electrolyte has an optical thickness of 0.25 and is 500 μm thick. Radiation is modeled using the discrete ordinates method. The results are compared with a simplified radiation model where the Rosseland approximation is used in the electrodes and Schuster-Schwarschild in the electrolyte. These approximations reduce the computation time considerably but have their limitations. The Rosseland approximation holds only for optical thick materials, and the Schuster-Schwarzschild approximation is a method that can be used for optical thin materials. A considerable temperature difference is found between the no-radiation and the

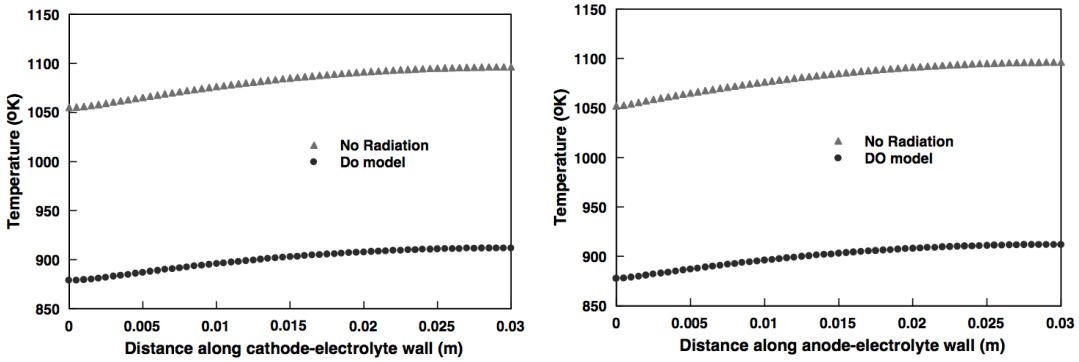

(a) Cathode/Electrolyte Interface

(b) Anode/Electrolyte Interface

Figure 2.2: Temperature profiles on electrode-electrolyte boundaries along flow path length. Anode, cathode and electrolyte are participating and the radiative transfer equations is solved using the discrete ordinates (DO) method. (Murthy and Fedorov [15])

radiation model. From the results in this article is concluded that radiation cannot be neglected in the PEN-structure. However, from this study is not clear what the contribution of each material is, or how sensitive these results are to optical properties and temperature.

In a study by Damm and Fedorov [17] a CFD-model of a single channel planar SOFC is used to show the effect of thermal radiation in the electrolyte material. Both electrodes are considered opaque. This assumption is based on optical measurements done on 200 [μm] thick layers of Ni – YSZ and LSM at room temperature. It is of course questionable if these optical properties also hold for the elevated temperatures encountered in SOFCs, they can have a strong temperature dependence. The absorption coefficient of YSZ was determined using transmissivity and reflectivity data obtained from optical measurements done on a 330 [μm] layer of polycrystalline YSZ at room temperature. Radiative heat transfer in the electrolyte is implemented using the Schuster-Schwarzschild approximation, with 3 spectral bands to account for non-gray behavior, which are

given by:

$$\kappa_{electrolyte} = \begin{cases} 160\ \text{cm}^{-1} \text{ for } 0.0 < \lambda < 3.5 \\ 110\ \text{cm}^{-1} \text{ for } 0.0 \leq \lambda < 3.5 \\ 50\ \text{cm}^{-1} \text{ for } 0.0 \leq \lambda < \infty \end{cases} \tag{2.1}$$

In each respective band these values give an optical thickness of 0.24, 0.165 and 0.075, for a 15 [μm] thick electrolyte. This is implemented in commercial CFD-package Ansys Fluent. Temperature profiles along the flow channel are shown in figure 2.3. The anode and cathode are considered opaque, the solution with thermal

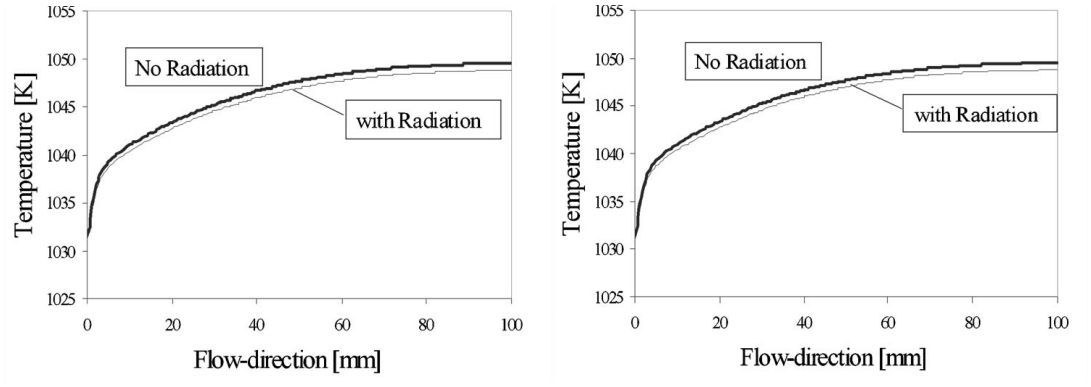

(a) Anode/Electrolyte Interface (b) Cathode/Electrolyte Interface

Figure 2.3: Temperature profiles with/without radiation along the flow channel of a single channel planar SOFC. Only the electrolyte material is participating in radiation, inplemented using Schuster-Schwarzschild with 3 spectral bands (Damm and Fedorov [17])

radiation is compared to the solution without thermal radiation. From the results it can be concluded that thermal radiation in the electrolyte has a very small effect on the temperature profile along the flow channel.

In a study by Daun et al. [16] a 2D planar SOFC model is developed to study thermal radiation in the PEN-structure. In Damm and Fedorov [17] the electrolyte was modeled as a non-porous layer, but in Daun et al. [16] however the layer is considered to be 6% porous YSZ. The optical properties of YSZ are obtained by applying a four-flux to to spectral reflection and transmission data at 1000K. The Planck mean absorption and scattering coefficients at 1000K are 260 [m^{-1}] and 1×10^4 [m^{-1}]. The optical properties of the anode and cathode material are determined analytically and shown in figure 2.4. These values give a mean penetration

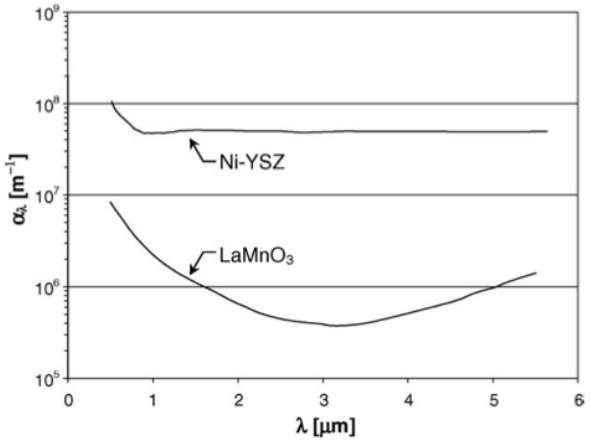

Figure 2.4: Spectral anode and cathode absorption coefficients [16]

distance of 2 [μm] for the cathode and 2 [nm] for the anode. This leads to the assumption that radiation can be neglected in those layers. Only thermal radiation in the electrolyte is left in the model. The results from this article are shown in figure 2.5. The results show that radiation in the electrolyte has very small effects on the temperature profiles in the PEN-structure, similar to the results from Damm and Fedorov [17].

The three articles discussed here all looked at planar SOFC configurations. The electrodes where either considered with high optical thickness or opaque. The electrolyte is shown to be optical thin. The results

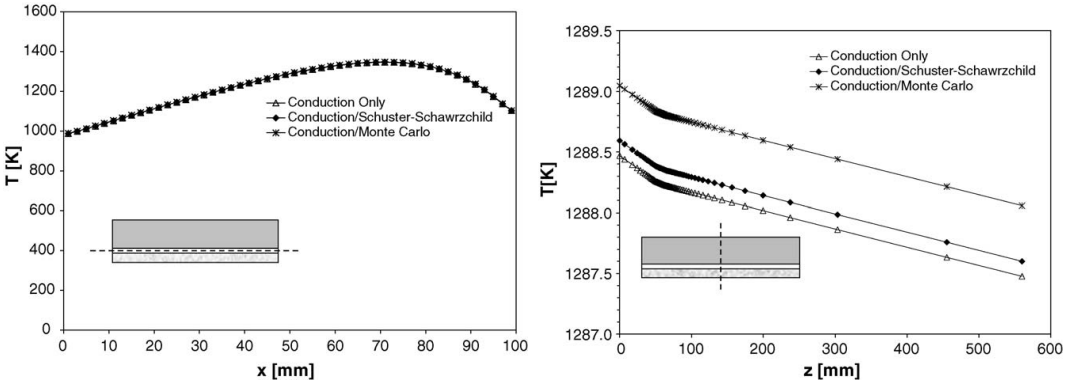

(a) Temperature profile in electrolyte (b) Temperature profile along vertical midplane

Figure 2.5: Temperature profiles in PEN-structure in both x and y-direction. Only radiation in electrolyte included using Schuster-Schwarzschild approximation (Daun et al. [16])

are however contradictive. The models that only consider the electrolyte as participating found that thermal radiation in this material can be neglected. In the model by Murthy and Fedorov [15] also the anode and cathode are participating media, optical thick, and a large temperature difference was found in the PEN-structure when including radiation. It is necessary to study radiation in the PEN-structure in more detail to understand what is happening.

2.3. SURFACE-TO-SURFACE RADIATION IN SOFCS

Surface-to-surface radiation is in many cases the most important form of radiative heat transfer. High temperature differences between walls can cause large heat flows. When there is no particating medium between those walls, the problem can be solved by calculating so called 'view factors' which give the proportion of radiation that leaves surface A and strikes surface B. This is where the geometry of the fuel cell can have an interesting effect on the heat flows, since the geometry of a tubular cell is completely different than a planar cell.

When determining surface-to-surface radiation, it is important to know the optical properties of the relevant surfaces. In all encountered articles the relevant surface where assumed to be 'grey', which means the properties are independent of wavelength. The surface properties used in literature are often assumptions. Assumed emissivity values found in literature for the cathode surface are listed in table 2.1. None of the arti-

Table 2.1: Emissivity cathode surface from literature

Emissivity ε_{cath}	Reference
1	[19]
0.9	[16, 20–25]
0.8	[26]
0.7	[27]
0.55	[28]
0.35	[29]

cles in this table justify where these material properties are based on. Some anode emissivities encountered in literature are shown in table 2.2. Only three values are shown here, but again they are far apart. The list of cathode surface emissivities is much longer, the reason for this is that most articles discussed here focus on tubular SOFCs. Tubular SOFC models that include radiation often only include it at the cathode side. For the planar configurations the surface properties of the interconnect material will also play an important role, since both flow channels are enclosed by this material. First articles on planar SOFCs will be discussed, followed by articles on tubular SOFCs.

Table 2.2: Anode surface emissivities

Emissivity ε_{an}	Reference
1	[19]
0.9	[16]
0.55	[28]

2.3.1. PLANAR SOFCS

The planar configuration was already discussed in the introduction. The fuel channel is enclosed by anode material and the current collector, the air channel by the cathode material and the current collector. In Damm and Fedorov [30] a general discussion is conducted about radiation in both planar and tubular SOFCs. From this discussion is concluded that radiation must be included in the flow channels, and that the walls can be assumed opaque, gray and diffuse. This article mentioned that the absence of optical properties makes the problem more difficult, because the properties of both anode and cathode can show much more complex behavior than a simple gray-surface assumption.

In an article by VanderSteen and Pharoah [31] a model is developed of a single channel planar SOFC to show both the effect of surface-to-surface exchange and participating gases. This model only focuses on the anode side of the planar cell, and a uniform heat source of 1900 [W/m^2] is applied at the anode surface. This is of course a debatable assumption, but even with this simplification it was found that including surface-to-surface radiation lowers the overall temperatures with approximately 30 [K].

In DiGiuseppe [28] the effects of radiation in the flow channels are studied. Due to lack of optical properties, the surface emissivity of both anode and cathode are assumed to be 0.55, based on the surface emissivity of aluminum. The emissivity of the current collectors are assumed to be 0.3. The results from this analysis are shown in figure 2.6. The figure on the left shows the temperature profiles obtained without radiation, plotted for different cell voltages. The figure on the right shows the temperature profiles when surface-to-surface radiation is included. It is clear from this figure that including radiation changes the temperature profile and lowers the overall temperatures. To show the effect of the surface emissivity the problem is also solved with cathode and anode emissivities of 0.01. The results shown in Fig. 2.7 show a slight change in temperature profiles, but the results are very similar to the results with emissiviy 0.55. The results from this article are

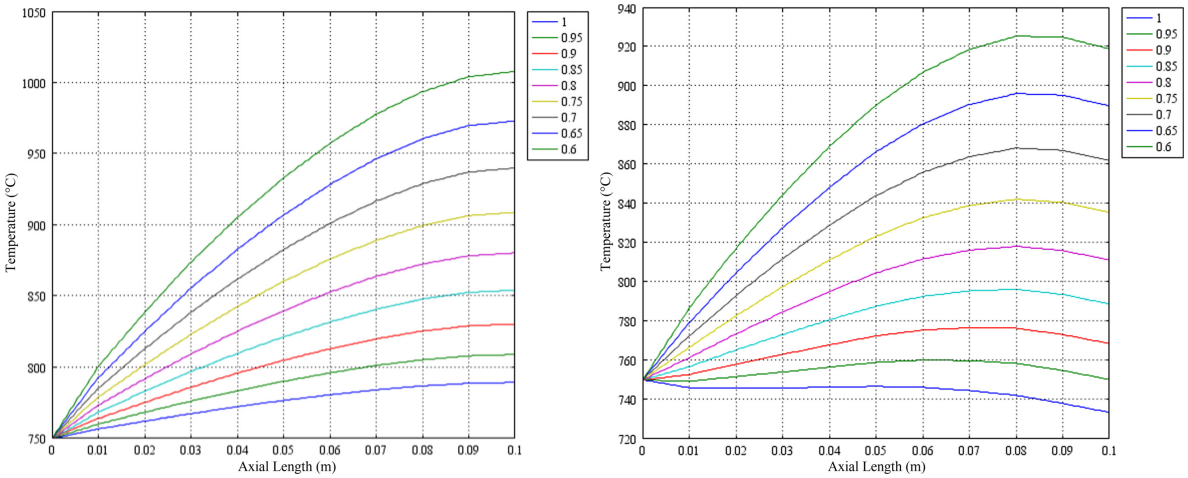

(a) (b)

Figure 2.6: (a) Temperature profiles without surface-to-surface radiation. (b) Temperature profiles with surface-to-surface radiation, anode and cathode emissivities 0.55. These temperature profiles are plotted along anode/electrolyte interface for different cell voltages. [28]

very interesting, a temperature peak occurs when including radiation. The solution is not very sensitive to surface emissivity. The emissivities that where used are however relatively low, the effect of a higher surface emissivity is not shown in this analysis.

In Qu et al. [24] a 3D CFD-model is developed of a single channel planar SOFC. Including surface-to-

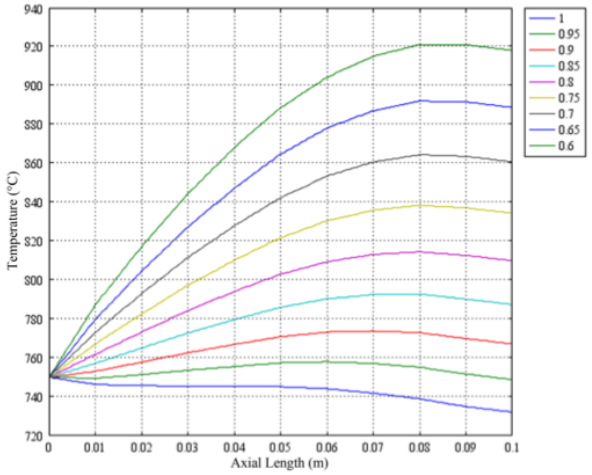

Figure 2.7: Temperature profiles with anode and cathode emissivities 0.01. Temperature plotted at anode/electrolyte interface at different cell voltages. [28]

surface radiation lowers the overall temperatures in the domain by approximately 8 [K]. The question is if this temperature difference is important enough to go through the efforts of modeling radiative heat transfer.

2.3.2. TUBULAR SOFCS

There are numerous articles that focus on the cathode supported tubular SOFC with an air injection tube. This design is based on the Siemens Westinghouse SOFC, and this is also the tubular design mentioned in the introduction chapter of this thesis. A schematic cross-sectional view of this design is shown in figure 2.8. Air

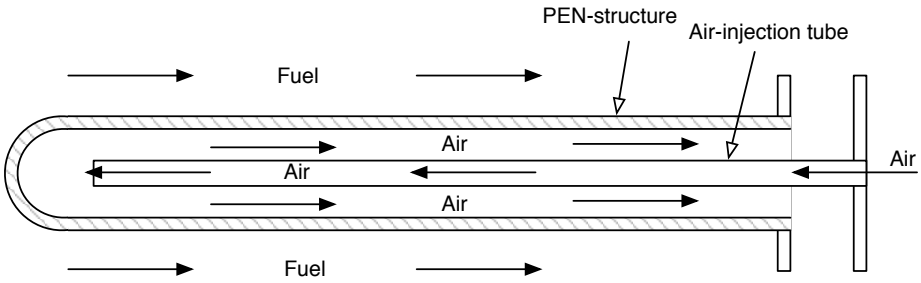

Figure 2.8: Cross section of a cathode supported tubular SOFC

enters through the injection tube, reverses direction and flows to the exit along the cathode surface. This tube is necessary because the fuel cell has a closed end, but a useful function is that it preheats the air. Radiation between the cathode surface and the injection tube surface is often modeled.

In an article by Hirano et al. [32] a tubular SOFC model is developed. In this article it is stated that convective heat transfer is more important than radiative heat transfer, concluding that it can be neglected. The model is based a cell design of Siemens Westinghouse, and the predicted temperature profiles from the model match the experimental measurements excellent. In Bessette et al. [20] for also a tubular SOFC is modeled, this time including radiation between the cathode surface and the air injection tube. All surface emissivities are assumed 0.9, and the results from this article also show excellent agreement with the experimental data of Siemens Westinghouse. There are many different phenomena occurring in SOFCs and different assumptions that influence the solution. It is difficult to know which is these two articles are more accurate.

In Hajimolana et al. [33] a tubular SOFC model is developed with as main focus the influence of participating gases at the fuel side on the temperature profiles. At the cathode side surface-to-surface is included between the air injection tube and the cathode. The consequence of neglecting this is however not discussed in the results. This is also the case in an article by [25]. Surface-to-surface radiation is included between the cathode and the air injection tube, with both surface emissivities 0.9, but the effect is discussed in the results.

In Calise et al. [27] the effects of surface-to-surface radiation are determined in again a similar tubular SOFC design. The emissivity of both the cathode surface and the air injection tube are assumed to be 0.7. The temperature profiles in the PEN-structure are shown with and without radiation in figure 2.9. The re-

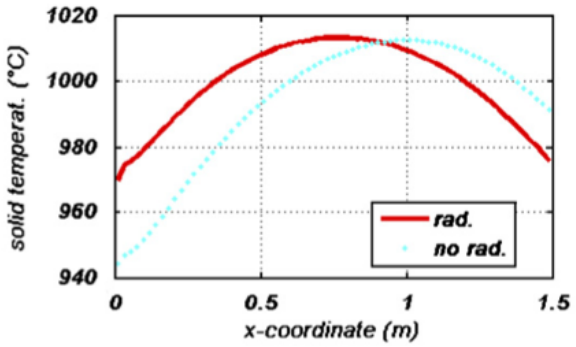

Figure 2.9: Temperature profile in "lumped" PEN-structure along axial direction with and without radiation[27].

sults show that the temperature peak shifts, and that the temperatures at the beginning and end of the tube are significantly different. When performing a thermal stress analysis the effect of thermal radiation on the temperature profiles can not be neglected.

In Haynes and Wepfer [34] the effect of surface-to-surface radiation between cathode and air injection tube is studied. In this study the materials are assumed to be isothermal in axial direction. This is a very questionable assumption, which does not seem appropriate when looking at the previous discussed results. The results obtained from this analysis are shown in figure 2.10. The amount of heat transferred due to radia-

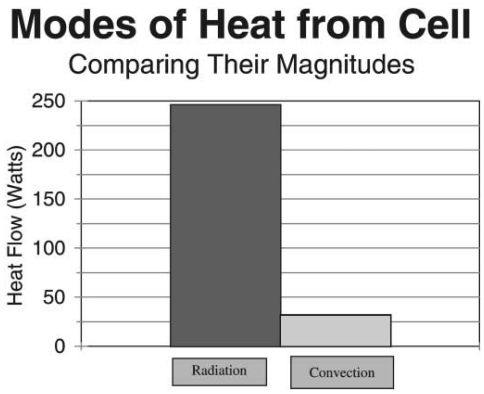

Figure 2.10: Convection and radiation magnitudes at fuel cell inner surface [34]

tion and convection are shown in this graph. The magnitude of thermal radiation is dominant over convective heat transfer, but as mentioned the modeling assumptions are very questionable.

2.4. PARTICIPATING GASES

In a hydrogen fueled SOFC the two components at the anode side are hydrogen and water vapor. When also utilizing carbon monoxide as a fuel there will also be carbon dioxide in this stream. Both carbon dioxide and water vapor are known to be participating media when considering thermal radiation. This means these components could have an influence on temperature values in fuel cells. The effect of participating gases on the anode side has been studied in different articles. The effect of participating gases on the cathode side is considered negligible in all articles.

In Damm and Fedorov [30] is discussed how participating gases should be treated in fuel cell channels. In this article a simple analysis using the Planck-mean absorption coefficient is performed to determine the optical thickness of the gas components. These obtained properties are shown in table 2.3. Using a distance of 5 [mm] in the fuel channel it was found that the optical thickness for a typical fuel stream composition is

Table 2.3: Spectrally averaged absorption coefficient for gas components at 600°C REF.

Species	Absorption coefficient [$cm^{-1}bar^{-1}$]
H_2O	0.1
CO_2	0.3
CO	0.3
CH_4	0.4

lower than 0.1 at atmospheric pressure. This leads to the conclusion that the influence of participating gases can be neglected.

In Hirano et al. [32] is discussed that all the relevant gas components are nearly transparent in the IR-region and therefore negligible. Also it is assumed that convective heat transfer is much larger than radiative heat transfer which is why radiation is completely neglected in the developed model. This assumption is however not validated.

These articles concluded that the components at the fuel side can be considered optical thin, and do not have to be included in the radiation problem. In Hajimolana et al. [33] participating media is included in a 0D dynamic tubular SOFC model. The effects of participating gases on the overall fuel cell temperature is determined here. Fuel components H_2O, CH_4, CO and CO_2 are taken into account, and the optical properties are determined using the weighted sum of gray gases model (WSGGM). The obtained results are shown in figure 2.11. Figure 2.11a shows the effect of participating media on the average cell temperature as function

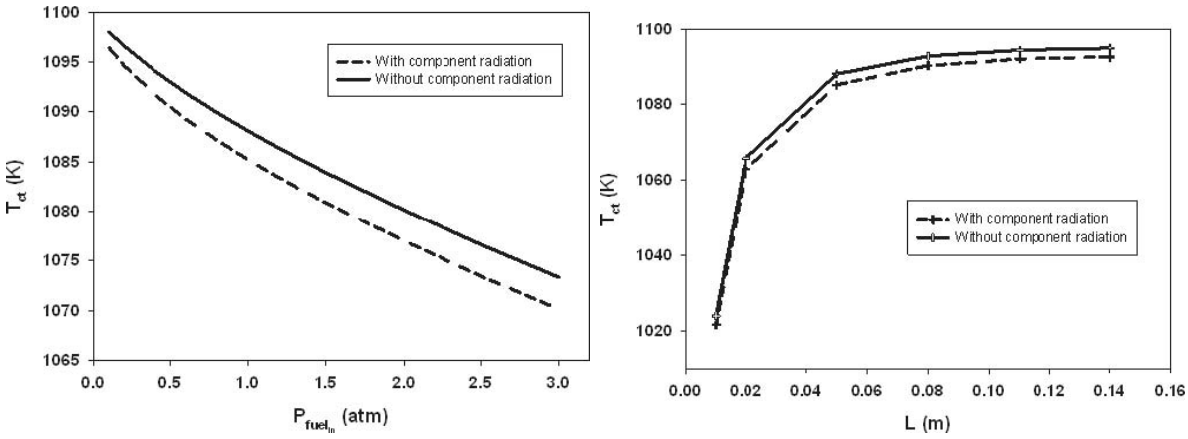

(a) (b)

Figure 2.11: (a) Cell-tube temperature with and without participating media, as function of inlet fuel flow pressure. (b) Cell-tube temperature with and without participating media, as function of the fuel cell length.[33]

of operating pressure, figure 2.11b shows the effect as function of tube length. In both these figures a small temperature difference can be noticed. The effect is small in this 0D model, but it might be more significant in a model with more dimensions.

The article by VanderSteen and Pharoah [31] was shortly discussed in the previous section. The effect of participating gases is also taken into account in this article. The model considered here is based on a single channel planar cell. Only the gas components on the anode side of the cell are taken into account. The components H_2O and CO_2 are modeled using a parametric gray gas model, assuming a partial pressure of 0.20 atm and a temperature of 1200K. Scattering of radiation is neglected. Including surface-to-surface radiation lowers the overall temperatures, but including the participating media has negligible effect. In the conclusions is mentioned however that in a tubular system, with a higher mean beam length, or at higher operating pressures, the effect might not be negligible.

In Sanchez et al. [25] among other goals the influence of participating media on fuel cell performance is researched. This model is based on a cathode supported tubular SOFC. Only the components CO_2 and H_2O are considered. Hadvig's analytical method is used to calculate the emissitity of the gas mixture. Emissivity and absorptivity of the gas depend on its composition, temperature and on the geometry of the duct through mean beam length. Concluded is that for low current density the effects of the participating gas are negligible

on the fuel cell current density and temperature. For high current density the performance is only 1% lower when including the anodic gas. The results show however that the mean temperature decreases from 903°C to 599°C. This temperature difference is remarkably high, and is not discussed in the conclusion. This leads to wonder if it might be an error in the results.

2.5. HEAT LOSS TO SURROUNDINGS

When looking at a single channel fuel cell often adiabatic boundary conditions are assumed, which physically could be interpreted as the cell being positioned in the middle of a stack. When simulating a complete stack the system boundary cannot be assumed adiabatic anymore. The temperature difference between the outer wall of the stack and the surroundings can be quite large, which means heat losses will be important for the thermal management of the stack. Because it is desirable that the cells operate at a similar temperature, studying the heat loss to the surroundings is important for designing fuel cell stacks.

In Achenbach [35] the effect of stack heat losses on the temperature distribution in the stack is determined. This articles concludes that an extremely effective thermal insulation is necessary to protect the stack from cooling out, which means these heat losses have a strong effect on the temperature distribution in the fuel cell stack. It is clear that radiative heat transfer losses from the stack are important.

In Tanaka et al. [36] the influence of thermal radiation from the stack to the surrounding on temperature profiles in the stack is investigated. In this article a planar SOFC stack is surrounded by other stacks contained in an isolating vessel. A single stack is modeled by assuming an ambient temperature surrounding it. Numerical simulations are performed for an ambient temperature of 1073 [K] and 1273 [K]. The results are compared with corresponding results in which the authors model only one cell. It is concluded that radiative heat transfer from the stack to the surroundings cannot be neglected.

2.6. CONCLUSIONS

Radiation in different fuel cell components was discussed in the previous sections. First radiation in the PEN-structure was discussed. In literature is assumed that the anode and cathode are optical thick and the electrolyte optical thin. There where 2 articles that modeled radiation in only the electrolyte and the results show that the effect on temperature profiles is negligible. There was however one article that also included radiation in the anode and cathode, and showed a considerable effect on the temperature profiles. The conclusion from this article is that radiation in the PEN-structure is non-negligible. Since the conclusions from these articles are not in agreement this has to be studied in more detail.

It appears that surface-to-surface radiation has a strong effect on the temperature distribution in SOFCs. This effect was particular strong in tubular SOFCs. There is a strong variation in optical properties used in literature. A more detailed study must be done to show the effect of these optical optical properties. A sensitivity analysis ranging from the lowest to the highest values will show how important these properties are. The results will show whether it is necessary to perform optical measurements on these materials.

The effect of participating gases is neglected in most literature. The articles that include it show a slight change in temperatures. Because these effects where obtained from 0D or 1D models, it might have a stronger effect in a complete 3D model. Concluding, the effects of participating gases must also be studied in more detail. Increasing the operating pressure increases the density and thus the optical depth of these gases.

The effect of thermal radiation will become less strong at lower operating temperatures. It is useful to know below which temperature radiative heat transfer can be considered negligible in SOFCs.

3

MODELING APPROACH

The motivation for this research is clear, and the literature study showed which areas need attention. On the basis of this, the present chapter will describe the modeling approach which is then applied in the following chapters.

3.1. MODELING APPROACHES

When developing a model the first step is to define it's goal, and to clearly identify which input and output variables are important, and which internal variables are of interest.

For this research one of the most interesting output variables is temperature. For design optimization, with thermal stress as important parameter, it is important to show temperature profiles throughout the cell. It is also important to show the heat flows occurring in the system, especially the amount of radiative heat transfer in comparison to the other heat transfer modes.

For validation the current and voltage output will be the most important outputs. Changing the current output will also change the voltage. When simulating over a large range of current outputs the dependence of output voltage on output current can be determined, which is known as the polarization curve. This gives important information about the fuel cell behavior at different external loads, and is relatively easy to determine experimentally. It is more difficult to validate temperature profiles, since temperature measurement in SOFCs are very rare. Since the system geometry can have great influence on thermal radiation, it is important that the modeling method is flexible in terms of modeling geometry.

There are various modeling approaches possible to model a SOFC. An important characterization is time dependence of a model. Only steady-state behavior is of interest here, which means all time dependent terms can be neglected.

In 0D-models only overall performance is of interest. This can be useful when transient behavior is studied, or when the component is part of a larger system. Parameters are lumped over large control volumes in the system, which means spatial distribution of variables is not determined. This approach has been chosen in various publications[33, 37–39]. This modeling paradigm is often chosen to study the transient behavior of a solid oxide fuel cell.

In 1D-models spatial distribution of variables is considered in one direction. This allows for more accurate calculation of variables in one direction, for example the axial direction of a tubular SOFC. This approach is also very popular in literature[21, 32, 34, 40–42].

This methodology can be extended to 2D-models[29, 43, 44], and 3D-models. This means the system will be subdivided in control volumes in two of three directions and variables are lumped over the control volumes.

The goal for the current models is however to obtain very detailed spatial distribution of internal variables, hence to use small control volumes. Physical phenomena are generally described with partial differential equations. These equations include mass, momentum, species and energy conservation equations in combination with constitutive equations. The problem is that most often there is no exact analytic solution available for the set of equations. Radiative heat transfer through a participating medium is described with a integro-differential equation for which there also does not exist a analytical solution.

A common approach for complex geometries is to divide space into a finite number of elements or volumes and to approximate the solution of partial differential equations by the numerical solution of algebraic equations relating the properties of the volumes. This is what happens in CFD modeling. The main disadvantage of this method is the large amount of computational effort it takes to solve a problem, but if well used, this method can provide valuable information. CFD modeling of SOFCs can be found in numerous articles, some obtain realistic results, but also unphysical results can be found [45]. This shows that it is still a challenge to obtain realistic results using this approach. This approach is used to develop the models in this thesis.

3.2. CFD MODELING OF SOFCS

The finite volume method uses the integral form of the conservation equations as its starting point. The solution domain is subdivided into a finite number of control volumes and the equations are applied to each control volume. The variables are calculated at each computational node, which is located at the centroid of each control volume. The variables are expressed at the boundaries in terms of the nodal values. This is done using interpolation schemes. Surface and volume integrals can be approximated using suitable quadrature formulas. This all results in a set of algebraic equations for each cell, containing a number of nodal values of neighbour cells, which have to be solved simultaneously.

First with the geometry of the problem must be approximated by a finite number of control volume. This mesh must be refined until the solution of the set of equations is independent of the amount of cells. This is called making the solution 'mesh independent'. This is followed by defining the model equations, material properties and boundary conditions. The model equations and boundary conditions will be discussed in the following section. The material properties are model dependent.

The models described in this thesis are developed using CFD-software Ansys Fluent. To account for electrochemistry and potential equations fuel cell add-on modules are used. There are two add-on modules available in Fluent that are capable of modeling SOFCs.

- Fuel Cell and Electrolysis Model
- SOFC Fuel Cell With Unresolved Electrolyte Model

Both add-on modules are used in this thesis. Figure 3.1 shows the important zones that must be included in the computational domain to obtain a solution. The figure on the left represents the 'Fuel Cell and Electrolysis

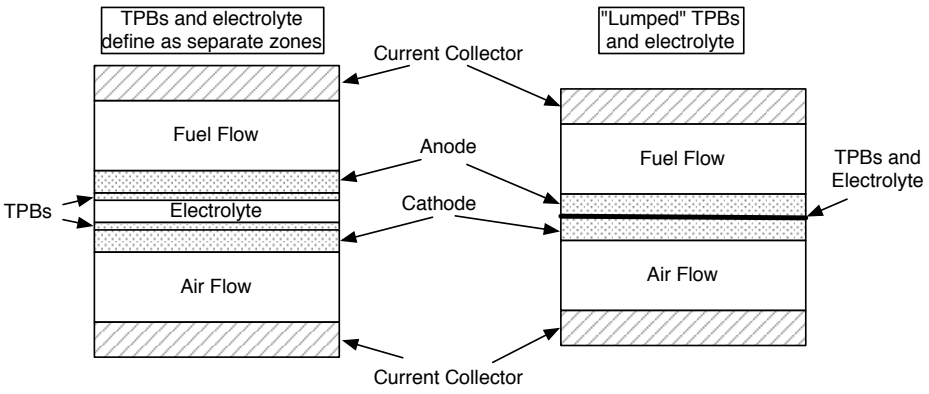

Figure 3.1: Cell zones necessary in fuel cell models

Model' and the figure on the right the 'SOFC Fuel Cell With Unresolved Electrolyte Model'. As can be seen in the figure the most important difference is that the reactions areas and electrolyte are defined as separate zones in the first model, and they are lumped onto an interface between anode and cathode in the second model. The following sections will discuss all the necessary modeling equations. The equations necessary for the fuel cell modules are obtained from ANSYS documentation [46].

3.3. ASSUMPTIONS

Before deriving all the model equations some assumptions applied on the different models will be listed here.

- Model operation is assumed to be steady state
- Laminar flow (low Reynolds number)
- Al flows can treated as incompressible ideal gases
- Material properties homogeneous
- Optical properties can be considered gray

3.4. MODEL EQUATIONS

The mass, momentum, energy, species and electric potential conservations equations will be derived in this section. Each zone in the computational domain needs additional constitutive equations to complete the set of equations.

3.4.1. POTENTIAL CONSERVATION EQUATION

The reactions at the anode and cathode TPB are given by equations (3.1) and (3.2).

$$H_2 + O^{2-} \leftrightarrow H_2O + 2e^- \tag{3.1}$$

$$\frac{1}{2}O_2 + 2e^- \leftrightarrow O^{2-} \tag{3.2}$$

Two potential fields will be present in the system, one driving the electron flow(ϕ_{solid}) and one driving the oxygen ion flow(ϕ_{ionic}). The reason for solving two potential equations is to obtain a 'overpotential' in the reaction areas (or TPBs). At zero current the reactions will be at equilibrium and both potential fields will give the same potential in the reaction areas. When a current is withdrawn from the system the reactions are driven away from equilibrium, which is modeled by a potential difference between the ionic field and the electron field. Both equations have identical form. The equation for conservation of electric potential is given by:

$$\vec{\nabla} \cdot (\sigma_{solid} \nabla \phi_{solid}) + R_{solid} = 0\,, \tag{3.3}$$

and the conservation of ionic transport is given by:

$$\vec{\nabla} \cdot (\sigma_{ionic} \nabla \phi_{ionic}) + R_{ionic} = 0\,. \tag{3.4}$$

ϕ_{solid} represents the potential field in the electrically conducting materials and ϕ_{ionic} the potential field in the electrolyte. To solve these potential field certain boundary conditions are necessary. For equation 3.3 boundary conditions are applied at the contact surfaces of the current collectors. At the contact surface of the anode side a potential of 0 [V] must be applied, at the contact surface of the cathode side either a potential ([V]) or a current density ([A/m^2]) must be applied. The boundary conditions for equation 3.4 are related to the potential field obtained by equation 3.3 by the overpotential in the reaction areas, which is shown later. Equation (3.3) is solved in the anode, cathode, the TPBs and the current collectors. Equation (3.4) is solved in the electrolyte and the TPBs.

The ionic conductivity, σ_{ionic}, can be modeled as a function of temperature using the following function (temperature in [K]):

$$\sigma_{ionic} = \frac{100}{0.3685 + 0.002838 e^{(10300/T)}} \tag{3.5}$$

This function is included in the fuel cell modules and is valid for temperatures between 1073 [K] and 1373 [K]. The terms R_{solid} and R_{ionic} represent the volumetric transfer current, and are non-zero only in the reaction zones. These terms are defined as:

$$\text{solid} \begin{cases} R_{solid} = -R_{an} (< 0) \text{ on anode side} \\ R_{solid} = +R_{cat} (> 0) \text{ on cathode side} \end{cases} \tag{3.6}$$

and:

$$\text{electrolyte} \begin{cases} R_{ionic} = +R_{an} (> 0) \text{ on anode side} \\ R_{ionic} = -R_{cat} (< 0) \text{ on cathode side} \end{cases} \tag{3.7}$$

These volumetric transfer currents are related to the overpotential by the Butler-Volmer equation. The Butler-Volmer equation for both the anode side and cathode side are shown in respectively equations (3.8) and (3.9).

$$R_{an} = \left(\zeta_{an} i_{0,ref}^{an}\right)\left(\frac{X_{H_2}}{X_{H_2,ref}}\right)^{\gamma_{H_2}} \left(e^{\alpha_{an} F \eta_{an}/RT} - e^{-\alpha_{cat} F \eta_{an}/RT}\right) \tag{3.8}$$

$$R_{cat} = \left(\zeta_{cat} i_{0,ref}^{cat}\right)\left(\frac{X_{O_2}}{X_{O_2,ref}}\right)^{\gamma_{O_2}} \left(-e^{\alpha_{an} F \eta_{cat}/RT} + e^{-\alpha_{cat} F \eta_{cat}/RT}\right) \tag{3.9}$$

The first term $\zeta_{an/cat}$ represents a specific active surface area of the triple phase boundary. This is the active reaction area divided by the volume of the reaction zone. The second term $i_{0,ref}$ represents the exchange current density. This is the current density in the reaction areas at equilibrium conditions, which means no net current output. This term is a measurement of the reaction rate of the electrochemical reactions and is often determined using a Arrhenius type equation. The ratio of X_i and $X_{i,ref}$ and the exponent γ_i are used to describe the concentration dependence of the current density. The last factor, containing the exponential, describes the dependence of the current density on the transfer coefficients ($\alpha_{\text{an/cat}}$), the overpotentials ($\eta_{\text{an/cat}}$), the Fahrenheid constant (F) and temperature. These exponential terms have an empirical background on which more information can be found in Appendix A. At equilibrium conditions these overpotentials will be zero, which means both the forward and backward reaction rates are equal.

There are two limiting cases of the Butler-Volmer equation, the low overpotential and high overpotential case. For the high overpotential region the Tafel equation can be used, which is given by:

$$R_{an} = \left(\zeta_{an} i_{0,ref}^{an}\right)\left(\frac{X_{H_2}}{X_{H_2,ref}}\right)^{\gamma_{H_2}} \left(e^{\alpha_{an} F \eta_{an}/RT}\right) \tag{3.10}$$

$$R_{cat} = \left(\zeta_{cat} i_{0,ref}^{cat}\right)\left(\frac{X_{O_2}}{X_{O_2,ref}}\right)^{\gamma_{O_2}} \left(e^{-\alpha_{cat} F \eta_{cat}/RT}\right) \tag{3.11}$$

This equation can be used instead of the Butler-Volmer equation in the add-on module. For the current system the Tafel-equations are only used to speed up convergence, the final solutions are determined with the Butler-Volmer equations.

The anodic and cathodic overpotential η_{an} and η_{cath} are determined using equation 3.12 and 3.13.

$$\eta_{an} = \phi_{solid,an} - \phi_{ionic,an}\,, \tag{3.12}$$

$$\eta_{cat} = \phi_{solid,cat} - \phi_{ionic,cat} - V_{OC}\,. \tag{3.13}$$

At the anode side the overpotential is the difference between ϕ_{solid} and ϕ_{ionic}. At the cathode side the term V_{OC} is subtracted, which is the open cell voltage. This represents the cell potential at zero current. The presence of the overpotentials η_{an} and η_{cath} in the source terms causes a strong nonlinear dependence of the source terms in (3.3)-(3.4) on the potentials ϕ_{solid} and ϕ_{ionic}. The Newton-Rhapson method is used to determine the overpotentials. Since the total electric current in both the anode and cathode reaction area must be the same, the following equation is used for current conservation.

$$\int_{anode} R_{an}\,dV = \int_{cathode} R_{cat}\,dV \tag{3.14}$$

Background information on these equations can be found in Appendix A.

SOFC FUEL CELL WITH UNRESOLVED ELECTROLYTE MODEL

In the Unresolved Electrolyte model the reactions zones and the electrolyte are lumped into an interface. In this module only one equation is necessary for the potential field, given by equation (3.15).

$$\vec{\nabla} \cdot (\sigma \nabla \phi) = 0 \tag{3.15}$$

The first boundary condition is a 0 [V] potential at the anode current collector. The second boundary condition is the potential on the 'lumped' interface, which is determined using the Nernst equation, given in equation (3.16).

$$\phi_{ideal} = \phi^0 + \frac{RT}{2F} ln\left(\frac{P_{H_2} P_{O_2}^{1/2}}{P_{H_2O}}\right) \tag{3.16}$$

The derivation of this equation is included in Appendix A. The Nernst equation represents the ideal potential. When there is no leakage current the Nernst potential is equal to the open cell voltage (OCV). The potential field must have a certain voltage jump applied at this 'lumped' interface to drive the electrochemical reactions. The actual cell voltage is determined by equation (3.17).

$$\phi_{cell} = \phi_{jump} - \eta_s \tag{3.17}$$

Where ϕ_{jump} is the voltage difference at the 'lumped' interface and η_s the ohmic loss in solid conducting regions. The jump condition is determined by:

$$\phi_{jump} = \phi_{ideal} - \eta_{ele} - \eta_{an} - \eta_{cat} \tag{3.18}$$

ϕ_{ideal} represents the Nernst voltage, η_{an} and η_{cat} the anodic and cathodic overpotential and η_{ele} the potential loss in the electrolyte. The current density is again determined by the Butler-Volmer equations:

$$i_{an} = i^{an}_{0,ref}\left(\frac{X_{H_2}}{X_{H_2,ref}}\right)^{\gamma_{H_2}}\left(\frac{X_{H_2O}}{X_{H_2O,ref}}\right)^{\gamma_{H_2O}}\left(e^{\alpha_{an}F\eta_{an}/RT} - e^{-\alpha_{cat}F\eta_{an}/RT}\right) \tag{3.19}$$

$$i_{cat} = i^{cat}_{0,ref}\left(\frac{X_{O_2}}{X_{O_2,ref}}\right)^{\gamma_{O_2}}\left(-e^{\alpha_{an}F\eta_{cat}/RT} + e^{-\alpha_{cat}F\eta_{cat}/RT}\right) \tag{3.20}$$

This equations used in this module are slightly different than equations (3.8) and (3.9). The anodic current density also has a H_2O dependence in this module.

3.4.2. MASS CONSERVATION EQUATION

The steady-state mass conservation equation is given by

$$\vec{\nabla}\cdot\left(\rho\vec{v}\right) = S_m\,. \tag{3.21}$$

In the fluid zones the source term S_m is equal to zero. This term is only non-zero in the reaction areas of the domain. Because oxygen ions cross over from the cathode side to the anode side, this term serves as a sink at the cathode side and a source at the anode side.

SOFC FUEL CELL WITH UNRESOLVED ELECTROLYTE MODEL

In this module this source term acts as source/sink at the cathode/anode side of the electrolyte interface. At the cathode side of the 'lumped' interface oxygen is consumed, so the source term will act as a sink here. At the anode side water vapor is produced, which means the source term will act as a mass source.

3.4.3. MOMENTUM CONSERVATION EQUATION

The flows are all assumed to be low Reynolds number laminar flows. Assuming that gravitational forces are negligible and the system is steady-state, the momentum conservation equation is given by:

$$\vec{\nabla}\cdot\left(\rho\vec{v}\,\vec{v}\right) = -\vec{\nabla}P + \vec{\nabla}\cdot(\overline{\tau}) + \vec{S}\,. \tag{3.22}$$

Where $\overline{\tau}$ is the viscous stress tensor which is given by:

$$\overline{\tau} = \mu\left[\left(\vec{\nabla}\vec{v} + \vec{\nabla}\vec{v}^{\,T}\right) - \frac{2}{3}\vec{\nabla}\cdot\vec{v}\,I\right]\,. \tag{3.23}$$

The fluid is incompressible which means $\nabla\cdot\vec{v} = 0$. This implies that both the second and third term of this equation are equal to zero. This means the momentum equation simplifies to:

$$\vec{\nabla}\cdot\left(\rho\vec{v}\,\vec{v}\right) = -\vec{\nabla}P + \mu\vec{\nabla}^2\vec{v} + \vec{S}\,. \tag{3.24}$$

In the flow channels the source term S_i is zero. This term is used in the porous areas to account for extra pressure drop. The pressure drop in porous areas can be determined using equation (3.25).

$$S_i = -\left(\sum_{j=1}^{3} D_{ij}\mu v_j + \sum_{j=1}^{3} C_{ij}\frac{1}{2}\rho|v|v_j\right)\,. \tag{3.25}$$

The source term S_i are the components of $\overrightarrow{S}$ in the three coordinate directions. D and C are prescribed matrices and $|v|$ is absolute velocity. The first term accounts for viscous resistance and the second term inertial resistance. For homogeneous porous media this equation can be written as:

$$S_i = -\left(\frac{\mu}{\alpha} v_i + C_2 \frac{1}{2} \rho |v| v_i\right) \tag{3.26}$$

The matrices D and C are specified here as diagonal matrices with $1/\alpha$ and C_2 on the diagonals. Under the assumption that inertial pressure losses are negligible in comparison with viscous losses, the pressure drop reduces to Darcy's law, given by:

$$\overrightarrow{\nabla} P = -\frac{\mu}{\alpha} \overrightarrow{v} \, . \tag{3.27}$$

Where α is the permeability and μ the dynamic viscosity.

3.4.4. ENERGY CONSERVATION EQUATION

The steady-state energy conservation equation is solved in Ansys Fluent in the following form:

$$\overrightarrow{\nabla} \cdot \left(\overrightarrow{v} \left(\rho E + P\right)\right) = \overrightarrow{\nabla} \cdot \left(k_{eff} \overrightarrow{\nabla} T - \sum_i h_i \overrightarrow{J}_i + \left(\overline{\tau}_{eff} \cdot \overrightarrow{v}\right)\right) + S_h \, . \tag{3.28}$$

Where $E = h - \frac{P}{\rho} + \frac{v^2}{2}$. E is the specific total energy, h is the specific enthalpy. The change of specific kinetic energy can be considered negligible compared to the internal energy ($h - P/\rho$). The first term on the right hand side represents heat conduction, the second term enthalpy transport due to species diffusion and the third term viscous heating. Transport of enthalpy due to species diffusion can have a significant effect and should not be neglected when the Lewis number, shown in equation (3.29), is far from unity for any species.

$$Le_i = \frac{k}{\rho c_p D_{i,m}} \tag{3.29}$$

For the current models can be shown that this term cannot be neglected. Viscous heating can be neglected when the Brinkman number, shown in equation (3.30), is much smaller than unity.

$$Br = \frac{\mu U_e^2}{k \Delta T} \tag{3.30}$$

For the current system considered in this work it can be shown that this term can be neglected. This means the energy equation can be simplified to equation (3.31).

$$\overrightarrow{\nabla} \cdot \left(\overrightarrow{v} \rho h\right) = \overrightarrow{\nabla} \cdot \left(k_{eff} \overrightarrow{\nabla} T - \sum_i h_i \overrightarrow{J}_i\right) + S_h \, . \tag{3.31}$$

In this equation k_{eff} is an effective thermal conductivity. In the fluid zones k_{eff} is equal to the normal fluid thermal conductivity. In porous areas the effective conductivity is determined as the volumetric average between fluid and solid conductivity:

$$k_{eff} = \epsilon k_f + (1 - \epsilon) k_s \, . \tag{3.32}$$

Where ϵ is the porosity of the medium. The species flux $\overrightarrow{J}_i$ will be discussed in detail at the species conservation equations in section 3.4.5. The last term in the energy equation, S_h, is a source term. This term is used to include all SOFC heat sources and to include radiative heat transfer in the energy equation. The heat source included by the fuel cell module is given by equation (3.33).

$$S_h = h_{react} - R_{an,cat} \eta_{an,cat} + i^2 R_{ohm} \tag{3.33}$$

Where h_{react} is the specific enthalpy rate of change by reaction, $R_{an,cat}$ is the volumetric transfer current in anode or cathode, $\eta_{an,cat}$ is the overpotential in anode or cathode, i is the current given by (3.3) and (3.4) and R_{ohm} is the ohmic resistance of conducting media. This equation suggests that electrical work is not included in the energy equation[1].

[1] A service request was submitted at the Ansys Customer Portal to ask why electrical work is not included in the energy equation. Apparently only the heat of reaction TdS is included in the term h_{react} in the energy equation, which means electrical work is indirectly accounted for.

FUEL CELL WITH UNRESOLVED ELECTROLYTE

In all solid regions the heat generated due to ohmic losses is given in equation (3.34).

$$S_h = i^2 R_{ohm} \tag{3.34}$$

The heat due to the electrochemical reactions and activation overpotential is included using the following term:

$$S_h = \frac{h_{H_2} + h_{O_2} - h_{H_2O}}{V_{cells}} - i\Delta V \tag{3.35}$$

Where the enthalpy terms h_i are the total enthalpy of species i (J/s) and i is the current density. V_{cells} is the volume of the cells adjacent to the interface. The first three terms account for the enthalpy change of reaction, the last term is the useful work delivered by the fuel cell. The difference between these both is the heat released due to reversible and irreversible heat sources. This heat is released at the interface between anode and cathode. 50% of the energy is released in the cells adjacent to the anode side and 50% at the cathode side. This is an arbitrary assumption.

THE RADIATIVE TRANSFER EQUATION

Another source term is the radiative transfer equation which describes the energy balance of a beam of thermal radiation in a participating medium, shown in Eq. (3.36). This equation gives a balance along a thin pencil of rays, for a medium that emits, absorbs and/or scatters radiation.

$$\frac{dI_\lambda}{ds} = \vec{\nabla} \cdot (I(\vec{r}, \vec{s})\vec{s}) = \kappa_\lambda n^2 I_{b\lambda} - (\kappa_\lambda + \sigma_s) I_\lambda(\vec{r}, \vec{s}) + \frac{\sigma_s}{4\pi} \int_0^{4\pi} I_\lambda(\vec{r}, \vec{s}\,')\Phi(\vec{s} \cdot \vec{s}\,')d\Omega' \tag{3.36}$$

Here $I_{b\lambda}$ is the black body intensity given by Planck's law ($I_{b\lambda} = E_{b\lambda}/\pi$), κ_λ is the spectral absorption coefficient and λ indicates that everything is per unit of wavelength. The scattering coefficient σ_s, scattering phase function Φ and refractive index n are assumed independent of wavelength in Fluent. When the medium through which the beam travels can be considered gray, which means all properties are independent of wavelength, the subscript λ can be omitted.

Fluent supports a way to model non-grey behavior of materials. The spectrum is divided into N wavelength bands, each with constant properties. This model is also referred to as the 'Box Model' in literature [8]. In general it is an inaccurate representation of non-grey behavior. It is also the most simple method, which means easy implementable in software packages as Fluent.

Solving the radiative transfer equation gives an energy balance for an infinitesimal pencil of rays. A volume balance is obtained by integrating this balance over all solid angles to obtain the heat flux per unit wavelength:

$$\vec{q}_\lambda = \int I_\lambda \vec{s}\, d\Omega \tag{3.37}$$

And integration over all solid angles is necessary to obtain the total heat flux:

$$\vec{q} = \int_0^\infty \vec{q}_\lambda d\lambda \tag{3.38}$$

The source term due to radiative heat transfer appearing in the energy equation is the divergence of the heat flux:

$$S_h = \vec{\nabla} \cdot \vec{q} \tag{3.39}$$

In absence of scattering and assuming uniform absorption coefficient and temperature the solution of the RTE is of the form:

$$I_\lambda(r, \vec{s}) = I_\lambda(0, \vec{s}) \exp(\kappa_\lambda s) + I_{b\lambda}\left[1 - \exp(-\kappa_\lambda s)\right] \tag{3.40}$$

The radiative heat transfer in the medium is characterized by the emissivity ϵ_λ:

$$\epsilon_\lambda = \left[1 - \exp(-\kappa_\lambda s)\right] \tag{3.41}$$

The emissivity ϵ_λ is wavelength and path length dependent. An effective emissivity describing the evolution of the total intensity $I = \int I_\lambda d\lambda$ is given by:

$$I(r, \vec{s}) = I(0, \vec{s})(1 - \epsilon) + I_b \epsilon \tag{3.42}$$

Finding good approximations for the emissivity, ϵ, is a big problem in radiative heat transfer.

3.4.5. SPECIES CONSERVATION EQUATION

The model takes into account 4 species, which means 3 transport equations must be solved. The species conservation equation predicts the mass concentration Y_i using the convection-diffusion equation shown in (3.43).

$$\nabla \cdot (\rho \overrightarrow{v Y_i}) = -\nabla \cdot \overrightarrow{J}_i + S_i \,. \tag{3.43}$$

The term on the left hand side of the equation represent convection of species i. The term $\overrightarrow{J}_i$ represents a flux due to species diffusion and S_i is a source term which accounts for chemical reactions.

Diffusion of species A with respect to B occurs because of driving forces that include concentration gradients (ordinary diffusion), pressure and temperature (thermal diffusion). Pressure diffusion requires a large gradient, which is achieved for example with gas mixtures in a centrifuge [47]. This can be in the current system. Fick's law of diffusion is the most well known method to relate the flux of species i to its concentration gradient. The way Fick's law as implemented in Fluent is shown in equation (3.44).

$$\overrightarrow{J}_i = -\rho D_{i,m} \nabla Y_i - D_{i,T} \frac{\nabla T}{T} \tag{3.44}$$

The first term on the right hand side represents the flux caused by concentration gradients, $D_{i,m}$ is the diffusion coefficient of species i in mixture m. The second term on the right hand side represents thermal diffusion, with $D_{i,T}$ the thermal (Soret) diffusion coefficient. This method is also called the dilute approximation approach, because it only holds for a dilute component in a carrier gas.

When using the dilute approximation approach the method to determine the mass diffusivities of the species is shown in equation (3.45).

$$D_i = \epsilon^{1.5} (1-s)^{r_s} \left(\frac{p_0}{p}\right)^{\gamma_p} \left(\frac{T}{T_0}\right)^{\gamma_t} \tag{3.45}$$

Where D_i^0 is the mass diffusivity of species i at T_0 and p_0. The exponents and reference values are defined in the user defined functions (UDFs) as:

$$\begin{aligned} p_0 &= 101325 \quad [\mathrm{N/m^2}] \\ T_0 &= 300 \quad [K] \\ \gamma_p &= 1.0 \\ \gamma_t &= 1.5 \\ r_s &= 2.5 \end{aligned}$$

A more accurate method for multi-component mixtures is to use the Stefan-Maxwell equations, also called the full multicomponent diffusion method. In Fluent the Stefan-Maxwell equations are used to determine coefficients for the 'generalized Fick's law', which is shown in equation (3.46). The derivation of this method can be found in Merk [48].

$$\overrightarrow{J}_i = -\sum_{j=1}^{n-1} \rho D_{ij} \nabla Y_j - D_{i,T} \frac{\nabla T}{T} \tag{3.46}$$

Where D_{ij} is a $(n-1) \times (n-1)$ matrix with generalized Fick's law diffusion coefficients, which is determined with:

$$D_{ij} = [D] = [A^{-1}][B] \tag{3.47}$$

The components in matrix $[A]$ and $[B]$ are determined with:

$$A_{ii} = -\left(\frac{X_i}{D_{in}} \frac{M_w}{M_{w,n}} + \sum_{\substack{j=1 \\ j \neq i}}^{N} \frac{X_j}{D_{ij}} \frac{M_w}{M_{w,i}} \right) \tag{3.48}$$

$$A_{ij} = X_i \left(\frac{1}{D_{ij}} \frac{M_w}{M_{w,j}} - \frac{1}{D_{in}} \frac{M_w}{M_{w,n}} \right) \tag{3.49}$$

$$B_{ii} = -\left(X_i \frac{M_w}{M_{w,n}} + (1 - X_i) \frac{M_w}{M_{w,i}} \right) \tag{3.50}$$

$$B_{ij} = X_i \left(\frac{M_w}{M_{w,j}} - \frac{M_w}{M_{w,n}} \right) \tag{3.51}$$

To calculate this matrix of generalized Fick's law diffusion coefficients the binary diffusion coefficients must be known. These can be determined using a modified Chapman-Enskog formula, shown in (3.52). This is a theoretical method based on Boltzmann's theory of gases, the theorem of corresponding states and a suitable intermolecular energy-potential function [47].

$$D_{ij} = 0.00188 \frac{\left[T^3 \left(\frac{1}{M_{w,i}} + \frac{1}{M_{w,j}}\right)\right]^{\frac{1}{2}}}{p_{abs} \sigma_{ij}^2 \Omega_D} \tag{3.52}$$

The term σ_{ij} is determined using the Lennard-Jones characteric length of species i and j, also referred to as average collision diameter, and Ω_D is the diffusion collision integral that is determined using the Lennard-Jones energy parameter ϵ_{LN}. The term Ω_D is a function of T_D^* which is given by equation (3.53).

$$T_D^* = \frac{T}{(\epsilon_{LJ}/k_B)_{ij}} \tag{3.53}$$

And $(\epsilon_{LJ}/k_B)_{ij}$ is determined using:

$$\left(\frac{\epsilon_{LJ}}{k_B}\right)_{ij} = \sqrt{(\epsilon_{LJ}/k_B)_i (\epsilon_{LJ}/k_B)_j} \tag{3.54}$$

Where σ_i is the Lennard-Jones characteristic length of species i. And σ_{ij} is determined with:

$$\sigma_{ij} = 1/2(\sigma_i + \sigma_j) \tag{3.55}$$

Where σ_i is the Lennard-Jones energy parameter of species i. Another method of greater accuracy is the Fuller method, which retains the form of the Chapman-Enskog theory but uses emperical constants derived from experimental data [5].

For the current models the full multicomponent method is used in combination with the Chapman-Enskog binary diffusion coefficients. Although the Fuller method is more accurate it is chosen to use Chapman-Enskog because this method is already implemented in Fluent. Also both methods are used in numerous fuel cell models [5], and the focus of this study is not mass transfer in SOFCs.

The calculated diffusion coefficients are properties of the gas mixture. Corrected diffusion coefficients are used to take into account the fact that the diffusion through channels of a porous medium is slower than in open space. One way to do this is to use the Bruggeman correction which is shown in equation (3.56). This is a well known correction method, the factor 1.5 is an empirical constant [49].

$$D_{ij}^{eff} = \epsilon^{1.5} D_{ij} \tag{3.56}$$

The Bruggeman correction is the default correction in the Fuel Cell module, but can be overwritten with other methods. Chosen is to use this default method.

The source term in the species conservation equation contains all the sink/sources due to electrochemical reactions, and these are a function of the volumetric transfer current. The transfer currents have units of [A/m^3]. Current is by definition transport of charge per unit of time, or [C/s]. The charge of a mole electrons is given by the Faraday constant F. From the anode and cathode half-reactions shown in equations (3.1) and (3.2) is known that for each reacting hydrogen atom two electrons are produced. At the cathode 4 oxygen atoms are necessary for the reduction reaction with 2 electrons. This means the different source terms are given by:

$$S_{H_2} = -\frac{M_{W,H_2}}{2F} R_{an} \tag{3.57}$$

$$S_{O_2} = -\frac{M_{W,O_2}}{4F} R_{cath} \tag{3.58}$$

$$S_{H_2O} = \frac{M_{W,H_2O}}{2F} R_{an} \tag{3.59}$$

SOFC FUEL CELL WITH UNRESOLVED ELECTROLYTE MODEL
This module used the full multicomponent method described above, based on the generalized Fick's law. The binary diffusion coefficient are used with the same Chapman-Enskog method. Instead of the Bruggeman method another correction method is used for the porous media, given in equation (3.60), with τ the tortuosity of the pores.

$$D_{ij}^{eff} = \frac{\epsilon}{\tau} D_{ij} \tag{3.60}$$

This is also a well known method to determine a effective diffusion coefficient in a porous matrix [49]. For low tortuosity and low porosity equations (3.56) and (3.60) give very similar results. In the unresolved electrolyte model the same equations are solved, but instead of the volumetric transfer current in (3.57), (3.58) and (3.59) the current density i_{an} and i_{cat} are used.

3.5. MATERIAL PROPERTIES

This section will give an overview of all material properties that must be specified to solve the given set of equations. The properties needed are of course model dependent, but the approximations used are presented here. For each individual species the following properties must be determined:

- Specific heat capacity
- Density
- Thermal conductivity
- Dynamic viscosity
- Molecular weight
- L-J Characteristic Length
- L-J Energy parameter
- Ohmic resistance
- Ionic resistance

The specific heat of each species is implemented using a piece-wise polynomial with temperature as variable. The other species properties are defined as independent of temperature. These properties are however made dependent on composition. The L-J (Lennard-Jones) parameters are necessary to determined the diffusion coefficients of the species, these values can be obtained from literature [50].

3.5.1. PROPERTIES SOLID MATERIALS

The material properties of the anode, cathode, electrolyte and current collectors are all model specific and are obtained from literature. In the description of each model will be discussed where these properties are exactly obtained from. This included all the properties necessary to solve the radiative transfer equation.

3.5.2. PROPERTIES GAS COMPONENTS

Solid oxide fuel cells operate at high temperature and moderate pressure. This means the thermodynamic state of the gases can be described using the ideal gas law, shown in equation (3.61).

$$PV = nRT \tag{3.61}$$

There are four species included in the fuel cell models: H_2, O_2, N_2, H_2O. Using the ideal gas law together with the mixture composition allows the determination of the mixture density using equation (3.62).

$$\rho = \frac{P_{op}}{RT \sum_i \frac{Y_i}{M_{w,i}}} \tag{3.62}$$

The specific heat of each component is determined using a temperature dependent polynomial, as shown in equation (3.63).

$$C_{p,i} = a_0 + a_1 T + a_2 T^2 + a_3 T^3 + a_4 T^4 + a_5 T^5 \quad \text{[J/kgK]} \tag{3.63}$$

The coefficients necessary to determine the specific heat are shown in table 3.1. These coefficients are based on data from literature [51]. The heat capacity of the mixture is determined using a mass weighted average as

Table 3.1: Specific heat coefficients for equation (3.63). Valid in range 273 - 1473 [K].

	a_0	a_1	a_2	a_3	a_4	a_5
H_2	1.1211E+04	2.2176E+01	-5.4364E-02	6.2299E-05	-3.2716E-08	6.5000E-12
O_2	9.9886E+02	-9.7824E-01	3.3815E-03	-4.0581E-06	2.1962E-09	-4.5076E-13
N_2	1.1089E+03	-4.9226E-01	1.0298E-03	-5.0954E-07	-1.7020E-11	4.7882E-14
H_2O	1.9242E+03	-8.8375E-01	3.0808E-03	-3.0750E-06	1.5785E-09	-3.3325E-13

shown in equation (3.64).

$$C_{p,mixture} = \sum_i Y_i C_{p,i} \tag{3.64}$$

The thermal conductivity of each component is also temperature dependent using a similar polynomial:

$$k_{,i} = b_0 + b_1 T + b_2 T^2 + b_3 T^3 + b_4 T^4 + b_5 T^5 \quad [\mathrm{W/mK}] \tag{3.65}$$

The necessary coefficients are shown in table 3.2. The dynamic viscosity of each component is also deter-

Table 3.2: Thermal conductivity coefficients for equation (3.65). Valid in range 273 - 1473 [K].

	b_0	b_1	b_2	b_3	b_4	b_5
H_2	1.8743E-02	5.9471E-04	-3.4943E-07	2.5890E-10	-1.1230E-13	2.0439E-17
O_2	-1.4120E-03	1.0707E-04	-5.9015E-08	4.0842E-11	-1.6908E-14	2.9778E-18
N_2	1.2264E-03	1.0705E-04	-1.0779E-07	1.2594E-10	-7.2863E-14	1.5813E-17
H_2O	1.1990E-02	-4.1741E-06	9.0874E-08	6.5360E-11	-9.3835E-14	2.7799E-17

mined using a temperature dependent polynomial:

$$\mu_{,i} = c_0 + c_1 T + c_2 T^2 + c_3 T^3 + c_4 T^4 + c_5 T^5 \quad [\mathrm{Pa \cdot s}] \tag{3.66}$$

The relevant coefficients are shown in table 3.3. Thermal conductivity and viscosity of the mixture are deter-

Table 3.3: Dynamic viscosity coefficients for equation (3.66). Valid in range 273 - 1473 [K].

	c_0	c_1	c_2	c_3	c_4	c_5
H_2	1.7504E-06	2.8175E-08	-1.7980E-11	1.3414E-14	-5.8369E-18	1.0643E-21
O_2	5.0973E-07	8.2702E-08	-6.6823E-11	5.0493E-14	-2.1864E-17	3.9599E-21
N_2	7.6070E-07	7.1291E-08	-5.9966E-11	4.5823E-14	-1.9960E-17	3.6282E-21
H_2O	-1.0581E-06	2.8029E-08	2.9292E-11	-2.9630E-14	1.3407E-17	-2.4342E-21

mined by a ideal-gas mixing law.

$$\mu_{mixture} = \sum_i \frac{X_i \mu_i}{\sum_j X_i \phi_{ij}} \tag{3.67}$$

With:

$$\phi_{ij} = \frac{\left[1 + \left(\frac{\mu_i}{\mu_j}\right)^{1/2} \left(\frac{M_{w,i}}{M_{w,j}}\right)^{1/4}\right]^2}{\left[8\left(1 + \frac{M_{w,i}}{M_{w,j}}\right)\right]^{1/2}} \tag{3.68}$$

RADIATIVE PROPERTIES

When considering the gas flows as participating in the radiative transfer problem some properties must be determined. One way of doing this is assuming the entire medium as a gray gas. A more accurate approach is to make these properties composition dependent, what is done in the Weighted Sum Of Gray Gases model (WSGGM). This leads to an expression of the emissivity of the gas of the form:

$$\epsilon = \sum_{i=1}^{I} a_{\epsilon,i}(T)\left(1 - e^{-\kappa_i P s}\right) \tag{3.69}$$

Where $a_{\epsilon,i}$ is a emissivity weighting factor, k_i the absorption coefficient of species i (expressed in units [$m^{-1}bar^{-1}$], P the sum of partial pressures of absorbing gases and s is the path length. The absorption coefficient for $i = 0$ is assigned a value of zero:

$$a_{\epsilon,0} = 1 - \sum_{j=1}^{I} a_{\epsilon,i} \tag{3.70}$$

The emissivity weighting factors can be made temperature dependent, using a polynomial such as shown in equation (3.71).

$$a_{\epsilon,i} = \sum_{j=1}^{I} b_{\epsilon,i,j} T^{j-1} \tag{3.71}$$

Where $b_{\epsilon,i,j}$ are polynomial coefficients for the gas emissivity, which are empirical parameters and specific for a range of gas compositions. The absorption coefficients κ_i and the weighting factors $a_{\epsilon,i}$ can be found in literature [52–54]. When the total emissivity ϵ of the gas mixture is known an effective absorption coefficient can be determined:

$$\kappa_{gas} = -\frac{\ln(1-\epsilon)}{s} \tag{3.72}$$

This property is used to solve for the RTE in the fluid domains.

3.6. BOUNDARY CONDITIONS

Since each model discussed in the chapters hereafter uses different equations the required boundary conditions are slightly different. They will be discussed in the description of each individual model. These boundary conditions include the following:

- Inlet mass flow, composition, temperature
- Outlet pressure, temperature
- Walls adiabatic or prescribed temperature
- External contact current density or potential prescribed
- Radiative surface properties
- Background radiation temperature

3.7. SOLVER

To solve the partial differential equations shown in the previous sections numerical approximation methods are necessary. The first step is to capture the geometry of the model using a finite amount of control volumes. High gradients require more control volumes to approximate all physical phenomena more accurate. There must be enough control volumes in the domain to obtain an accurate solution. The computational mesh must be refined until the amount of control volumes does not influence the solution anymore, in other words, to make the solution 'grid-independent'. The computational mesh will be discussed in the description of each developed model.

For all conservation equations second order upwind schemes are used. This is a well known method which can be found in CFD-textbooks [55]. Gradients at the cell boundaries are determined using the Least Squares Method. A pressure-based solver is used to solve for the flow equations. These can be done in a segregated way or a coupled way. All models in this thesis use the coupled solver. This means that the momentum and pressure-based continuity equation are solved together. This results in more robust convergence and it said to be more stable when all model equations are strongly dependent on each other, which is the case for the current models.

3.7.1. NUMERICAL SOLUTION METHOD FOR THE RADIATIVE TRANSFER EQUATION

For most cases no exact analytic solutions exist for the radiative transfer equation. This has lead to the development of several approximate models and associated numerical solution methods over the years. The solution methods available in Fluent are:

- Rosseland
- Discrete Transfer (DTRM)

- P1
- Surface to Surface (S2S)
- Discrete Ordinates (DO)

The Rosseland approximation can be used when the participating medium has an optical thickness much larger than unity. From the literature study it is known that this is the case for the anode and cathode materials. In the limit of approaching a wall everything becomes optical thin, so near wall surfaces this model may give erratic results.

The DTRM method is a method by which the accuracy can be increased by increasing the number of rays involved, and this method applies to a wide range of optical thickness. There are however some limitations to this model. Only diffuse reflection can be modeled at walls. Scattering is not included in this model. This method only allows gray media.

The P1 method solves the RTE as a diffusion equation. This model includes the effect of scattering and non-gray radiation. Only diffuse reflection is considered at walls.

The S2S (Surface To Surface) method can be used when there are no participating media. This method calculates radiation within enclosed surfaces and considers only gray radiation and diffuse surfaces. The DTRM and DO-method are also able to calculate surface-to-surface radiation, but this method has a shorter computation time. Before running the simulation it is necessary to calculate all the view factors.

The DO-method is the most general solution method to approximate the RTE. This method spans the entire range of optical thicknesses and allows to solve problems for both surface-to-surface radiation and radiation in participating media. This method also allows non-gray properties and specular surfaces. Scattering is modeled using a scattering coefficient and a scattering phase function, which can be defined anisotropic using this method.

Because the models in this thesis will span a wide range of optical properties and must be able to take participating media into account it is chosen to use the DO-method. What the DO-method does is divide the integral in Eq. (3.36) into discrete solid angles. The direction integral in Eq. (3.36) is approximated by numerical quadrature, as shown Eq. (3.73).

$$\int_{4\pi} f(\vec{s})\, d\Omega \approx \sum_{i=1}^{n} w_i f(\vec{s_i}) \tag{3.73}$$

Were w_i are quadrature weights associated with each direction $\vec{s_i}$. The radiative transfer equation (Eq. (3.36)) can now be approximated with a set of n equations.

$$\vec{s_i} \cdot \vec{\nabla} I(\vec{r}, \vec{s_i}) = \kappa(\vec{r}) I_b(\vec{r}) - \beta(\vec{r}) I(\vec{r}, \vec{s}) + \frac{\sigma_s(\vec{r})}{4\pi} \sum_{j=1}^{n} w_j I(\vec{r}, \vec{s_j}) \Phi(\vec{r}, \vec{s_j}, \vec{s_i}), \quad i = 1, 2, ..., n \tag{3.74}$$

Subject to boundary conditions:

$$I(\vec{r_w}, \vec{s_i}) = \epsilon(\vec{r_w}) I_b(\vec{r_w}) + \frac{\rho(\vec{r_w})}{\pi} \sum_{\vec{n} \cdot \vec{s_j} < 0} w_j I(\vec{r_w}, \vec{s_j}) |\vec{n} \cdot \vec{s_j}| \quad \vec{n} \cdot \vec{s_i} > 0 \tag{3.75}$$

Solving this equation gives the radiative intensity at every location. The solution depends on material properties and temperature of the medium and on the properties of the bounding surfaces. One of the properties that can be shown after postprocessing in Fluent is incident radiation. This property is obtained by integration of the radiative intensity over all solid angles. The definition is shown in equation (3.76).

$$G = \int_{4\pi} I(\vec{r}, \vec{s})\, d\Omega \tag{3.76}$$

To solve the energy conservation equation, the radiative intensity must be used to determine the volumetric heat source due to radiation. The radiative heat flux is determined with Eq. (3.77).

$$q_{rad}(\vec{r}) = \int_{4\pi} I(\vec{r}, \vec{s})\, \vec{s}\, d\Omega \approx \sum_{i=1}^{n} w_i I_i(\vec{r})\, \vec{s_i} \tag{3.77}$$

To know how much energy is deposited (or withdrawn from) each volume element, the divergence of the radiative heat flux must be determined.

The way Fluent uses this method can be explained using Fig. 3.2. This figure shows an angular coordinate system, polar angle θ and azimuth angle ϕ. Each octant of angular space 4π is divided into $N_\theta \times N_\phi$ control angles. It can happen that a control angle crosses the boundary of two materials. Therefore a number of pixels per control angle have to be specified. These pixels allow for interpolation across the control angle, which means one pixel could be a heat inflow and an other pixel a heat outflow. The Fluent manual recommends at least a 3×3 pixelation for problems involving symmetry, periodic, specular of semi-transparent boundaries.

For a 2D geometry the z-direction is considered infinitely long in both positive and negative direction. The xy-plane which contains the 2D geometry is considered as a symmetry plane in z-direction. This means the DO equation only has to be solved in 4 octants, which means there is a total of $4N_\theta N_\phi$ control angles.

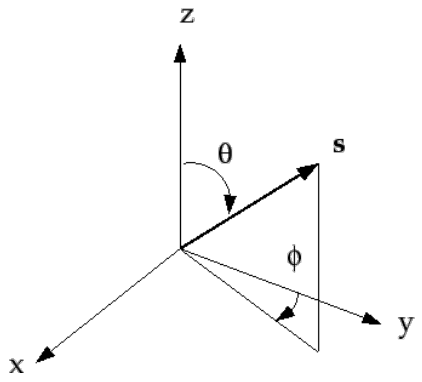

Figure 3.2: Angular Coordinate System used for DO-method[56]

4

RADIATIVE HEAT TRANSFER IN THE PEN-STRUCTURE

4.1. INTRODUCTION

In the literature study three articles were discussed that study thermal radiation in the PEN-structure. In this chapter radiation in PEN-structure will be studied in more detail, since the results from the literature study were not in agreement. All three articles agree that the anode and cathode can be considered optical thick. In two of the articles these materials were therefore considered opaque, non-participating, but in Murthy and Fedorov [15] these layers were modeled as participating media. This lead to very different results. In the models developed here the absorption coefficients of the anode and cathode will be varied over a large range to study its effect on the temperatures and heat flows. The articles agree that thermal radiation in the electrolyte has a negligible effect on the temperature field. This is also checked by varying the optical properties of the electrolyte. This results will help to explain the differences between the discussed articles, and will show whether the materials in the PEN-structure should be modeled as participating media.

4.2. MODEL DESCRIPTION

The models will be based on Daun et al. [16] and Murthy and Fedorov [15]. A schematic of the model from Daun et al. [16] is shown in figure 4.1a. This shows a 2D representation of the PEN-structure, with flow channels included at the top and bottom. This model is simplified here by omitting the flow channels, which means only the solid material will be left. This model will be referred to as 'Case One'. For the model based on Murthy and Fedorov [15] the geometry is similar, but with different dimensions. This model will be referred to as 'Case Two'. The assumptions applied to the these models are listed below:

- System isothermal in x-direction
- Convection and radiation at flow boundaries
- Material properties are homogeneous
- Materials are modeled as gray media
- Uniform heat source in reaction areas to account for electrochemical reactions

The isothermal assumption holds if only a small slice of the PEN-structure is taken into account, where gradients in the x-direction are very small. This is forced upon the models by applying symmetry boundary conditions on the left and right wall. At the flow boundaries heat flux boundary conditions are applied. This is specified in Fluent using a convective heat transfer coefficient and radiative properties of the surfaces. The materials are approximated as gray effective media. As a first approximation this should give some basic insight in the physics involved. Since in Daun et al. [16] uniform heat sources are applied in the PEN-structure this is also done in the current models. In Murthy and Fedorov [15] a coupled electrochemical model determines the current density, voltage and heat flux at the electrodes based on the species and temperature distribution within the cell. The information necessary to reproduce this is not given in the article. This is why both in case one and case two the same heat sources are applied.

The geometry used for case one is shown in figure 4.1 and the geometry for case two is shown in figure 4.2. The schematic show that the main difference between both models is the thickness of the electrodes and electrolyte. The reaction area in case two is assumed to have a thickness of 50 [μm].

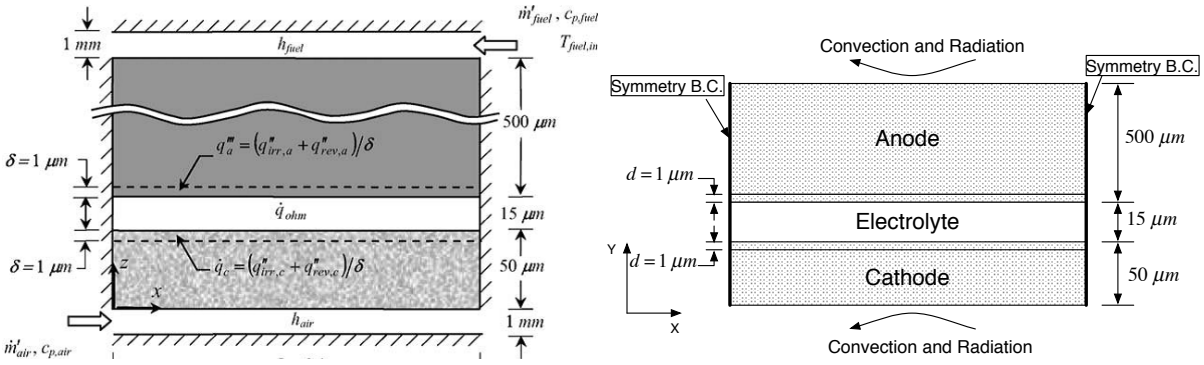

Figure 4.1: (a) Geometry from Daun et al. [16]. (b) Case One, based on the model from Daun et al. [16]

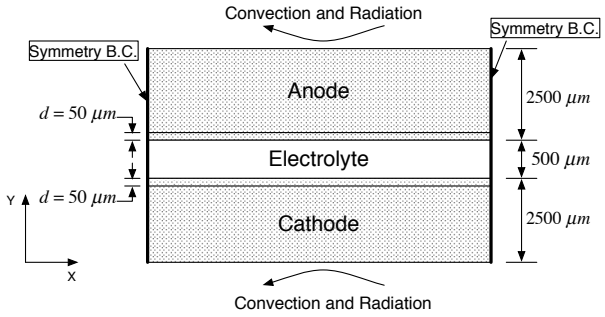

Figure 4.2: Case Two, based on the model from Murthy and Fedorov [15]

4.2.1. PROPERTIES

In the preliminary models there is no flow and there are no species. The equations necessary for the electrochemistry are not included in this model, instead uniform heat sources are applied to the appropriate areas. These heat sources are obtained from Daun et al. [16] and are based on a uniform current density of 4000 [A/m^2]. The only equations solved in the solution domain are the energy conservation equation and the radiative transfer equation. The uniform heat sources are shown in table 4.1. In the cathode and anode reac-

Table 4.1: Heat sources from Daun et al. [16] at a current density of 4000 [A/m^2]

Layer	Source term	
Anode	$q_{irr-an} = 0.6$	[kW/m^2]
	$q_{rev-an} = -0.6$	[kW/m^2]
Cathode	$q_{irr-cat} = 0.4$	[kW/m^2]
	$q_{rev-cat} = 1.7$	[kW/m^2]
Electrolyte	14.7×10^3	[kW/m^3]

tion areas both a 'reversible' and a 'irreversible' heat source are applied. This reversible heat source is caused by the entropy change of reaction. The irreversible heat source here is caused by overpotential in the reaction areas. These sources still have to be divided by the relevant zone thickness to obtain a volumetric heat source. The reaction area thickness is 1 [μm] for case one and 50 [μm] for case two. In the electrolyte an additional ohmic heat source is applied, which is caused by resistance against the flow of oxygen ions. From the table can be observed that the reversible heat source is negative at the anode side and positive at the cathode side.

This implies that the half-reaction at the anode side is endothermic, and the half-reaction at the cathode side exothermic. It is difficult to determine the heat sources associated with half-reactions, because state variables as entropy and enthalpy are not available for electrons and oxygen ions. There are however methods to estimate the entropy change of half-reactions in fuel cells, called Seebeck coefficient analysis [57]. This method is included in appendix **??**. With this method can be shown that the anodic half-reaction is indeed endothermic.

The material properties used are shown in table 4.2. In both Daun et al. [16] and Murthy and Fedorov [15] these same density and thermal conductivity are used. The specific heat is not specified in Murthy and Fedorov [15], so the values used in Daun et al. [16] are used. These properties are obtained from Daun et al.

Table 4.2: Material properties PEN-structure

	$\rho\left[\frac{kg}{m^3}\right]$	$C_p\left[\frac{J}{kgK}\right]$	$k\left[\frac{W}{mK}\right]$	$\kappa[m^{-1}]$	$\sigma_s[m^{-1}]$
Electrolyte	5160	400	2.16	260	1.00×10^4
Anode	3030	600	5.84	4.00×10^6	-
Cathode	3310	607	1.86	4.00×10^6	-

[16]. For the electrolyte both an absorption coefficient and a scattering coefficient are defined. Isotropic scattering is assumed. The extinction coefficient is defined as:

$$\beta_\lambda = \kappa_\lambda + \sigma_\lambda \tag{4.1}$$

Which is shown in the radiative transfer equation (Eq. (3.36)).

BOUNDARY CONDITIONS

At the walls on the left and right side of the domain symmetry boundary conditions are applied. At the anode and cathode external walls, which are the top and bottom of the domain, heat flux boundary conditions must be applied. Both convective and radiative heat transfer are present. There are different ways to treat a wall while using the discrete ordinates method.

Boundary conditions are shown in table 4.3. The walls can be considered semi-transparent or opaque.

Table 4.3: Boundary conditions

	Anode flow boundary	Cathode flow boundary
h_{conv} [W/m^2/K]	215	181
T_{flow} [K]	950	950
ϵ_{ext}	0.9	0.9
T_{rad} [K]	950	950

When defining an opaque boundary condition radiation is not allowed to pass through the wall. Instead the radiation can be absorbed in the wall or reflected back into the domain. It is more accurate to model the wall as a semi-transparent wall. This means radiation can be absorbed, reflected and transmitted trough the wall. When defining a wall thickness of 0 [mm] nothing will be absorbed or reflected. Instead radiation is allowed to leave the domain without interference of the wall, which is what happens at this porous surface. Radiation can also enter the domain by defining external radiation beams or by defining an external radiation temperature and emissivity.

The models developed here will use the semi-transparent boundary conditions. This is the most realistic one since radiation can exit and enter the material through the porous surface. A wall thickness of 0 [mm] is specified. Both convective and radiative heat transfer occurs at these walls. The convective heat flux is determined by:

$$q_{conv} = h_{ext}(T_{flow} - T_{wall}) \tag{4.2}$$

Radiation beams exit the domain at the top and bottom wall. An external emissivity and temperature are defined to simulate the radiation from the surrounding walls towards the domain. This external flux is determined with:

$$q_{rad,ext} = \epsilon_{ext}\sigma_{sb}T_{rad}^4 \tag{4.3}$$

4.2.2. CONVERGENCE

The obtained solution must be grid-independent, refining the mesh should not influence the results. It was found that the initial grid was already fine enough. Since these are simple cases it was chosen not to include this grid-independence check in this report. To check convergence the temperature at multiple points are monitored until they reach a stable value. Next the total heat flux leaving the domain is checked, this should equal the magnitude of the applied heat sources. This is done for each case.

A thing worth showing is the discretization of the discrete ordinates method. Increasing the amount of angular discretizations exponentially increases computation time. It is important to use the least amount of control angles while still obtaining good results. In table 4.4 the different settings that were used for the DO-method are shown. The results obtained with these different settings for both cases are shown in figure

Table 4.4: DO-settings

Legend	θ divisions	ϕ divisions	θ pixels	ϕ pixels
21	2	2	1	1
32	3	3	2	2
43	4	4	3	3
54	5	5	4	4
55	5	5	5	5

4.3a and 4.3b. Both the results from case one and two show that the setting '21' is already accurate enough.

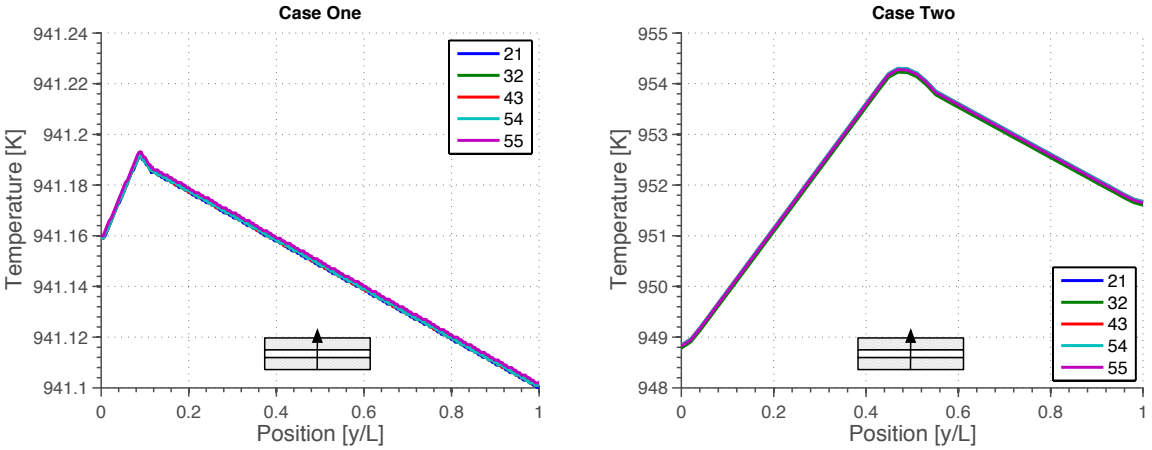

(a) (b)

Figure 4.3: Temperature profiles obtained in PEN-structure using different settings for the DO-method. (a) Case One (b) Case Two

In both models a temperature peak can be observed at triple phase boundary on the cathode side. Since in the electrolyte and the cathode heat sources are applied this is an expected result. The temperature profile obtained at case one is different than the temperature profile obtained in Daun et al. [16]. The temperature profiles in the article shows a decreasing temperature from the air side to the fuel side, while in the current models a peak occurs near the electrolyte. Also the temperatures are lower in the current models. This is caused by the simplifications applied here, the symmetric conditions and the heat flux boundary conditions result in different behavior of the model. The current models are however sufficient to check the effect of different radiative properties on the heat flows and temperatures within the domain. The obtained results are shown in the next section.

4.2.3. RESULTS

The standard radiative properties for the anode, cathode and electrolyte were given in the model description. These properties will be varied to see what the effects are on the temperature profiles and heat flows in the domain. This will show how important radiation in the different materials is, and whether it is important to

have a detailed understanding of the material properties. The properties of anode and cathode will be varied at the same time, since they are assumed to have properties in a similar range. The different absorption coefficients are chosen such that a large range of optical thicknesses is obtained. Optical thickness based on the extinction coefficient can be determined with:

$$\tau_\lambda = \int_0^s \beta_\lambda \mathrm{d}s \tag{4.4}$$

Changing the optical thickness over a large range will show what happens in the optical thin and the optical thick limit. For both case one and case two the range of absorption coefficients together with the corresponding optical thickness in anode and cathode are shown in table 4.5. The obtained temperature profiles in the

Table 4.5: Variation of anode and cathode absorption coefficient

(a) Case One

	κ	τ_{an}	τ_{cath}
A1	10	0.005	0.0005
A2	100	0.05	0.005
A3	1000	0.5	0.05
A4	10000	5	0.5
A5	100000	50	5
A6	1000000	500	50

(b) Case Two

Solution	κ	$\tau_{an,cath}$
A1	1	0.0025
A2	10	0.025
A3	100	0.25
A4	1000	2.5
A5	10000	25
A6	100000	250

PEN-structure are shown in figures 4.4a and 4.4b. Both figures show that increasing the absorption coefficient

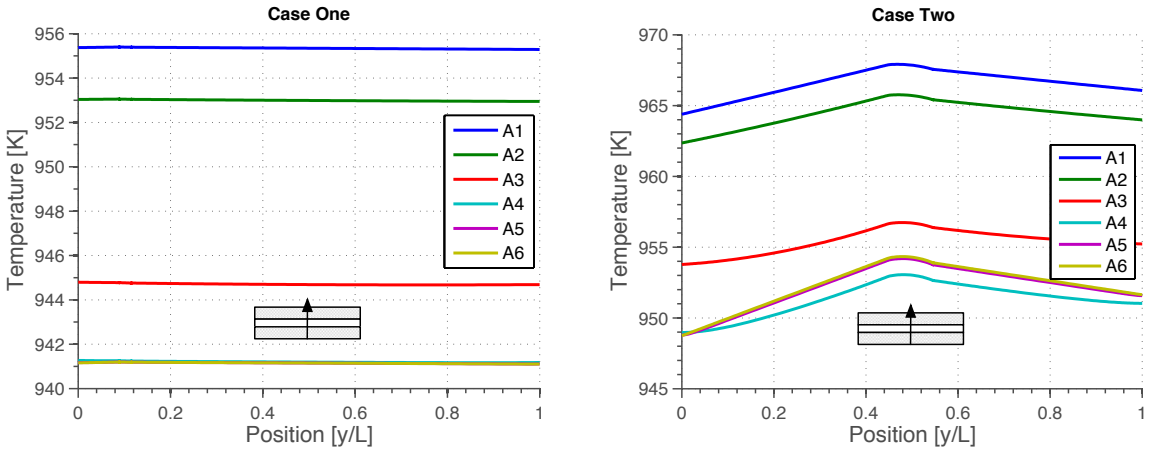

(a) (b)

Figure 4.4: Temperature profiles obtained with different anode and cathode absorption coefficients. (a) Case One (b) Case Two

lowers the temperature in the domain. A higher absorption coefficient means that the material emits more energy. The boundary condition temperatures are 950 [K], but for high absorption coefficients can be seen that the temperatures in the domain are below that value. At this stage the material is emitting more energy than it is receiving. This is caused by the external radiation boundary condition. The external emissivity and temperature are used to determine a flux of radiative intensity entering the domain. Using an emissivity of 0.9 and a temperature of 950 [K] will create the same irradation as an emissivity of 1 and a temperature of 925 [K]. When the temperature at the boundaries is lower then 950 [K] convection will transfer heat from the flows to the solid material. This is also possible in a more accurate fuel cell model. From the magnitude of heat flows and temperatures it is possible to determine the relevance of thermal radiation. The figures show that increasing the absorption coefficient of anode and cathode lowers the temperature in the domain, but after a certain value the temperatures remain at a constant level. For both cases this happens with the 'A5' and 'A6' case. At the values for 'A3' and 'A4' the optical thickness for both cases are around magnitude one, which can be observed by the non-linear behavior of the temperature profiles. This is clearly visible in 4.4b.

Since 950 [K] is not a very high temperature for SOFCs the same simulations are performed with the boundary condition temperatures at 1200 [K]. The obtained results are shown in figures 4.5a and 4.5b. These

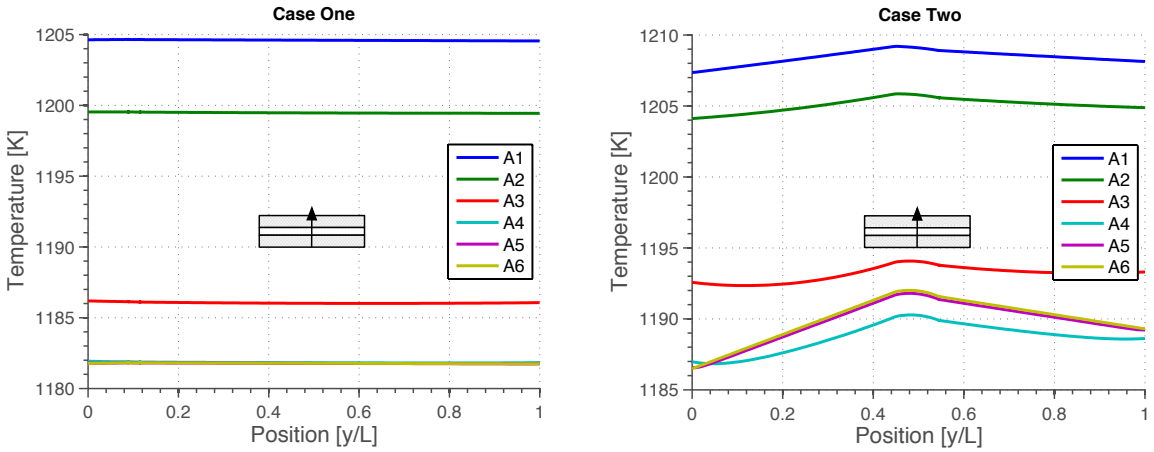

(a) (b)

Figure 4.5: Temperature profiles obtained with different anode and cathode absorption coefficients, temperature at boundaries 1200 [K]. (a) Case One (b) Case Two

figures show similar behavior as the 950 [K] cases. For high optical thicknesses the temperature profiles do not change anymore.

The results so far showed that at high optical thickness of the anode and cathode the temperature profiles in the domain do not change anymore. The absorption coefficients in literature are even higher then the values simulated here. Now it is interesting to see how what actually happens to the heat flows in the domain as function of these absorption coefficients. First a look is taken at the flow boundaries. The ratio of radiative heat flux to convective heat flux is shown in figures 4.6a and 4.6b. The results show that at very low optical

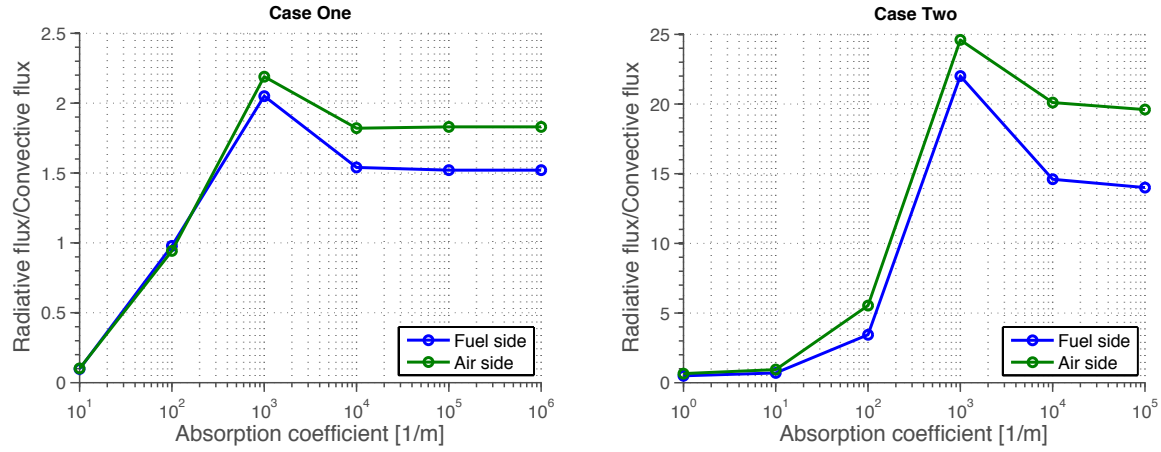

(a) (b)

Figure 4.6: Magnitude of radiative heat flux vs convective heat flux at flow channel walls as function of anode and cathode absorption coefficients. (a) Case One (b) Case Two

thickness the magnitude of radiation is small compared to the magnitude of convection. This is because the material is very transparent and emits almost no radiation. Increasing the absorption coefficient causes the radiative heat flux at the boundaries to increase. At high optical thicknesses the temperatures in the domain do not change anymore and the ratio of thermal radiation to convective heat transfer reaches a stable value. For case one it can be seen that the magnitude of thermal radiation is between 1.5 and 2 times higher. At case two this ratio is much higher. This is caused by the volumetric heat source in the electrolyte. Because the electrolyte is much thicker the net heat released in the electrolyte is much higher.

At the interface between anode/electrolyte and cathode/electrolyte the ratio of thermal radiation to conductive heat flux is investigated. The results are shown in figures 4.7a and 4.7b. These results show that at

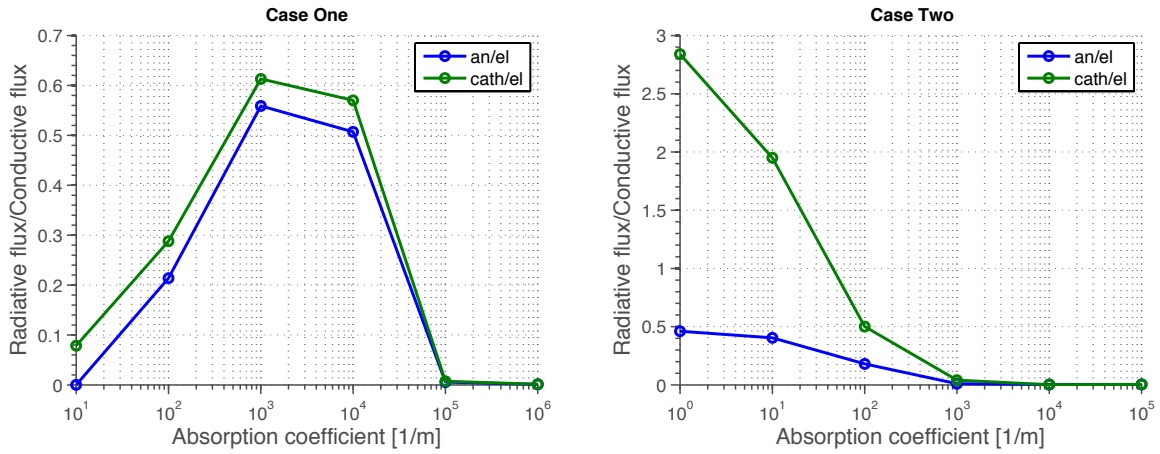

(a) (b)

Figure 4.7: Magnitude of radiative heat flux vs conductive heat flux at electrode/electrolyte interface as function of anode and cathode absorption coefficients. (a) Case One (b) Case Two

high absorption coefficients the ratio of radiation to conduction goes to zero. Which means internally there is no thermal radiation anymore. When looking at the combined results it can be concluded that radiation at the flow channels goes to a constant value for increasing optical thickness and the internal radiation goes to zero. From this it can be concluded that at high optical thickness the material behaves as an opaque material and only radiation at the surfaces is still important. This means the anode and cathode do not have to be modeled as participating media, but the radiation from the surfaces is important.

The literature study showed that radiation in the electrolyte has an negligible effect. To confirm this the optical properties of the electrolyte are varied. Both the anode and cathode absorption coefficients are set on their default values of 4.00×10^6 [1/m]. The different optical properties used for the electrolyte are shown in table 4.6. The obtained temperature profiles are shown in figures 4.8a and 4.8b. Case 7 represents the

Table 4.6: Electrolyte cases with different optical properties

Case	$\sigma_s = 1 \times 10^4$	Case	$\sigma_s = 0$
	κ		κ
1	260	4	260
2	2600	5	2600
3	26000	6	26000
		7	0

situation where both absorption and scattering coefficient are zero. Case 3 is the most optical thick case, with a high absorption coefficient and the default scattering coefficient. As shown in the figures, the effect on the temperature profiles is negligible. The results in [16] showed a decrease of approximately 0.5 [K] when including radiation in the electrolyte. In that model however the anode/electrolyte and cathode/electrolyte wall were modeled as opaque walls with an emissivity of 0.9. Overall it can be concluded that radiation in the electrolyte has negligible effect.

4.3. OBSERVATIONS

The temperature profiles obtained for case one show different behavior than the temperature profiles obtained in Daun et al. [16]. In the article the temperature decreases from the cathode side to anode side, where in the current models a temperature peak occurs near the electrolyte.

For case two the conclusions are similar to case one. This model was based on Murthy and Fedorov [15], where an even higher optical thickness is assumed for the anode and cathode ($\tau_{an/cat} = 10^4$). The results in

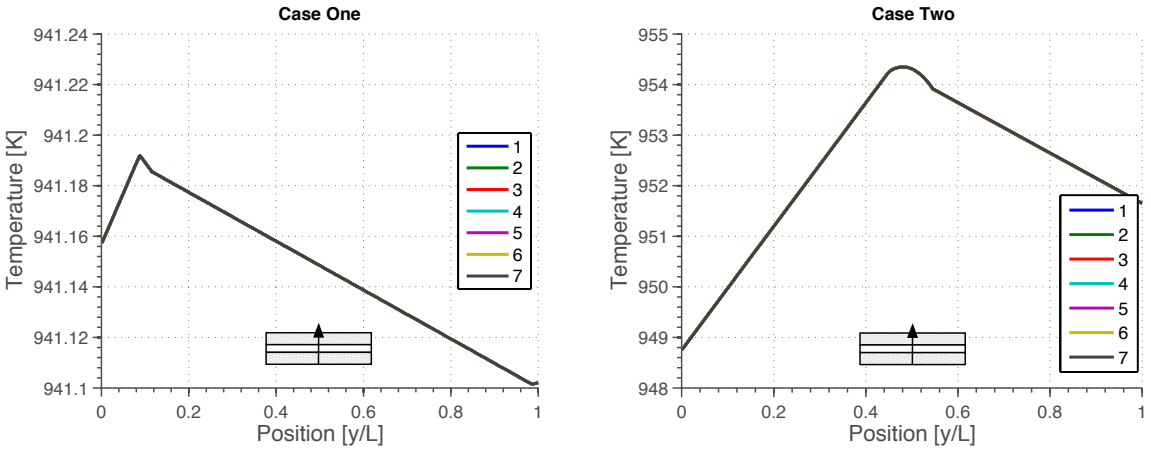

(a) (b)

Figure 4.8: Temperature profiles obtained in PEN-structure using different electrolyte optical properties. (a) Case One (b) Case Two

this article show a large temperature difference when radiation is included in the PEN-structure. From the current results can be concluded that this is caused by radiation emitting from the surface. A computation with only surface-to-surface radiation should give similar results. The large temperature difference in the article is probably caused by the applied thermal boundary conditions. The article is not very specific about this.

To obtain some more detailed results case one will be extended with flow channels to fully resemble the model from Daun et al. [16]. This model will be used to show the effect of radiation in the flow channels. Also the effect of including radiation in the PEN-structure will be studied, to confirm the conclusions based on the previous results.

4.4. 2D MODEL INCLUDING FLOW CHANNELS

The model developed here will use the same PEN-structure dimensions that were used in case one. The model is now extended with flow channels. The previous models used symmetry boundary conditions on the left and right wall, which forced the results to vary in only one direction. This model will give two dimensional results. The geometry is an exact copy of the geometry shown in Fig. 4.1a. A schematic of the geometry is shown in figure 4.9.

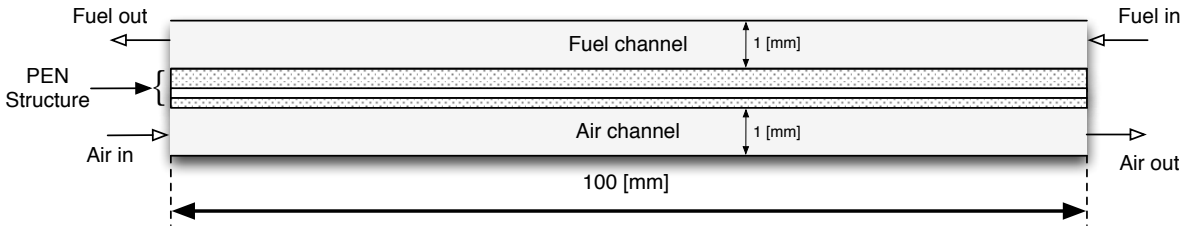

Figure 4.9: Geometry case three

4.4.1. MODEL DESCRIPTION

This model solves for the mass, momentum, species, energy and the discrete ordinate equations. The same material properties used for case one are applied here to the PEN-structure, and the same volumetric heat sources are applied. The inlet mass flows and compositions are shown in table 4.7. These values are obtained from Daun et al. [16]. All necessary properties are shown in table 4.7. The table shows that constant values are used for all gas properties. The gas properties used in the article are however a bit strange, which can be

Table 4.7: Parameters and Properties simulation Case Three

Parameter/Property	Air	Fuel
$\dot{m}_{in}$ [kg/s]	6.649×10^{-4}	6.452×10^{-4}
ρ [kg m^{-3}]	0.399	0.255
C_p [kJ kg^{-1}K^{-1}]	1.129	1.673
k [W m^{-1}K^{-1}]	0.067	0.08
y_{O_2}	0.225	0
y_{H_2}	0	0.85
y_{N_2}	0.775	0.10
y_{H_2O}	0	0.05

shown by calculating the fuel and air density using the ideal gas law(Eq. (3.62)). This results in:

$$\rho_{air}(T = 1073K) = \frac{101325}{8314 \cdot 1073\left(\frac{0.225}{32} + \frac{0.775}{28}\right)} = 0.3272 \quad [\text{kg/m}^3] \tag{4.5}$$

$$\rho_{fuel}(T = 1073K) = \frac{101325}{8314 \cdot 1073\left(\frac{0.85}{2} + \frac{0.10}{28} + \frac{0.05}{18}\right)} = 0.0263 \quad [\text{kg/m}^3] \tag{4.6}$$

The density of the fuel flow is an order of magnitude lower than the value shown in table 4.7. The computations will be performed with the properties shown in table 4.7 and the results compared to a situation with a more accurate property approximations. The results will show that this has a dramatic influence on the temperature field.

4.4.2. MESH

The geometry and mesh were created using Ansys ICEM CFD. To check mesh independence the problem was solved without radiation on three different mesh sizes. Temperature profiles along the cathode surface and in the PEN-structure were compared for these three meshes and shown in figures 4.10a and 4.10b. From these

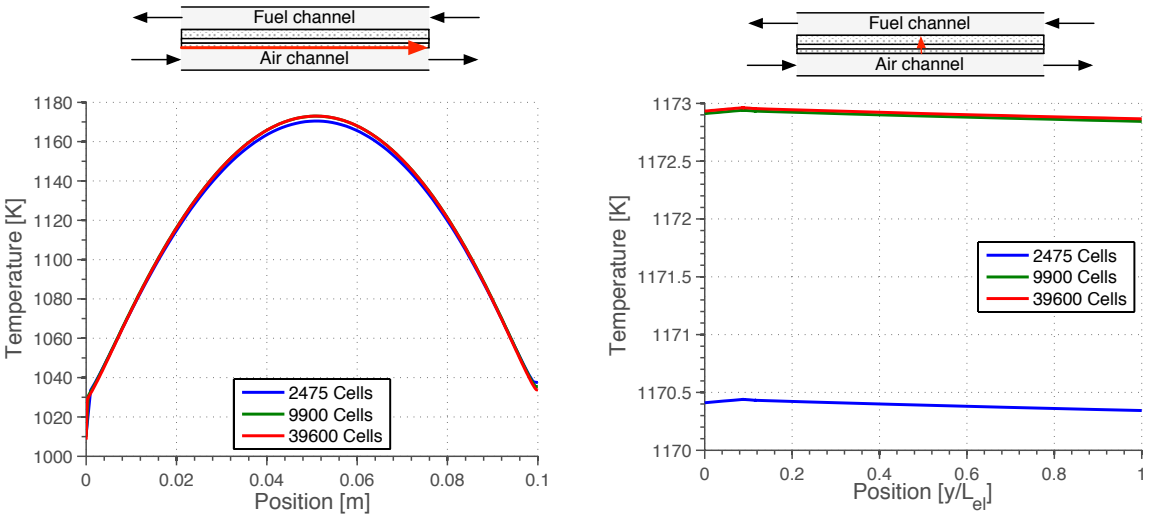

(a) (b)

Figure 4.10: Temperature profiles obtained using different grid sizes. (a) Temperature profile along cathode surface. (b) Temperature profile in PEN-structure

figures can be concluded that 9900 cells is sufficient to obtain good results.

4.4.3. RESULTS

This model is used to compare the following cases with each other:

- No radiation in solution domain
- Radiation only included in flow channels
- Radiation included in flow channels and PEN-structure

The results are obtained with different surface emissivities for the anode and cathode surface. Temperature profiles along the cathode channel are shown in figure 4.11. These results show that the temperature increases

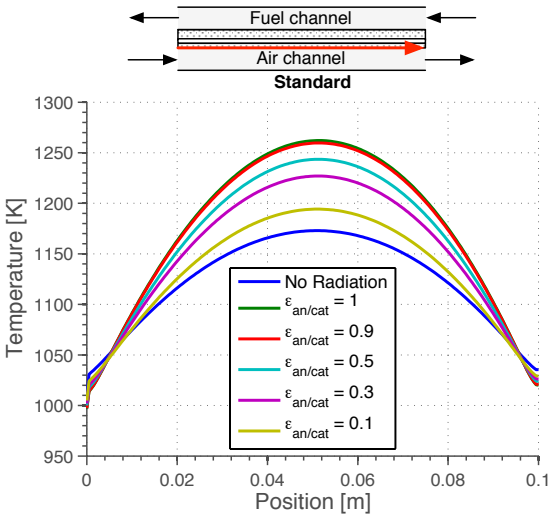

Figure 4.11: Temperature profiles obtained without radiation, and with surface-to-surface radiation for different anode and cathode properties

throughout the domain when surface-to-surface radiation is included. This is an unexpected result. An extra mode of heat transfer is expected to make the temperature field throughout the domain more uniform. It is however the case that all properties are considered constant. Assuming a constant density causes the flow field to be independent of temperature in this model. Also the assumption of specific heat does not make the solution any better. The flow is moving at a constant velocity, but more heat is transferred in the domain, which causes the temperatures to increase.

The same computation is performed with a more accurate approximation of the gas properties. The heat capacity, thermal conductivity and dynamic viscosity are made a function of temperature using the polynomials defined in section 3.5.2. Again the surface emissivities of the anode and cathode are varied. The results are shown in figures 4.12a and 4.12b. Figure 4.12a shows the temperature profile along the cathode flow channel for different surface emissivities and the case without radiation. The results show a small influence of thermal radiation on the temperature profiles, a completely results then shown in fig. 4.11. The lower fuel density causes a much higher velocity in the fuel channel, causing the temperature peak to shift to the left of the domain. In figure 4.12b three curves are shown, the case without radiation, the case with surface emissivities 0.9, and the case where all materials are participating in the radiative transfer equation. The standard optical values defined in section 4.2.1 are used for the anode, cathode and electrolyte. The results confirm the earlier conclusions, in the case of optical thick anode and cathode, the PEN-structure does not need to be considered as participating media. Only surface-to-surface radiation has effect. The temperature profiles obtained in the PEN-structure are shown in figures 4.13a and 4.13b. Figure 4.13a shows that the overall temperature in the PEN-structure decreases when surface-to-surface radiation is included. The maximum temperature difference between the cases is approximately 0.5 [K]. Figure 4.13b shows the temperature profile obtained when the PEN-structure is participating in the radiative transfer equation. The obtained temperature profile is identical to the temperature profiles obtained when only considering surface-to-surface radiation. This proofs the point that the PEN-structure can be considered opaque. In figure 4.14 temperature contours in the domain are shown for the case without radiation and a case with radiation. The temperature field is slightly different when including thermal radiation. When comparing the results to figures 2.5a and 2.5b it is obvious the results obtain here do not agree with the article. This is caused by the difference in gas properties.

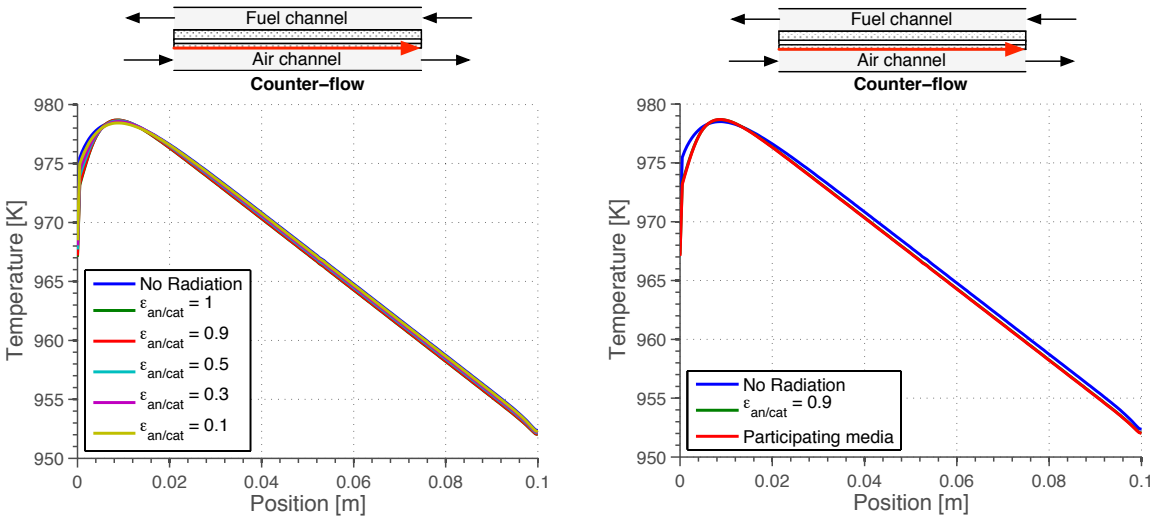

(a) (b)

Figure 4.12: Temperature profiles along cathode channel. (a) The case without radiation is compared to cases with different anode and cathode surface emissivities. (b) The case without radiation is compared to a case with surface-to-surface radiation, and a case where the PEN-structure is participating in the RTE.

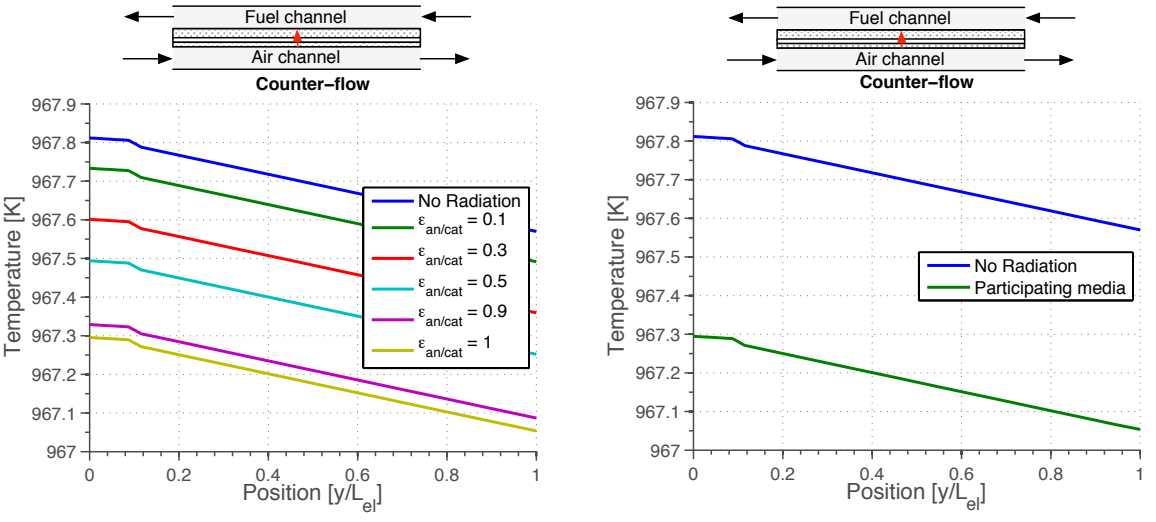

(a) (b)

Figure 4.13: Temperature profiles in PEN-structure. (a) The case without radiation is compared to cases with different anode and cathode surface emissivities. (b) The case without radiation is compared to a case where the PEN-structure is participating in the RTE.

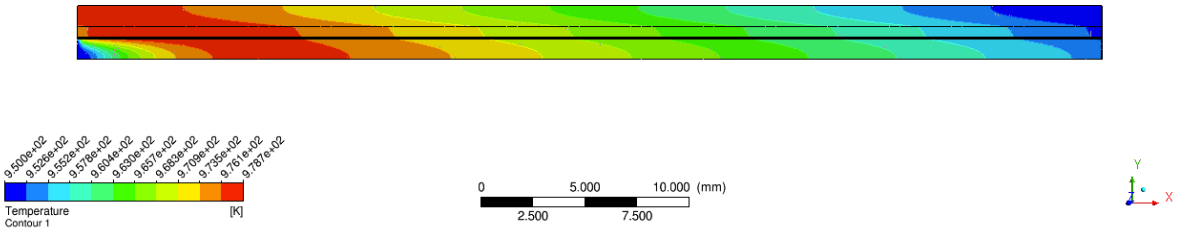

(a)

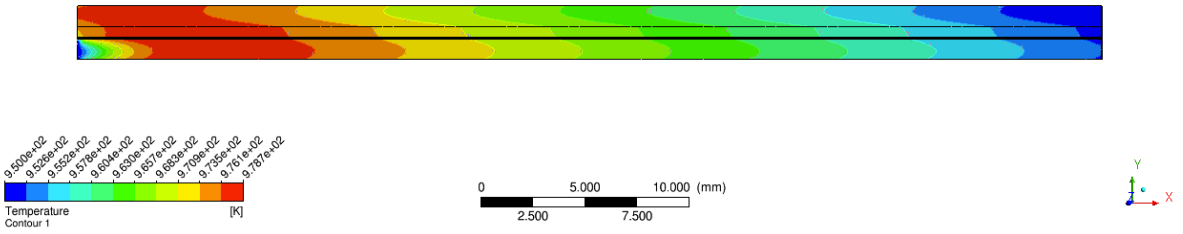

(b)

Figure 4.14: Contour plot of temperature in domain, figures are scaled in x-direction. (a) Case without radiation. (b) Case with surface-to-surface radiation and emissivities 1.

CO-FLOW

An extra case study is performed to study what happens when the previous model has a co-flow arrangement instead of counter-flow. All other model settings are identical. Temperature profiles obtained along the cathode flow channel are shown in figure 4.15. Temperature profiles obtained in the PEN-structure are shown in figure 4.16b. These results show that the fuel flow has a large influence on the temperature profiles. For the case without radiation the temperature profiles increase more or less linear along the flow channel. When including thermal radiation a small decrease of temperature can be observed near the end of the flow channel. This is caused by radiation exiting the domain.

4.5. CONCLUSIONS

The preliminary models (without flow channels) showed that increasing the absorption coefficients of anode and cathode causes a lower temperature in the PEN-structure. This is caused by the emission of more radiation. When going to the optical thick limit the internal radiative heat flux goes to zero, where at the flow boundaries it goes to a constant value. This constant value is the consequence of thermal boundary conditions. This means in the optical thick limit only surface-to-surface radiation will be important.

The model with the flow channels verified this. From the results obtained here can be concluded that radiation has a very small effect on the temperatures in the domain. Temperature differences in the order of magnitude of 1 [K] are obtained. These simulations also verified that including radiation in the PEN-structure indeed gives identical results when considering the PEN-structure opaque.

A lot of simplifications were applied in the previous models. No electrochemical reaction were included, and the uniform heat sources are a questionable assumption. In the following chapter a more accurate mathematical representation of a solid oxide fuel cell will be used.

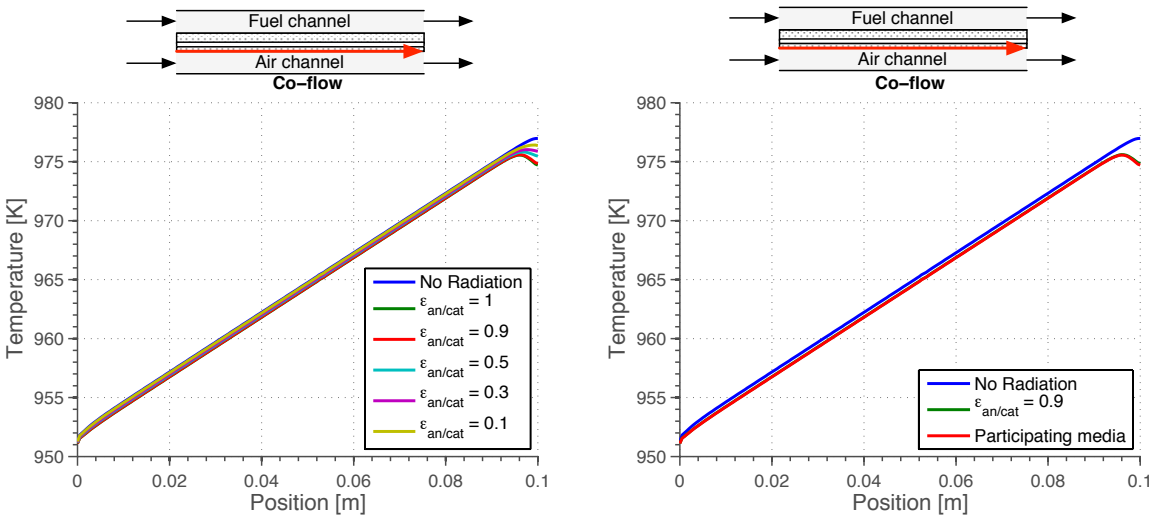

(a) (b)

Figure 4.15: Temperature profiles obtained along cathode flow channel for co-flow arrangement. Comparing the case without radiation, case with all materials participating, and surface-to=surface radiation using different surface emissivities.

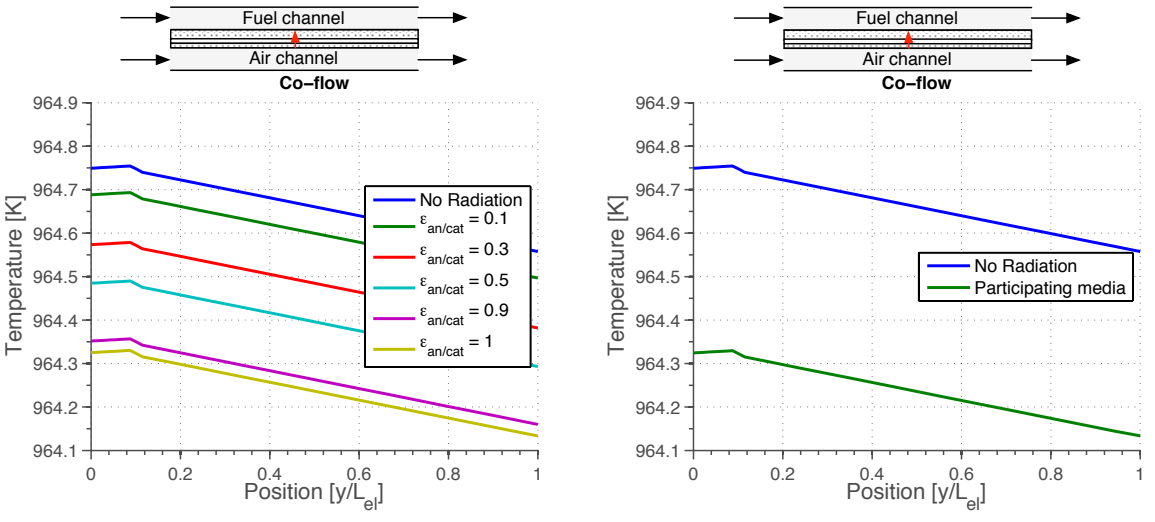

(a) (b)

Figure 4.16: Temperature profiles in PEN-structure. (a) The case without radiation is compared to cases with different anode and cathode surface emissivities. (b) The case without radiation is compared to a case where the PEN-structure is participating in the RTE.

5

3D MODEL OF A SINGLE CHANNEL PLANAR SOFC

5.1. INTRODUCTION

The previous chapter showed the effect of thermal radiation in the PEN-structure on the temperature field in 2D-models. However, these models were subject to a lot of simplifications. The most debatable simplification is probably the assumption of uniform heat sources.

This chapter will describe the development of a 3D-model of a single channel planar SOFC. The geometry of this model will be based on the geometry of the 2D-models. Instead of only solving the flow and energy equations this model will solve for for mass, momentum, species, energy and potential conservation using the 'fuel cell and electrolysis' model (see chapter 3). This set of equations is a more accurate mathematical representation of what is going on the fuel cell.

This is a theoretical case study and the results are difficult to validate. Where possible the results will be compared with literature [24, 28].

5.2. MODEL DESCRIPTION

A schematic of the model geometry is shown in Fig. 5.1. The geometry is based on the 2D-geometry from Daun et al. [16] which was used in the previous chapter. The total front width is 3 [mm], the total height 3.565 [mm], and the length of the cell is 100 [mm]. The flow channels are 2 [mm] wide and 1 [mm] high. The domain also included current collectors. These enclose the flow channels and are necessary to solve the potential equations. The dimensions of the anode, cathode and electrolyte are similar to the dimensions

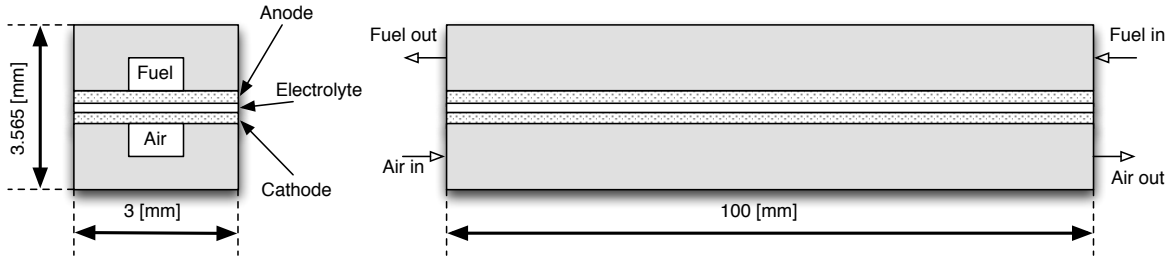

Figure 5.1: Planar single channel SOFC geometry

used in the 2D models, and are included in table 5.1. The reaction zones (TPBs) are included as separate zones in the model domain, instead of lumping them onto an interface with the electrolyte. This should result in more accurate results, since in actual SOFCs these reaction areas are also considered as separate zones. The operating conditions of the fuel cell will be based on a uniform current density of 4000 [A/m^2], based on literature and similar to the previous chapter[16].

Table 5.1: Dimensions planar cell

Input	Value	Units
t_{anode}	500	[μm]
$t_{cathode}$	50	[μm]
$t_{electrolyte}$	15	[μm]
t_{tpb-an}	1	[μm]
$t_{tpb-cat}$	1	[μm]

5.2.1. PROPERTIES

The model equations for the 'fuel cell and electrolysis' module were discussed in chapter 3. All the necessary electrochemical and material properties will be discussed here.

To drive the reactions away from equilibrium and obtaining a net current an overpotential is necessary in both reaction areas. The relation between current density and overpotential is described with the Butler-Volmer or the Tafel equation. The Tafel equation is a simplification of the Butler-Volmer equation in the high-overpotential limit and is not used here to obtain the final results. Both equations contain the exchange current density, $i_{0,ref}^{cat/an}$, which is a measurement of the reaction kinetics in both anode and cathode. When developing fuel cell materials an important goal is to increase the exchange current densities at similar conditions. These values can be made temperature dependent using a Arrhenius like equation, as shown in equations (5.1) and (5.2).

$$i_{0,ref}^{cat} = \gamma_{cat} \exp\left(-\frac{E_{act,cat}}{RT}\right) \tag{5.1}$$

$$i_{0,ref}^{an} = \gamma_{an} \exp\left(-\frac{E_{act,an}}{RT}\right) \tag{5.2}$$

The activation energy, $E_{act,cat/an}$, and the pre-exponential factors $\gamma_{cat/an}$ are obtained from literature[58]. These values are shown in table 5.2. The exchange current densities are calculated at a temperature of 1073 [K] and included as constants in the model, the obtained values are also included in table 5.2. The local current density in the fuel cells is dependent on concentration of the gaseous species, known from the Butler-Volmer equations (eq. (3.8)). For this dependence a reference concentration $X_{i,ref}$ and a concentration exponent γ_i are needed. These values are also obtained from literature[58], and included in table 5.2.

These reactions kinetics are obtained from literature [58]. The exchange current densities, $i_{0,ref}^{cat/an}$, are a measurement of the speed of the reactions, and when developing materials for fuel cells it is always attempted to improve these values. The activation energy $E_{act,cat/an}$ and pre-exponononential factors $\gamma_{cat/an}$ are obtained from literature and shown in table 5.2 [58].

Table 5.2: Electrochemical parameters

Property	Anode	Cathode	Units
$\zeta_{an/cat}$	$2 \cdot 10^6$	$2 \cdot 10^6$	[1/m]
α_{an}	0.5	0.5	[-]
α_{cat}	0.5	0.5	[-]
$E_{act,an/cat}$	$100 \cdot 10^3$	$120 \cdot 10^3$	[J/mol]
$\gamma_{an/cat}$	$5.50 \cdot 10^8$	$7.00 \cdot 10^8$	[A/m^2]
$X_{H_2,ref}$	1	-	[mol%]
$X_{O_2,ref}$	-	1	[mol%]
γ_{H_2}	1	-	[−]
γ_{O_2}	-	0.25	[−]
$i_{0,ref}^{an/cat}$	7460	1007	[A/m^2]

The material properties of the anode, cathode, electrolyte and current collector are shown in table 5.3. These properties are obtained from literature[59]. In chapter 3.5.2 temperature dependent functions for C_p, k and μ are defined. It was chosen to only make the heat capacity temperature dependent here. Making

Table 5.3: Material properties

		Anode	Cathode	Electrolyte	Current collector
ϵ	[−]	0.5	0.5	-	-
τ	[−]	6	6	-	-
α	$[m^2]$	$1.00 \cdot 10^{-8}$	$1.00 \cdot 10^{-8}$	-	-
ρ	$[kg/m^3]$	3030	3310	5160	7450
C_p	$[J/kgK]$	600	607	400	600
κ	$[W/mK]$	5.84	1.86	2.16	27
σ	$[1/\Omega m]$	$3.03 \cdot 10^4$	$1.28 \cdot 10^4$	-	$7.69 \cdot 10^5$

all properties dependent on temperature induced more instability. Values for the thermal conductivity and dynamic viscosity are obtained at 1073 [K].

For the radiative transfer equation the optical properties of all participating media must be defined. The anode, cathode and electrolyte are not considered as participating in this model which means only the gas properties must be defined. These are calculated using the WSGG-model, described in section 3.5.2.

5.2.2. BOUNDARY CONDITIONS

At the fuel and air inlet 'mass-flow-inlet' boundary conditions are applied. The mass flow, temperature and composition of the flow must be given here. The mass flows will be calculated by assuming a uniform current density of 4000 [A/m^2]. This rather large current density is chosen because a large current density causes more reaction heating and irreversible losses. From the half-reactions (3.1) and (3.2) it is known that for each reacting hydrogen molecule 2 electrons are released, and for each reacting oxygen molecule 4 electrons are consumed. The Faraday constant, F, is used to relate the current output of the fuel cell to the amount of hydrogen and oxygen that is needed. The mass flow of air is determined using equation (5.3).

$$\dot{m}_{air} = \frac{i \cdot A_{act}}{n \cdot F} \cdot \frac{M_{O_2}}{u_{O_2} \cdot Y_{O_2}} = \frac{4000 \cdot 3 \cdot 10^{-4}}{4 \cdot 96485} \cdot \frac{32}{0.1 \cdot 0.20} \cdot 10^{-3} = 4.74 \cdot 10^{-6} \quad \text{[kg/s]} \tag{5.3}$$

The mass flow of fuel is determined using:

$$\dot{m}_{fuel} = \frac{i \cdot A_{act}}{n \cdot F} \cdot \frac{M_{H_2}}{u_{H_2} \cdot Y_{H_2}} = \frac{4000 \cdot 3 \cdot 10^{-4}}{2 \cdot 96485} \cdot \frac{2}{0.8 \cdot 0.8} \cdot 10^{-3} = 1.94 \cdot 10^{-8} \quad \text{[kg/s]} \tag{5.4}$$

Where A_{act} is the active area of the fuel cell, u_i is the utilization factor of species i and Y_i is the inlet concentration of species i. The active area of this single channel cell is $3 \cdot 10^{-4}$[m^2], which means the total output current is 1.2 A. The factors u_i are used because not all oxygen and hydrogen will be utilized. This is to reduce concentration losses. The inlet concentration of hydrogen is 80% H_2, and the inlet concentration of oxygen is 20% O_2. These are normal gas compositions for SOFCs. The inlet temperatures of both streams are 973 [K]. All these input parameters are summarized in table 5.4. The fuel and air outlet are defined as 'pressure outlet' at

Table 5.4: Operating conditions and input parameters

Input	Value	Units
$m_{anode-in}$	$1.94 \cdot 10^{-8}$	[kg/s]
$T_{anode-in}$	973	[K]
$m_{cathode-in}$	$4.74 \cdot 10^{-6}$	[kg/s]
$T_{cathode-in}$	973	[K]
Anode inlet composition	80% H_2, 20% H_2O	[wt%]
Cathode inlet composition	20% O_2, 80% N_2	[wt%]
Average current density	4000	[A/m^2]
Oxygen utilization	0.1	-
Fuel utilization	0.8	-

atmospheric pressure. For the energy equation all the boundaries of the domain except the inlets and outlets are considered adiabatic.

POTENTIAL EQUATIONS

The boundary conditions necessary for the potential field are applied at the external contact surfaces of the current collectors at both anode and cathode side. At the anode current collector a potential of 0 [V] is applied. At the cathode side either a current or a potential may be applied. Both the air and fuel mass flow were determined here using an assumed current density of 4000 [A/m^2]. It is convenient to apply this value as a boundary condition on the cathode side, since the resulting hydrogen and oxygen consumption must then match the calculated values. It is however more realistic to apply a potential boundary condition instead of a current density. The computations here will use the current density BC for convenience. It will be discussed how this influences the solution. At all other exterior walls a zero current boundary condition is applied.

RADIATION BOUNDARY CONDITIONS

During development of this model it was discovered that Fluent does not have a proper way to calculate radiative heat transfer in porous materials. This problem can be explained using figure 5.2. The boundary

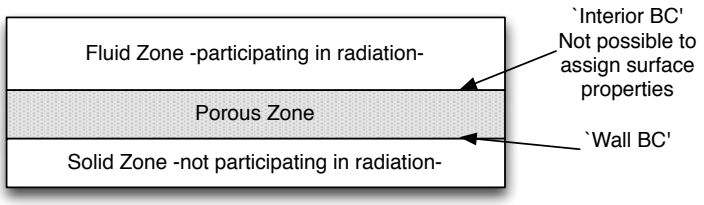

Figure 5.2: Type of boundary conditions for different cell zones

condition on the interface between the porous zone and the fluid zone is an interior boundary condition. This is necessary to solve the flow and species equations between both zones. On this interior wall it is not possible to assign any boundary conditions. This is a problem if surface-to-surface radiation is to be studied between in the fluid zones, and optical properties must be assigned to the surface of the porous material.

Porous materials are considered fluid zones in Fluent. Even though absorption coefficients can be specified for the solid materials, only fluid absorption will be calculated when considering the porous zone as participating in radiation. When considering the zones as not participating, radiation will only be solved in the flow channels. This interior wall is then treated as a black surface with a surface emissivity of 1. No other values can be assigned to this interface[1].

The porous zones will be considered as not participating, which according to the results from the previous chapter is a good assumption. The surface emissivity of the anode and cathode will be equal to 1. According to the previous chapter the solution is not very sensitive to this property. The results obtained in this chapter will show if radiation has a larger effect on this 3D-model. If so, it will be necessary to solve the problem described above, to be able to more accurately model thermal radiation. For the default situation the emissivities of the other surfaces, the current collector surfaces enclosing the flow channels, will be assigned a value of 0.9.

5.2.3. MESH

The geometry is created using Autodesk Inventor. The mesh is created using Ansys ICEM CFD. The first mesh developed contains 18.424 cells and is very coarse as shown in figure 5.3a. This mesh is refined twice to study mesh dependency of the solution, these finer grids are shown in figures 5.3b and 5.3c. The fine grid contains 91.740 cells. The cells in the current collector domain are still reasonably coarse. Since this is a high electrically conducting material the potential gradients will be very small here, and reasonable results should be obtained. The model is run with these different grid sizes and the temperature and hydrogen mass fraction are plotted along the anode channel. This is shown in figure 5.4a and figure 5.4b. The hydrogen mass fraction is similar for the different grid sizes. The temperature profiles along the anode channel show differences for the different grid sizes. The first two meshes clearly show the discretization in the z-direction is too coarse, unnatural kinks can be observed in the temperature profile. The grid with 91.740 does show nice behavior.

[1]This is a well known problem. A topic on this problem can be found on `http://www.cfd-online.com/Forums/fluent/48421-fluent-radiation-porous-media.html`. Attemps have been made to solve this problem with user defined functions. However it appears that a UDF cannot be assigned to an interior wall

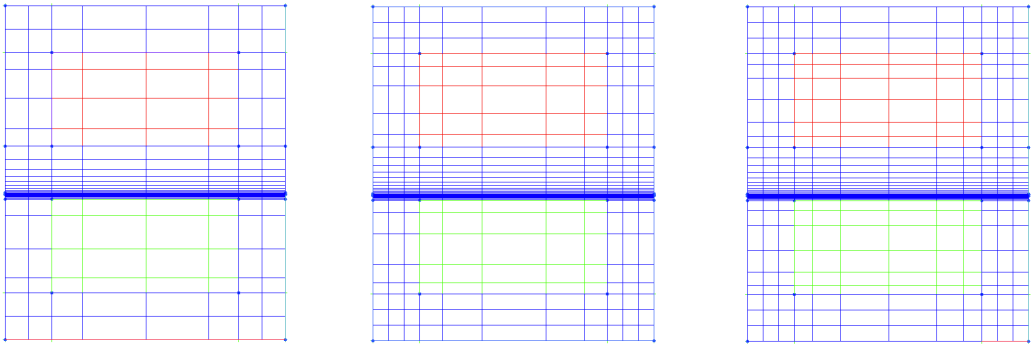

(a) (b) (c)

Figure 5.3: Mesh comparison. (a) 18.424 Cells. (b) 46.057 Cells. (c). 91.740 Cells

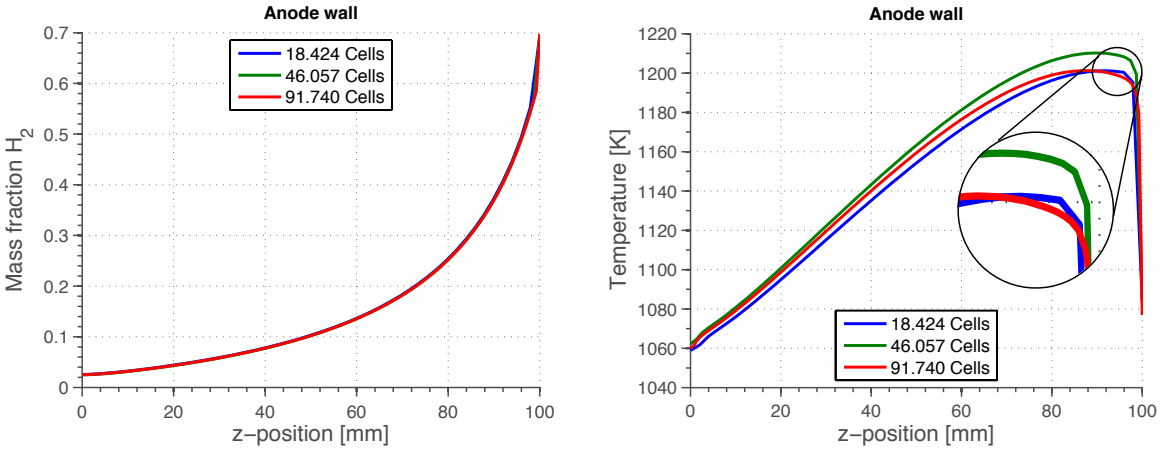

(a) (b)

Figure 5.4: Mesh comparison. (a) 18.424 Cells. (b) 46.057 Cells. (c). 91.740 Cells

The surface integral of Y-direction current density on both bottom and top results in 1.2 [A], which means there is electrochemical balance in the equations.

In the flow direction of the mesh no refinement has been done yet. At the inflow and outflow regions the mesh is refined extra. This resulted in a mesh with 104.940 Cells. As a final step mesh adaptation in Fluent can be applied to obtain a grid with 8 times as many cell, which means 839.520 cells. Temperature profiles obtained with these last three grids along the anode channel are shown in figure 5.6. As can be seen, the mesh with 104.940 cells results in lower temperatures. This is caused by the high gradients at the inlet and outlet. The grid size near the inlet and outlet of the domain is very important. Here temperature gradients are large, and the concentration of hydrogen is at is maximum at the inlet, which means electrochemical reactions will have optimal conditions there. The temperature profile obtained with 839.520 Cells is close to the 104.940 cell mesh, but the temperature peak observed is lower.

Vector plots of the current density are shown in figure 5.5 for both the two final meshes. These results show that a good initial solution can be obtained when using 104.940 Cells. This mesh will be used to obtain initial solutions and the large mesh is used to obtain the final solution. This results in much lower computation times compared to starting with the large mesh. Figures of this final mesh are shown in figure 5.7a and 5.7b to get an impression of the amount of cells.

5.3. CONVERGENCE

To prevent unstable convergence behavior, a combination of the right solver settings together with a delicate solution procedure was necessary. For future users of this add-on module these settings and procedures are

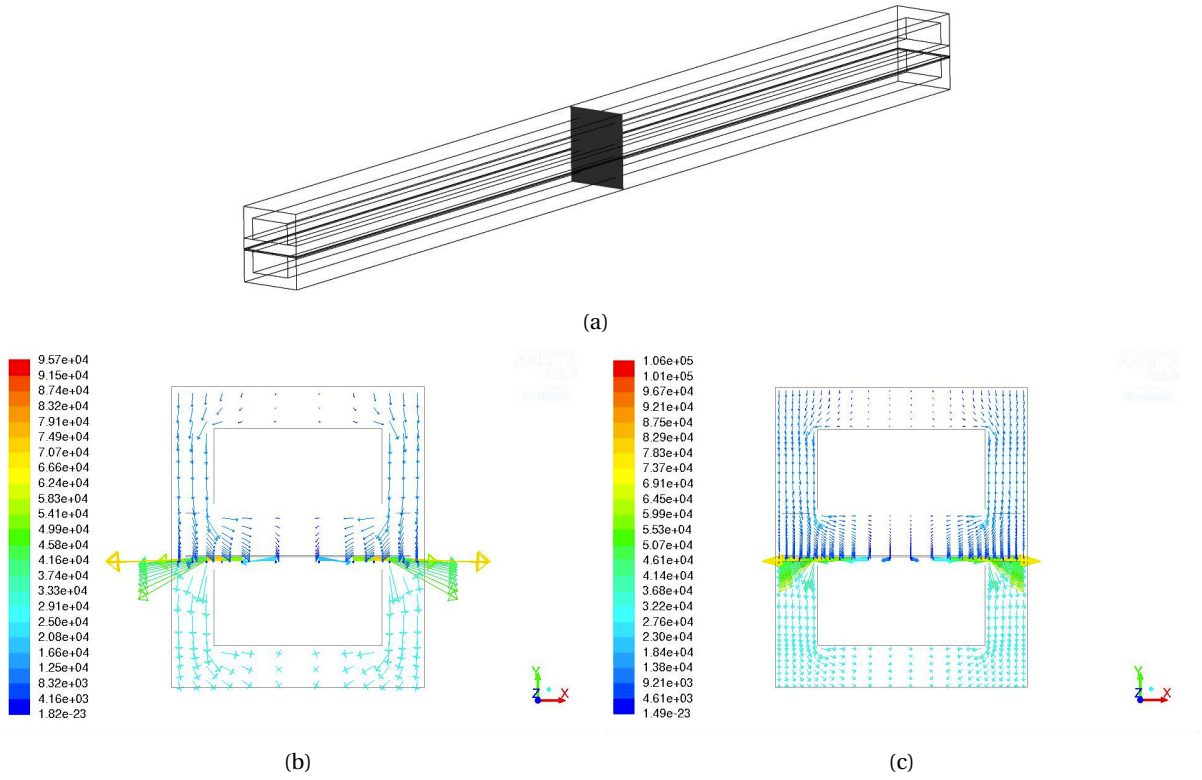

Figure 5.5: Current density vector plot, colored by current density magnitude in [A/m^2]. (a) Plane indicated location of contour plots. (b) 104.940 Cells. (c) 839.520 Cells

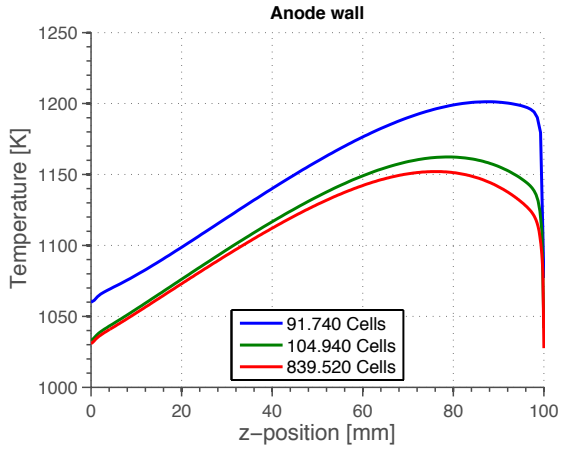

Figure 5.6: Temperature profile along anode channel for different grid sizes

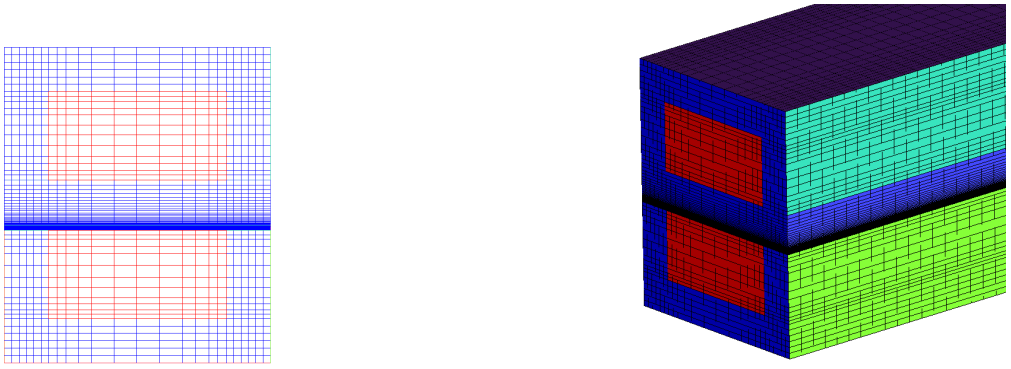

(a) (b)

Figure 5.7: Final mesh containing 839.520 Cells

included in the appendix B. To check whether the solution is actually converged it is necessary to make sure the mass and heat balances are correct. The command `/report/species-mass-flow` gives the mass flow of species at the domain boundaries and a net balance of the amount consumed/produced. The amount of hydrogen and oxygen consumed can be used to determine whether this accounts for the specified current output. This is done using equation 5.5.

$$I = \frac{\dot{m}_{cons,i}\, nF}{M} \quad [\text{A}] \tag{5.5}$$

Where $\dot{m}_{cons,i}$ is the net consumed mass of species i. This convergence check is performed using both the consumed hydrogen and oxygen, in table 5.5 the results of this analysis are shown. The second column shows the net consumed oxygen mass flow, the third column the associated current, and the fourth column the deviation from the expected current. The last three column show the same procedure for the consumed hydrogen flow. The largest deviation encountered in the current cases is 0.313%, which is considered acceptable. With

Table 5.5: Convergence check different cases

Case	$\dot{m}_{cons,O_2}$ [kg/s]	I_{O_2} [A]	Deviation [%]	$\dot{m}_{cons,H_2}$ [kg/s]	I_{O_2} [A]	Deviation [%]
CC $\epsilon = 0.3$	9.980E-08	1.204	0.313	1.250E-08	1.200	-0.026
CC $\epsilon = 0.5$	9.980E-08	1.204	0.307	1.250E-08	1.199	-0.048
all $\epsilon = 0.9$	9.970E-08	1.202	0.159	1.250E-08	1.200	-0.032
No radiation	9.960E-08	1.201	0.071	1.250E-08	1.199	-0.065

the final mesh the solution is obtained first using 2ϕ and 2θ angular discretizations for the DO-method. The final solution is obtained with 4ϕ and 4θ angular discretizations. More angular control volumes were not used for practical reasons since this caused the computational time to increase to several days for each case.

5.4. RESULTS

The Reynolds number is 4.95 in the fuel channel and 141.56 in the air channel, which means the flow is indeed laminar as assumed in the modeling approach. The Lewis number is from unity, which species diffusion cannot be neglected in the energy equation, as assumed in the modeling approach. The Brinkman number is much smaller than unity, which shows that viscous heating can indeed be neglected, as assumed. Temperature contour plots are shown in figure 5.8. These contour plots show that the temperature gradient is dominant in z-direction. In y-direction there is not much temperature variation. Including radiative heat transfer changes the temperature contours only a little bit. To have a more closer look on the influence of thermal radiation the temperature profiles are plotted along the anode surface. These results are shown in figure 5.9. These results show the temperature profile obtained without radiation, and the temperature profiles obtained using different current collector emissivities. It seems that radiation has a very small influence on on the temperature profiles, the largest temperature difference is approximately 5 [K]. Also the current collector surface emissivities do not seem to be important. Temperature profiles in the center of the air channel

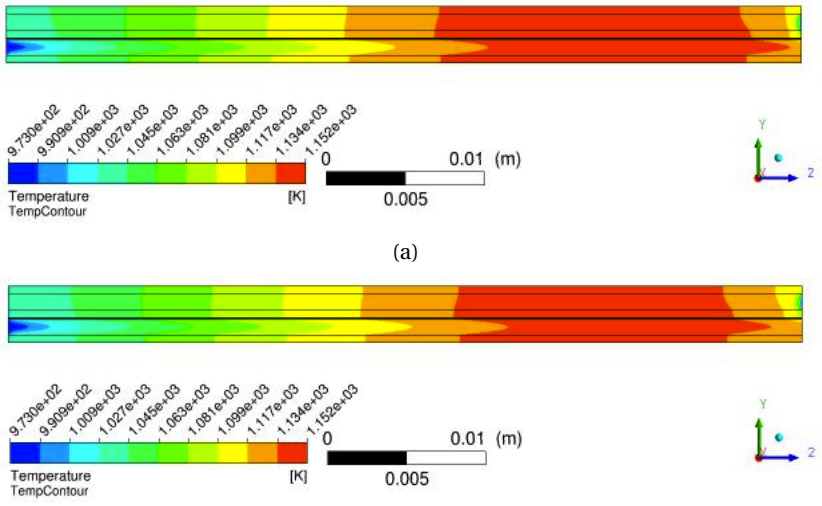

(a)

(b)

Figure 5.8: Temperature contours. (a) Without radiation. (b) With radiation

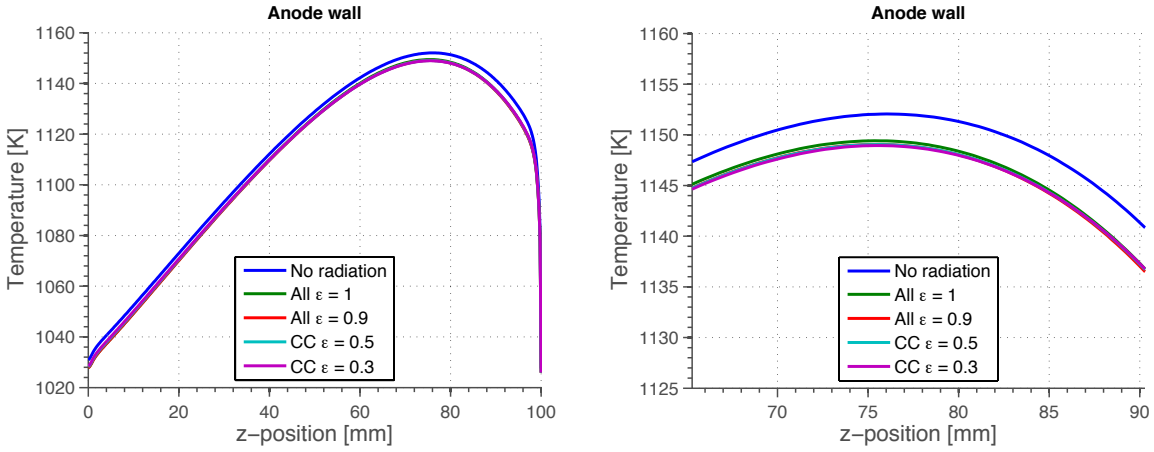

(a)

(b)

Figure 5.9: Temperature profiles with/without radiation for different surface properties

are shown in figure 5.10. The influence of radiation on the temperature profiles again seems to be minimal. This is logical since temperature gradients are only significant in flow direction. Radiation effects are dominant perpendicular to the flow direction, and the net radiation between two gray planar surfaces can be expressed using:

$$q_{net} = \frac{\sigma(T_1^4 - T_2^4)}{\frac{1}{\epsilon_1} + \frac{1}{\epsilon_2} - 1} \tag{5.6}$$

If the temperatures T_1 and T_2 are very close to each other the net radiative heat flux will be small. In table 5.6 the average heat fluxes are shown calculated at the anode current collector surface. The total, radiative and convective heat flux are shown. The last row shows the percentage of radiative heat transfer at this surface compared to the total heat flux. The radiative heat flux decreases as the current collector surface emissivity decreases. When all emissivities are 1 only 8.7% of the total heat flux is due to radiative heat transfer. It can be safely assumed that radiative heat transfer can be neglected. The WSGGM is used to determine the influence of gas components. The only participating component is H_2O. The temperature profile obtained with and without the participating gas is shown in figure 5.11. It shows to have zero influence on the temperature profile, which is an expected result. It was already shown that radiation has minimal effect on the temperature profiles in the computational domain. Only water vapor is present as participating gas, but can be considered

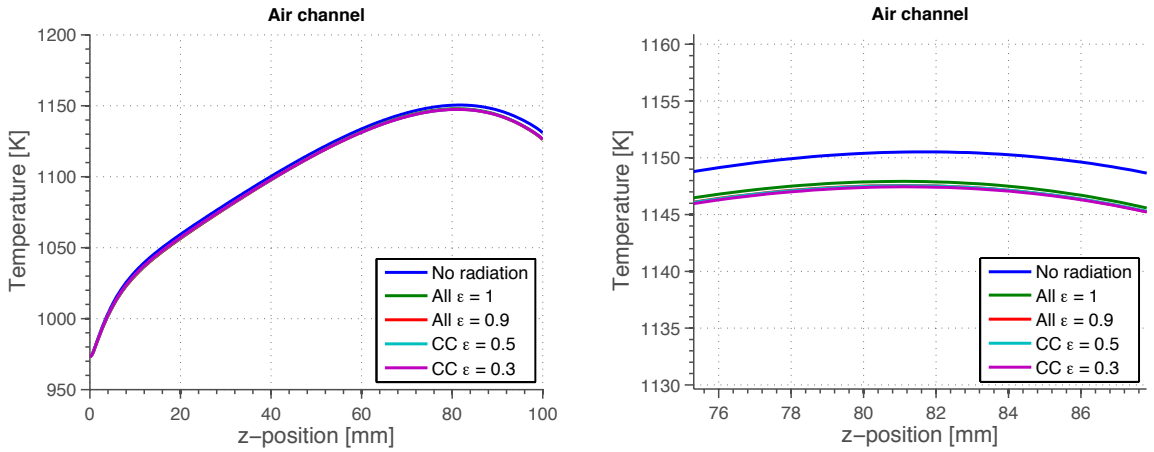

(a) (b)

Figure 5.10: Temperature profiles with/without radiation for different surface properties

Table 5.6: Average heat fluxes at anode current collector surface

	All $\epsilon = 1$	All $\epsilon = 0.9$	CC $\epsilon = 0.5$	CC $\epsilon = 0.3$	No radiation
q_{total} [W/m^2]	659.20	663.20	655.28	650.86	658.28
$q_{radiation}$ [W/m^2]	57.21	33.60	20.15	12.76	-
$q_{convection}$ [W/m^2]	601.99	629.59	635.14	638.10	658.28
$q_{radiation}/q_{total} \times 100$	8.68%	5.07%	3.07%	1.96%	0.00%

optical thin in this geometry.

The results obtained from this model can be compared to results from literature. The temperature difference when including radiation is similar to results obtained by [24], where radiation is studied in a single channel planar SOFC. These results are shown in figure 5.12a. These results from literature are for co-flow single channel SOFCs. The results from Qu et al. [24] show a slightly larger temperature difference, but also not very significant. The results from DiGiuseppe [28] show a large temperature difference. The computational mesh presented in this paper is however very coarse, and the previous results in this chapter show the results are very sensitive to the computational mesh.

In chapter 4 uniform heat sources were applied to obtain a simplified model. The current model can show the actual distribution of those heat sources. The volumetric reaction heat source along the electrolyte surface is shown in figure 5.13. It is obvious that assuming uniform heat sources is a wrong assumption. The average volumetric heat source is $1.53 \cdot 10^9$ [W/m^3], but the distribution shows values ranging from 1.2 to $2 \cdot 10^9$ [W/m^3]. A contour plot of the ohmic heat source is shown in figure 5.14.

5.5. REMARKS

A limitation of this model is that there is no correct way of modeling radiative heat transfer in the anode and cathode. Both the anode and cathode are considered porous media, which in the model are considered fluid domains. The optical properties in these materials are therefore the optical properties of the gases. This means there is less resistance against radiative heat transfer in the anode and cathode, which will result in lower temperatures at the electrolyte. The net radiative heat flux cannot be larger than shown in the current results.

A constant current density was defined as boundary condition at the cathode side, while it is more realistic to define a constant potential. This type of boundary condition was chosen because this forces the model to consume the same amount of hydrogen and oxygen for the different case studies. This results in similar heat sources. It is more accurate to subscribe a constant potential at the current collectors. Although the choice of boundary conditions change the distribution of current and potential throughout the domain, it was found that the influence on the temperature field was very small.

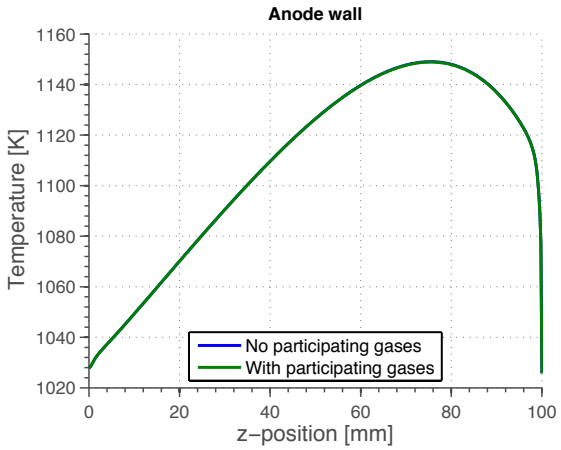

Figure 5.11: Influence of participating gas on temperature profile at anode wall

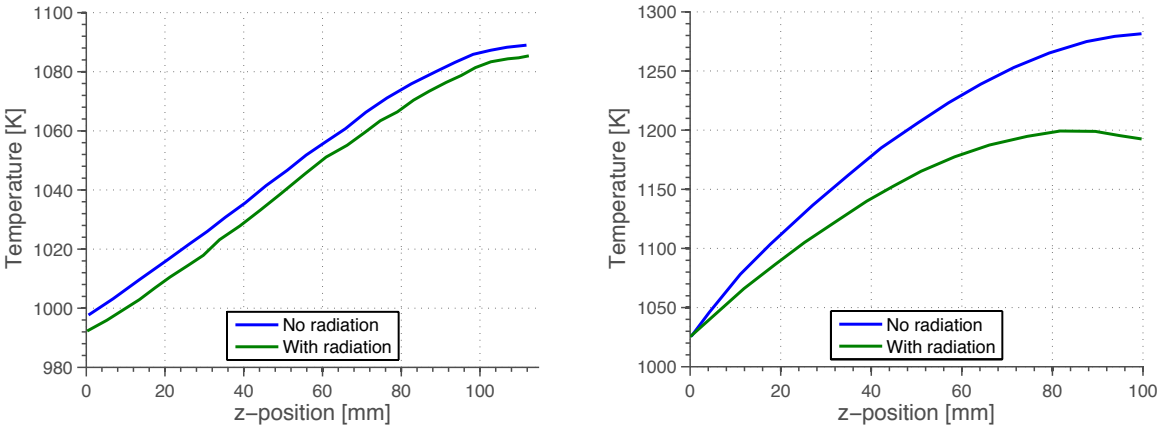

Figure 5.12: Results from literature. (a) Temperature profiles from Qu et al. [24]. (b) Temperature profiles from DiGiuseppe [28].

All the reaction heat in the current model is released in the anode triple phase boundary. In literature the anode side is also often used at the location for the reaction heat source. This assumption is however wrong [57]. This can be shown by having a closer look at the heat released at each half-reaction(or single electrode reaction). In appendix A is shown how the heat sources can be determined using a Seebeck coefficient analysis. This shows that the half-reaction at the anode is in fact endothermic, while the half-reaction at the cathode is strongly exothermic. It is expected however that implementing these half-reaction heat sources in the current model will not lead to different conclusions with respect to thermal radiation or with respect to temperature gradients.

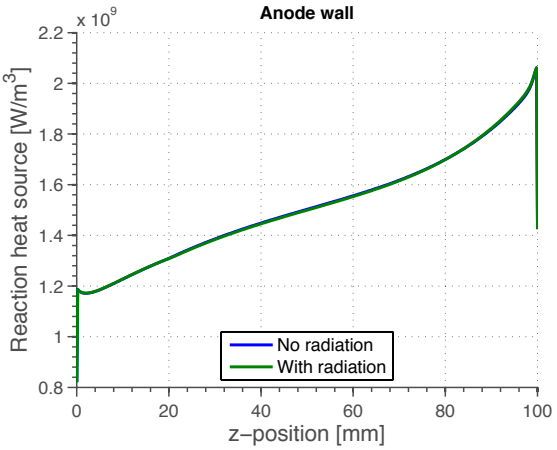

Figure 5.13: Reaction heat at electrolyte surface

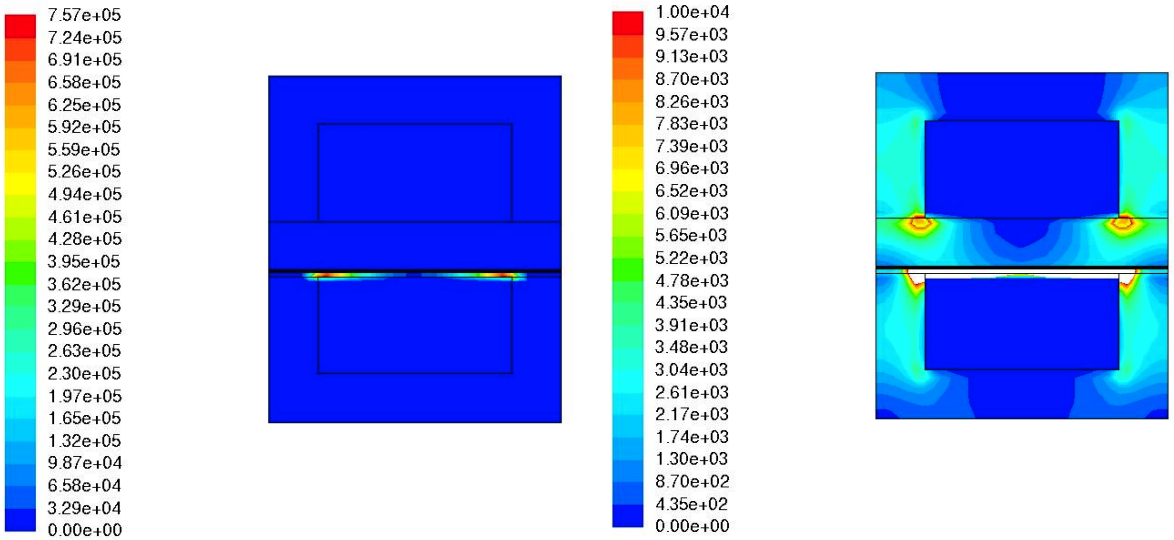

(a) (b)

Figure 5.14: Contour plots of ohmic heat source in [W/m^3]. (a) Auto range of values. (b) Maximum value limited to 10.000 [W/m^3].

6

3D MODEL OF A TUBULAR SOFC

6.1. INTRODUCTION

This chapter describes the development of a 3D-model of a Tubular SOFC. This model is based on a anode supported tubular cell, while most tubular cells are cathode supported. This specific design was chosen because this type of SOFC is currently being studied at the Delft University Of Technology, which means experimental data will be available for validation. The next sections describe the fuel cell geometry, material and electrochemical properties and simulation results. This model has not been studied yet with the inclusion of thermal radiation. It is expected that thermal radiation has a larger effect on this type of fuel cell then the effect shown in the 3D planar cell in chapter 5. Therefore recommendations will be given for future research.

6.2. MODEL DESCRIPTION

A schematic of the SOFC geometry is shown in figure 6.1. Fuel flows on the inside of the cell and air on the outside. The dimensions of this cell are given in figure 6.1 and table 6.1.

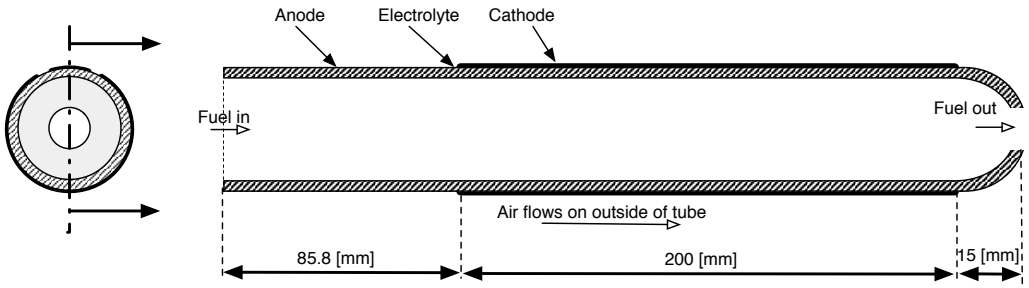

Figure 6.1: Schematic representation of anode supported tubular SOFC

A cylindrical oven is used to perform experiments on this fuel cell. The outside diameter of the model geometry is equal to the inner cylinder of the oven. A schematic of the experimental set-up together with the simplified model domain are shown in figure 6.2. Instead of using the fuel injection tube, and the holes in the oven for air inlets and outlets, the entire areas at the bottom and top of the domain are modeled as inlet and outlet. This is chosen to simplify the mesh.

The system of equations associated with the 'SOFC with Unresolved Electrolyte' module is solved here. This means the electrolyte and reaction areas are not included in the domain but instead lumped onto an interface between the cathode and the anode. This is done for practical reasons. The reaction areas would become so thin it would be very difficult to create a reasonable mesh, the difference between the reaction area dimensions and the other zones in the domain was simply very large. A picture of this cell is shown in figure 6.3. The tube is mainly made of anode material($NiO + ZrO_2$) . The outside surface of the cell is covered with a thin layer of electrolyte material(YSZ). The black areas shown in picture 6.3 are thin layers of cathode

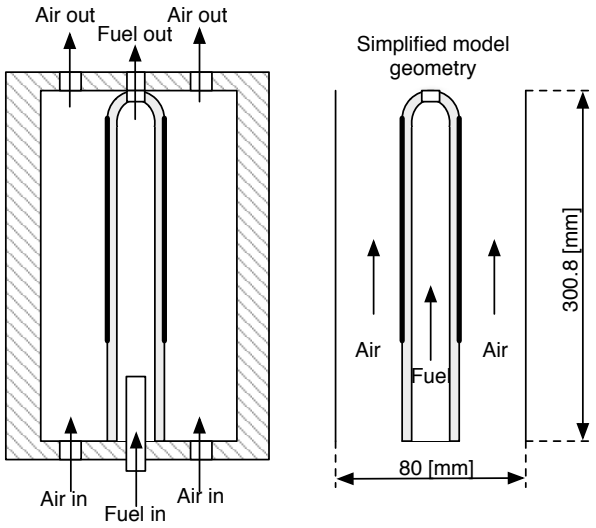

Figure 6.2: Schematic of experimental set-up

Table 6.1: Dimensions tubular cell

Input	Value	Units
d_{in}	17.4	[mm]
d_{out}	22.7	[mm]
t_{anode}	2	[mm]
$t_{cathode}$	30	[μm]
$t_{electrolyte}$	30	[μm]

material(LSM). The surface area covered by the cathode material is the active area of the fuel cell. The metal wire shown in the picture acts as current collector. The current collectors will be simplified in the model geometry and represented by solid strips.

There is limited information available about this cell. This means for all electrochemical and material properties reasonable assumptions are made based on literature. All information given by Nova Scientific Resources, the supplier of this fuel cell.

6.3. PROPERTIES

As mentioned the material properties of this cell are not well known. The properties necessary for the electrochemical reactions are based on literature[58], the same properties used for the Planar Cell in chapter 5. The exchange current densities are again determined at a temperature of 1073 [K] using equations (5.1) and (5.2), and are shown in table 6.2. The reference concentrations, $X_{i,ref}$, and the concentration exponents are also included in table 6.2.

The material properties of the anode, cathode and current collector are shown in table 6.3. These properties are obtained from literature [59]. The heat capacity of each species is determined using a polynomial dependent on temperature which is defined in section 3.5.2. The thermal conductivity and dynamic viscosity of each species are taken at 1073 [K] and remain constant in the domain.

For the radiative transfer equation the optical properties of all participating media must be defined. The anode, cathode and electrolyte are not considered as participating in this model which means only the gas properties must be defined. These are calculated using the WSGG-model, described in section 3.5.2.

Figure 6.3: Picture of tubular SOFC

Table 6.2: Electrochemical parameters

Property	Anode	Cathode	Units
$\zeta_{an/cat}$	$2 \cdot 10^6$	$2 \cdot 10^6$	[1/m]
α_{an}	0.5	0.5	[-]
α_{cat}	0.5	0.5	[-]
$E_{act,an/cat}$	$100 \cdot 10^3$	$120 \cdot 10^3$	[J/mol]
$\gamma_{an/cat}$	$5.50 \cdot 10^8$	$7.00 \cdot 10^8$	[A/m^2]
$X_{H_2,ref}$	1	-	[mol%]
$X_{O_2,ref}$	-	1	[mol%]
γ_{H_2}	1	-	[−]
γ_{O_2}	-	0.25	[−]
$i_{0,ref}^{an/cat}$	7460	1007	[A/m^2]

6.4. BOUNDARY CONDITIONS

To determine the inlet mass flows an average current density of 1500 [A/m^2] is assumed. The active surface area is given by:

$$A_{act} = \pi \cdot D \cdot L \frac{360-86}{360} = \pi \cdot 22.7 \cdot 200 \cdot 10^{-6} \cdot \frac{360-86}{360} = 0.0109 \quad [\text{m}^2] \tag{6.1}$$

Multiplying the active area with the current density results in a total current of 16.28 [A]. From this current the flow of electrons and the inlet mass flow of oxygen and hydrogen can be determined.

$$\dot{m}_{air} = \frac{i \cdot A_{act}}{n \cdot F} \cdot \frac{M_{O_2}}{u_{O_2} \cdot Y_{O_2}} = \frac{1500 \cdot 0.0109}{4 \cdot 96485} \cdot \frac{32}{0.233 \cdot 0.1} \cdot 10^{-3} = 5.795 \cdot 10^{-5} \quad [\text{kg/s}] \tag{6.2}$$

The mass flow of fuel is determined using

$$\dot{m}_{fuel} = \frac{i \cdot A_{act}}{n \cdot F} \cdot \frac{M_{H_2}}{u_{H_2} \cdot Y_{H_2}} = \frac{1500 \cdot 0.0109}{2 \cdot 96485} \cdot \frac{2}{0.8 \cdot 0.8} \cdot 10^{-3} = 2.637 \cdot 10^{-7} \quad [\text{kg/s}] \tag{6.3}$$

Table 6.3: Material properties tubular cell

		Anode	Cathode	Electrolyte	Current collector
ϵ	[−]	0.4	0.4	-	-
τ	[−]	6	6	-	-
α	[m^2]	$1.00 \cdot 10^{-8}$	$1.00 \cdot 10^{-8}$	-	-
ρ	[kg/m^3]	7740	5300	6000	7450
C_p	[J/kgK]	600	607	400	600
κ	[W/mK]	6	10	2.7	27
σ	[$1/\Omega m$]	$3.03 \cdot 10^4$	$1.28 \cdot 10^4$	-	$7.69 \cdot 10^5$

Note that these mass flows must be divided by 2 since only half of the geometry is modeled. All necessary boundary conditions for the flow equations are shown in table 6.4. The fuel and air outlet are specified at

Table 6.4: Operating conditions and input parameters

Input	Value	Units
m_{fuel}	$2.637/2 \cdot 10^{-7}$	[kg/s]
$T_{anode-in}$	1073	[K]
m_{air}	$5.795/2 \cdot 10^{-5}$	[kg/s]
$T_{cathode-in}$	1073	[K]
Anode inlet composition	80% H_2, 20% H_2O	[wt%]
Cathode inlet composition	23.3% O_2, 76.7% N_2	[wt%]
Average current density	1500	[A/m^2]
Oxygen utilization	0.1	-
Fuel utilization	0.8	-

pressure-outlets at atmosheric pressure. The furnace wall is considered adiabatic for the energy equation.

POTENTIAL EQUATION

To solve the potential equation it is necessary to specify a 'voltage tap surface' and a 'current tap surface'. The voltage tap surface is the external contact surface of the anode current collector. The current tap surface is the external contact surface of the cathode current collector. At the anode side a potential of [0] is applied. The Nernst equation, eq. 3.16, is used to determine the ideal voltage on the 'lumped' interface. In the graphical user interface a total output current is specified to which the solution must converge.

Located between the current collector surfaces and the furnace wall is the air domain. Specifying the outside surfaces of the current collectors resulted in erratic results. Because the contact surfaces are not on the outside of the domain the model tried to solve the potential field in the air domain. This problem is solved by turning the symmetry plane of the domain into a wall. This way the current collector surfaces on this wall can be specified as the external contact surfaces. The wall adjacent to fluid domains are specified as adiabatic for the energy equation and zero shear stress for the momentum equations, thereby obtaining symmetry.

RADIATIVE HEAT TRANSFER

The problem described in section 5.2.2 also applies here. The porous regions cannot be modeled correctly together with radiative heat transfer. Another problem is that the symmetry plane is specified as a wall in this model. For the flow and energy equations symmetry is still satisfied by specifying zero shear stress and adiabatic boundary conditions. It is more complicated for the radiative transfer equation. The wall can be either considered semi-transparent or opaque. Semi-transparent will mean that radiation can escape the domain here, which is not desired. When specifying the wall as opaque surface properties must be specified. A surface emissivity of 1 will mean this symmetry plane is considered as a black wall. Radiation is absorbed, increasing the wall temperature and radiation will be emitted from this wall. A surface emissivity of 0 will have the effect that all radiation is reflected back into the domain, basically turning this symmetry plane into a mirror. The best solution is to specify an emissivity of 0, and complete specular reflection.

The problem that radiation is not correctly solved in the porous materials is causing the results to be wrong, since most of the geometry is build of anode material. Before obtaining solutions with radiative heat transfer this problem must be solved. At the results only solutions without radiative heat transfer are presented.

6.5. MESH

The geometry is created using Autodesk Inventor and a structured mesh is developed using ICEM CFD. The initial mesh contains 95.132 Cells. This mesh is developed coarse, but fine enough to capture the essential features of the geometry. Also convergence is very slow with this mesh size, so the solution is only obtained using this mesh. At the results is discussed where mesh refinement might be necessary. Note that only half of the geometry is modeled here due to symmetry considerations. Figure 6.4 shows what the mesh looks like.

Figure 6.4b shows the actual domain used to solve the equations, in figure 6.4a this mesh is mirrored to show how it would look like on the complete domain. In figure 6.5 the mesh of the actual fuel cell is shown without

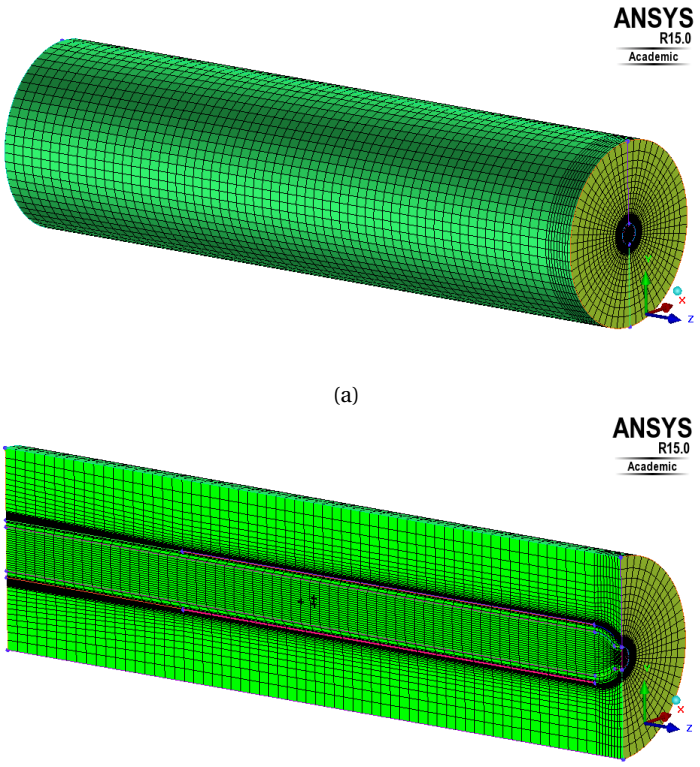

(a)

(b)

Figure 6.4: Tubular Cell Mesh

the air and fuel domain. One of the problem sections in this mesh is shown in figure 6.6. The nodes at the outlet of the fuel cell have been merged in order to obtain the sharp edge. This however causes ugly cells which induce instability in the solution process. These cells are in the anode domain, where species diffusion occurs. Since the model behavior is very sensitive to the species solver settings, these cells are one of the reasons for causing problems.

6.6. CONVERGENCE

A specific set of solver settings together with a delicate solution procedure was followed to obtain a converged solution. For future users of the 'SOFC with Unresolved Electrolyte' module is included in the appendix B.

The air and fuel mass flows were determined using an average current density of 1500 $[A/m^2]$. In the user interface of the model a total output current must be specified to which the model converges. This could be interpreted as a representation of an external load. To obtain a solution first the set of equations is solved at zero current output. The current is gradually increased until the required external load is reached. When increasing the output current above 2 [A] the model becomes unstable. This is a problem that needs to be solved. Still, the results obtained with this current output are discussed here. The average current density at this output is 368.55 [A/m^2]. Again one of the important measurements of convergence the species balance. The amount of consumed hydrogen and oxygen must account for the correct output current. This is checked using the following equation:

$$I = \frac{\dot{m}_{cons,i}\, nF}{M} \quad [\text{A}] \tag{6.4}$$

The results of this analysis is shown in table 6.5. The current output associated with the consumed species is about 0.25% higher than the specified current output.

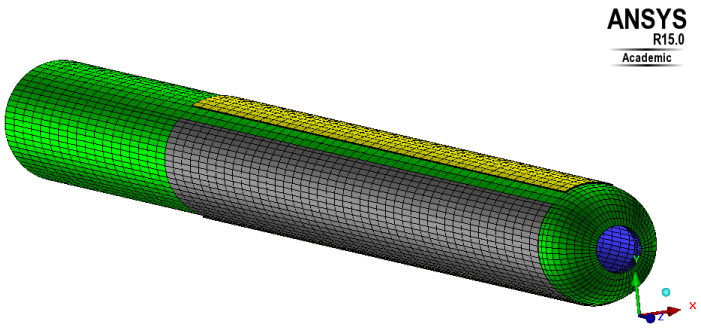

Figure 6.5: Mesh of the fuel cell without the air and fuel domain

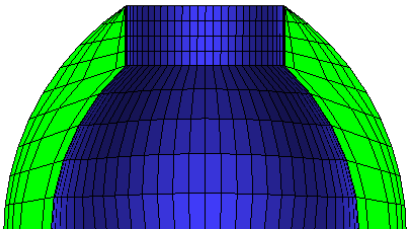

Figure 6.6: Mesh at fuel cell outlet, the cells in the sharp edge can be a reason for instability of the model.

6.7. RESULTS

Only results without radiative heat transfer are presented here, since no accurate solution could be obtained while including it. Solving this problem is future work.

The results obtained without radiation and at an output current of 2 [A] are shown to be reasonable. The output cell voltage is 0.942 [V]. When looking at conventional polarization curves in textbooks [4] this is a reasonable voltage at low current output. density is relatively low this high voltage is reasonable. The highest Reynolds number occurring in the fuel flow is 4.05 and the Reynolds number in the air flow is 26.65, which means the flow is laminar. The Reynolds number of the fuel flow is determined at the outlet of the flow since the velocity is at its highest here. To show this an contour plot of the velocity is shown in figure 6.7. Similar to the planar cell it is expected that the most heat will be generated at areas of high hydrogen concentration, at the beginning of the cell. This is the case with the current results. Both fuel and air flow temperatures along the active cell area, which is shown in the temperature contour plot in figure 6.8. Highest temperatures are observed in the fuel channel. The temperatures in the air and fuel channel are shown in figure 6.9. It is expected that radiation will have a larger effect on the temperature field than the effect shown at the planar SOFC models. This is expected because the temperature difference in axial direction is larger than the temperature difference in the planar SOFC models.

6.8. VALIDATION

The results obtained cannot be validated yet because experimental data has not yet become available. For future work with this CFD-model it is advised to optimize the grid first. Validation of the fuel cell is possible by measuring the polarization curve of the fuel cell. Measuring the fuel cell potential at different external loads will give show the behavior of the potential vs the output current. To validate the temperatures obtained by the model a thermographic camera can be used to determine the temperatures on the outside surface of the

Table 6.5: Convergence check using consumed species

$\dot{m}_{cons,O_2}$ [kg/s]	I_{O_2} [A]	Deviation [%]	$\dot{m}_{cons,H_2}$ [kg/s]	I_{O_2} [A]	Deviation [%]
1.662E-07	2.005	0.253	2.095E-08	2.005	0.253

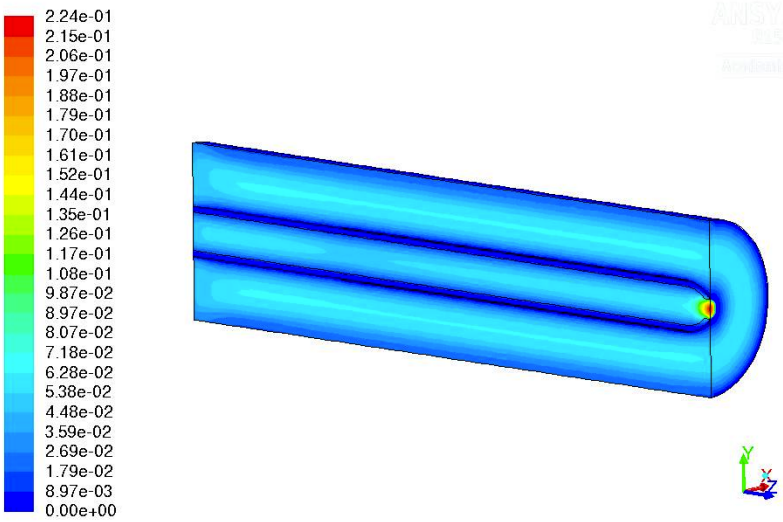

Figure 6.7: Contour plot of velocity in [m/s]

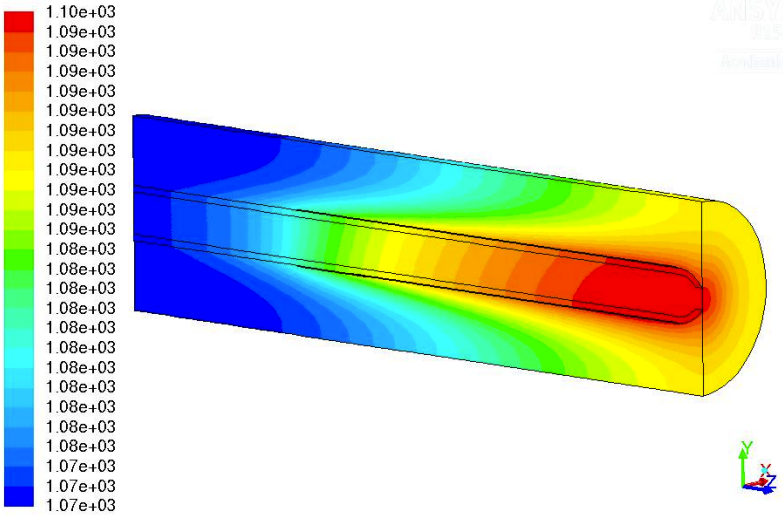

Figure 6.8: Contour plot of temperature in [K]

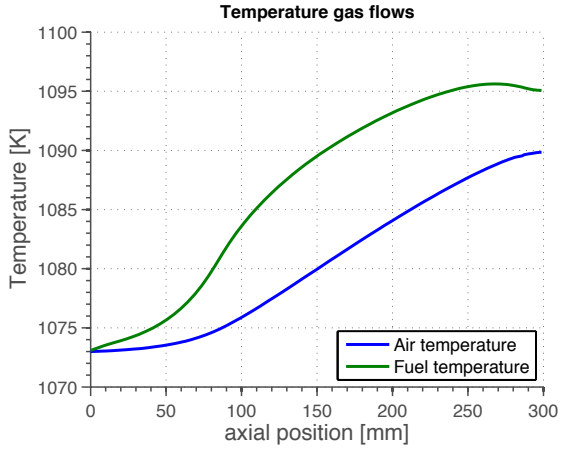

Figure 6.9: Temperature air and fuel flow

fuel cell.

6.9. REMARKS

Although the 'SOFC with Unresolved Electrolyte' add-on lumps the reaction areas and electrolyte onto one interface, the equations used in this model more accurately describe the fuel cell phenomena. A big advantage of the reactions happening on an interface is that the Nernst equation can be used to calculate the ideal potential. This means both the potential and the current density are dependent of gas composition.

As mentioned the models becomes unstable when increasing the external load above 2 [A]. One of the reason for instability could be skewed cells in the grid. It is possible that the instability has a physical reason. Specifying the current output forces the model to consume a specific amount of hydrogen and oxygen. At high output currents the reaction becomes diffusion limited in practice, or in fuel cell terminology, the concentration polarization increases. Since the anode is relatively thick the mass diffusion can be a serious limitation. To check whether this a problem in current model the permeability and porosity can be increased. It would also be interesting to see how the fuel cell performs in practice.

7

CONCLUSIONS AND RECOMMENDATIONS

This study was a first step in detailed research of radiative heat transfer in solid oxide fuel cells. The effect of thermal radiation in the porous layers of the PEN-structure was studied, and also the effect of participating gases, and the effect of surface-to-surface radiation in the gas channels.

This has lead to a number of conclusions which will be discussed here. There are also a number of recommendations for further research.

7.1. CONCLUSIONS

CFD MODELING OF SOFCS

Two different fuel cell add-on modules were used in this thesis. The 'Fuel Cell and Electrolysis' module was initially developed to model PEM fuel cells. The 'SOFC with Unresolved Electrolyte' module was developed to model the Siemens Westinghouse tubular SOFC. Although this second module simplifies the geometry, the equations more accurately describe fuel cell phenomena. Important remaining uncertainties in the CFD-models concern:

- Constant open cell voltage

The 'Fuel Cell and Electrolysis' module captures the geometry accurate, including reaction zones and the electrolyte in the domain. However instead of calculating the ideal voltage using the Nernst equation a constant value must be specified, which introduces inaccuracy in the results.

- Exchange current density

The exchange current density, i_0, represents the reaction rate at the electrodes at equilibrium conditions, and can be described using an Arrhenius like reaction rate equation. However this value is specified as a constant in the current models. More accurate results will be obtained when making this parameter temperature dependent.

- Species diffusion

Another uncertainty is species diffusion. Diffusion coefficients are determined using generalized Fick's law, binary diffusion coefficients with Chapman-Enskog. It is known that diffusion coefficients will be lower in porous media due to interaction with solid material. Although a correction method is used in the current models for the diffusion coefficients in the anode and cathode it is known that the most accurate way to determine diffusion coefficients in these materials is by using the dusty gas model (DGM). Since the modeling results are sensitive to species diffusion it is necessary to check the accuracy of the current methods.

- SOFC material properties are not well known

The uncertainty of material properties is universal for all SOFC modeling efforts. Generally the most reasonable properties are used obtained from literature.

RADIATIVE HEAT TRANSFER

The effect of thermal radiation in the PEN-structure was studied at first using simplified 2D-models. It was found that due to the high optical thickness of the anode and cathode these materials can be considered opaque. It was also shown that radiative heat transfer in the electrolyte has a negligible effect on the temperatures in the PEN-structure. This leads to the conclusion that radiation in the PEN-structure materials can be completely neglected.

A more detailed 2D model was developed to study the effect of thermal radiation in the flow channels of a planar cell. In this model uniform heat sources were used to account for the electrochemical reactions and irreversibilities. For both a counter-flow and a co-flow situation it was shown that thermal radiation has a very small effect on the temperature profiles in the domain. It was also shown that the influence of the anode and cathode surface emissivities is very small. Considering the PEN-structure materials as participating in radiative heat transfer gives similar results compared to only including surface-to-surface radiation. This confirms the previous conclusion that the PEN-structure can be considered opaque.

Because of the simplifications in the 2D-models a more detailed model was developed to obtain more accurate results. A 3D-model of a single channel planar cell was developed, using the 'Fuel Cell and Electrolysis' add-on module from Ansys Fluent to model all relevant fuel cell phenomena. The results showed that assuming uniform heat sources is a wrong assumption. The effect of surface-to-surface radiation was again found to be minimal, and the effect of participating gases completely negligible. This leads to the conclusion that radiative heat transfer can be completely neglected in single channel planar SOFCs.

The literature study showed that thermal radiation cannot be neglected in tubular SOFCs based on the Siemens Westinghouse design. In this study a 3D model of a tubular SOFC was developed, however based on a different design. This model is not functioning optimally yet, and thermal radiation has net yet been studied. Due to temperature gradients in radial direction it is expected that radiative heat transfer has a slightly larger effect on this design than on single channel planar SOFCs.

Another interesting problem not addressed in this thesis is radiative heat transfer from the fuel cell stack to the surroundings. Past research shows that his effect cannot be neglected when studying the thermal behavior of a stack. These heat losses will cause the temperatures near the boundaries of the stack to be lower and this influences the fuel cell performance.

TEMPERATURE GRADIENTS

The largest temperature gradients occur in the direction of the flow, i.e. the direction parallel to the PEN-structure. The largest amount of heat is released at areas where the hydrogen concentration is maximal. The largest temperature gradients therefore occur at the reaction areas near the fuel flow inlet. These temperature gradients can cause thermal stresses when the load of the fuel cell is varied.

During this research it was found that the heat of reaction is often determined for the overall reaction between H_2 and O_2. In literature this overall reaction heat source is often located at the reaction area of the anode side. This is also the case in the 3D planar cell model developed in this thesis. However, during this research was found that the single-electrode reaction at the anode should be in fact endothermic while the heat source at the cathode is strongly exothermic. This means it is more accurate to place the overall heat of reaction at the cathode side. It is not expected that changing the location of this heat source in the current models will result in different conclusions with respect to radiation effects or with respect to temperature gradients.

7.2. RECOMMENDATIONS

Although radiative heat transfer effects are found to be weak the following aspects deserve attention.

PLANAR VERSUS TUBULAR

It is expected that thermal radiation in the tubular cell has a larger effect than on the planar SOFC. However this model is not working optimal yet. It is recommended to continue the development of this model. Validation of this model will be possible with experimental measurements (when available).

REACTION HEAT SOURCE LOCATION

It is recommended to place the reaction heat source at the cathode instead of the anode reaction area. It would be even more accurate to determine the heat sources associated with the single-electrode reactions.

FUEL

Only hydrogen is considered as fuel in this study. Including methane adds a number of reactions including methane steam-reforming, which is a strong endothermic reaction located in the anode. Larger temperature gradients will occur compared to hydrogen fueled SOFCs, which means radiation effects can become more important.

POROUS MEDIA RADIATIVE HEAT TRANSFER

An important limitation of the 3D-models is that radiative heat transfer in porous media could not be modeled properly using the current version of Ansys Fluent. For future research where radiation in porous media must be modeled accurately, it is necessary to investigate whether this problem can be solved when using Ansys Fluent. Another solution is to look for different software packages of to develop an own CFD code.

RESOLVED OR UNRESOLVED ELECTROLYTE

If fuel cells are to be modeled using one of the discussed add-on modules, it is recommended to use the 'SOFC with Unresolved Electrolyte' module. Since the reaction areas and electrolyte are generally very thin compared to other dimensions the geometry simplifications are reasonable.

CFD-PLATFORM

The available modules in Fluent have been developed for specific fuel cell types. It is not at all straightforward to use these models effectively for other designs. To obtain complete control and have the ability to adjust all model equations it is recommended to start developing an own original CFD code, e.g. in OpenFoam. The add-on modules in Fluent require special licenses. A big limitation during this project was the availability of only two licenses, which meant a maximum of 2 cases at the same time. Development of an own code will give more freedom, allows for complete adjustment of the set of equations, and the ability to share models without the necessity of special licensed software.

BIBLIOGRAPHY

[1] Inc. EG&G Technical Services. *Fuel Cell Handbook*. U.S. DOE, National Energy Technology Laboratory, 7th edition edition, November 2004.

[2] S. C. Singhal. Solid oxide fuel cells: Past, present and future. In John T.S. Irvine and Paul Connor, editors, *Solid Oxide Fuel Cells: Facts and Figures*, Green Energy and Technology, pages 1–23. Springer London, 2013.

[3] J. Weissbart and R. Ruka. A solid electrolyte fuel cell. *Journal of The Electrochemical Society*, 109(8): 723–726, 1962.

[4] J. Larminie and A. Dicks. *Fuel Cell Systems Explained*. J. Wiley, 2003. ISBN 9780768012590.

[5] S. A. Hajimolana, M. A. Hussain, W. M. A. W. Daud, M. Soroush, and A. Shamiri. Mathematical modeling of solid oxide fuel cells: A review. *Renewable and Sustainable Energy Reviews*, 15(4):1893–1917, MAY 2011. ISSN 1364-0321.

[6] Lieh-Kwang Chiang, Hui-Chung Liu, Yao-Hua Shiu, Chien-Hsiung Lee, and Ryey-Yi Lee. Thermo-electrochemical and thermal stress analysis for an anode-supported {SOFC} cell. *Renewable Energy*, 33(12):2580 – 2588, 2008. ISSN 0960-1481.

[7] A. Nakajo, C. Stiller, G. Härkegård, and O. Bolland. Modeling of thermal stresses and probability of survival of tubular {SOFC}. *Journal of Power Sources*, 158(1):287 – 294, 2006. ISSN 0378-7753.

[8] M.F. Modest. *Radiative Heat Transfer*. Elsevier Science, 2013. ISBN 9780123869906.

[9] B. Rousseau, H. Gomart, Domingos De Sousa Meneses, Patrick Echegut, Mathilde Rieu, Romain Dugas, Pascal Lenormand, and Florence Ansart. Modelling of the radiative properties of an opaque porous ceramic layer. *Journal of Electroceramics*, 27(2):89–92, OCT 2011. ISSN 1385-3449.

[10] Pablo Rubiolo and Jean-Marie Gatt. Modeling of the radiative contribution to heat transfer in porous media composed of spheres or cylinders. *International Journal of Thermal Sciences*, 41(5):401 – 411, 2002. ISSN 1290-0729.

[11] J. Taine, F. Bellet, V. Leroy, and E. Iacona. Generalized radiative transfer equation for porous medium upscaling: Application to the radiative fourier law. *International Journal of Heat and Mass Transfer*, 53 (19-20):4071 – 4081, 2010. ISSN 0017-9310.

[12] Jean Taine and Estelle Iacona. Upscaling Statistical Methodology for Radiative Transfer in Porous Media: New Trends. *JOURNAL OF HEAT TRANSFER-TRANSACTIONS OF THE ASME*, 134(3), MAR 2012. ISSN 0022-1481.

[13] M. Tancrez and J. Taine. Direct identification of absorption and scattering coefficients and phase function of a porous medium by a monte carlo technique. *International Journal of Heat and Mass Transfer*, 47(2):373 – 383, 2004. ISSN 0017-9310.

[14] S.C. Singhal. Advances in solid oxide fuel cell technology. *Solid State Ionics*, 135(1–4):305 – 313, 2000. ISSN 0167-2738. Proceedings of the 12th International Conference on Solid State.

[15] S. Murthy and A.G. Fedorov. Radiation heat transfer analysis of the monolith type solid oxide fuel cell. *Journal of Power Sources*, 124(2):453–458, NOV 24 2003. ISSN 0378-7753.

[16] K.J. Daun, S.B. Beale, F. Liu, and G.J. Smallwood. Radiation heat transfer in planar SOFC electrolytes. *Journal of Power Sources*, 157(1):302–310, JUN 19 2006. ISSN 0378-7753.

[17] D.L. Damm and A.G. Fedorov. Spectral radiative heat transfer analysis of the planar sofc. *Journal Of Fuel Cell Science And Technology*, 2(4):258–262, NOV 2005. ISSN 1550-624X. ASME International Mechanical Engineering Congress, Anaheim, CA, NOV 13-19, 2004.

[18] Jeffrey I. Eldridge, Charles M. Spuckler, and James R. Markham. Determination of scattering and absorption coefficients for plasma-sprayed yttria-stabilized zirconia thermal barrier coatings at elevated temperatures. *Journal of the American Ceramic Society*, 92(10):2276–2285, 2009. ISSN 1551-2916.

[19] V.M. Janardhanan and O. Deutschmann. Numerical study of mass and heat transport in solid-oxide fuel cells running on humidified methane. *Chemical Engineering Science*, 62(18–20):5473 – 5486, 2007. ISSN 0009-2509. 19th International Symposium on Chemical Reaction Engineering - From Science to Innovative Engineering ISCRE-19.

[20] Norman F. Bessette, William J. Wepfer, and Jack Winnick. A mathematical model of a solid oxide fuel cell. *Journal of The Electrochemical Society*, 142(11):3792–3800, 1995.

[21] Junxi Jia, Abuliti Abudula, Liming Wei, Renqiu Jiang, and Shengqiang Shen. A mathematical model of a tubular solid oxide fuel cell with specified combustion zone. *Journal of Power Sources*, 171(2):696 – 705, 2007. ISSN 0378-7753.

[22] M Karcz. From 0d to 1d modeling of tubular solid oxide fuel cell. *Energy Conversion and Management*, 50(9):2307 – 2315, 2009. ISSN 0196-8904.

[23] Hong Liu, Jinliang Yuan, and Bengt Sunden. Thermal radiation and effects on transport processes in solid oxide fuel cells. *Heat Transfer Research*, 39(5):453–467, 2008. ISSN 1064-2285.

[24] Zuopeng Qu, P.V. Aravind, N.J.J. Dekker, A.H.H. Janssen, N. Woudstra, and A.H.M. Verkooijen. Three-dimensional thermo-fluid and electrochemical modeling of anode-supported planar solid oxide fuel cell. *Journal of Power Sources*, 195(23):7787 – 7795, 2010. ISSN 0378-7753. Selected Papers from the, Eleventh Grove Fuel Cell Symposium London, United Kingdom and Selected Papers from E-Mrs Spring Meeting 2009, Strasbourg, France.

[25] D. Sanchez, R. Chacartegui, A. Munoz, and T. Sanchez. Thermal and electrochemical model of internal reforming solid oxide fuel cells with tubular geometry. *Journal of Power Sources*, 160(2, SI):1074–1087, OCT 6 2006. ISSN 0378-7753.

[26] C Stiller, B Thorud, S Seljebo, O Mathisen, H Karoliussen, and O Bolland. Finite-volume modeling and hybrid-cycle performance of planar and tubular solid oxide fuel cells. *Journal of Power Sources*, 141(2): 227–240, MAR 1 2005. ISSN 0378-7753.

[27] Francesco Calise, Massimo Dentice d'Accadia, and Giulio Restuccia. Simulation of a tubular solid oxide fuel cell through finite volume analysis: Effects of the radiative heat transfer and exergy analysis. *International Journal of Hydrogen Energy*, 32(17):4575 – 4590, 2007. ISSN 0360-3199. Fuel Cells.

[28] Gianfranco DiGiuseppe. Surface-to-Surface Radiation Exchange Effects in a 3D SOFC Stack Unit Cell. *Journal Of Fuel Cell Science And Technology*, 9(6), DEC 2012. ISSN 1550-624X.

[29] R. Suwanwarangkul, E. Croiset, M.D. Pritzker, M.W. Fowler, P.L. Douglas, and E. Entchev. Mechanistic modelling of a cathode-supported tubular solid oxide fuel cell. *Journal of Power Sources*, 154(1):74 – 85, 2006. ISSN 0378-7753.

[30] D.L. Damm and A.G. Fedorov. Radiation heat transfer in sofc materials and components. *Journal of Power Sources*, 143(1-2):158–165, APR 27 2005. ISSN 0378-7753.

[31] J. D. VanderSteen and J. G. Pharoah. Modeling radiation heat transfer with participating media in solid oxide fuel cells. *Journal of Fuel Cell Science and Technology*, 3(1):62–67, 07 2005.

[32] A. Hirano, M. Suzuki, and M. Ippommatsu. Evaluation of a new solid oxide fuel cell system by non-isothermal modeling. *Journal of The Electrochemical Society*, 139(10):2744–2751, 1992.

[33] S. A. Hajimolana, M. A. Hussain, M. Soroush, W. M. A. Wan Daud, and M. H. Chakrabarti. Modeling of a Tubular-SOFC: The Effect of the Thermal Radiation of Fuel Components and CO Participating in the Electrochemical Process. *Fuel Cells*, 12(5):761–772, OCT 2012. ISSN 1615-6846.

[34] Comas Haynes and William J. Wepfer. Characterizing heat transfer within a commercial-grade tubular solid oxide fuel cell for enhanced thermal management. *International Journal of Hydrogen Energy*, 26 (4):369 – 379, 2001. ISSN 0360-3199.

[35] E. Achenbach. Three-dimensional and time-dependent simulation of a planar solid oxide fuel cell stack. *Journal of Power Sources*, 49(1–3):333 – 348, 1994. ISSN 0378-7753. Proceedings of the Third Grove Fuel Cell Symposium The Science, Engineering and Practice of Fuel Cells.

[36] T. Tanaka, Y. Inui, A. Urata, and T. Kanno. Three dimensional analysis of planar solid oxide fuel cell stack considering radiation. *Energy Conversion and Management*, 48(5):1491 – 1498, 2007. ISSN 0196-8904. doi: http://dx.doi.org/10.1016/j.enconman.2006.11.019.

[37] A. Gebregergis, P. Pillay, D. Bhattacharyya, and R. Rengaswemy. Solid oxide fuel cell modeling. *Industrial Electronics, IEEE Transactions on*, 56(1):139–148, Jan 2009. ISSN 0278-0046.

[38] D.J. Hall and R.G. Colclaser. Transient modeling and simulation of a tubular solid oxide fuel cell. *Energy Conversion, IEEE Transactions on*, 14(3):749–753, Sep 1999. ISSN 0885-8969.

[39] N. Lu, Q. Li, X. Sun, and M.A. Khaleel. The modeling of a standalone solid-oxide fuel cell auxiliary power unit. *Journal of Power Sources*, 161(2):938 – 948, 2006. ISSN 0378-7753.

[40] Tomoyuki Ota, Michihisa Koyama, Ching ju Wen, Koichi Yamada, and Hiroshi Takahashi. Object-based modeling of sofc system: dynamic behavior of micro-tube sofc. *Journal of Power Sources*, 118(1–2):430 – 439, 2003. ISSN 0378-7753. Scientific Advances in Fuel Cell Systems.

[41] S. Campanari and P. Iora. Definition and sensitivity analysis of a finite volume sofc model for a tubular cell geometry. *Journal of Power Sources*, 132(1–2):113 – 126, 2004. ISSN 0378-7753.

[42] Wei Jiang, Ruixian Fang, Jamil A. Khan, and Roger A. Dougal. Parameter setting and analysis of a dynamic tubular {SOFC} model. *Journal of Power Sources*, 162(1):316 – 326, 2006. ISSN 0378-7753.

[43] PW Li and MK Chyu. Simulation of the chemical/electrochemical reactions and heat/mass transfer for a tubular SOFC in a stack. *Journal of Power Sources*, 124(2):487–498, NOV 24 2003. ISSN 0378-7753.

[44] Debangsu Bhattacharyya, Raghunathan Rengaswamy, and Caine Finnerty. Dynamic modeling and validation studies of a tubular solid oxide fuel cell. *Chemical Engineering Science*, 64(9):2158 – 2172, 2009. ISSN 0009-2509.

[45] Valery A. Danilov and Moses O. Tade. A cfd-based model of a planar {SOFC} for anode flow field design. *International Journal of Hydrogen Energy*, 34(21):8998 – 9006, 2009. ISSN 0360-3199.

[46] *ANSYS Fluent Fuel Cell Modules Manual*. ANSYS, inc, release 15.0 edition, November 2013.

[47] E.J. Henley, J.D. Seader, and D.K. Roper. *Separation Process Principles*. Wiley, 2011. ISBN 9780470646113.

[48] H. J. Merk. The macroscopic equations for simultaneous heat and mass transfer in isotropic, continuous and closed systems. *Flow Turbulence and Combustion*, 8:73–99, 1959.

[49] L. Ma, D. B. Ingham, M. Pourkashanian, and E. Carcadea. Review of the computational fluid dynamics modeling of fuel cells. *Journal of Fuel Cell Science and Technology*, 2(4):246–257, 04 2005.

[50] J.O. Hirschfelder, C.F. Curtiss, R.B. Bird, and University of Wisconsin. Theoretical Chemistry Laboratory. *Molecular theory of gases and liquids*. Structure of matter series. Wiley, 1954. ISBN 9780471400653.

[51] B. Todd and J.B. Young. Thermodynamic and transport properties of gases for use in solid oxide fuel cell modelling. *Journal of Power Sources*, 110(1):186 – 200, 2002. ISSN 0378-7753.

[52] T.F. Smith, Z.F. Shen, and J.N. Friedman. Evaluation of coefficients for the weighted sum of gray gases model. *Journal Of Heat Transfer - Transactions Of The ASME*, 104(4):602–608, 1982.

[53] Alexis Coppalle and Pierre Vervisch. The total emissivities of high-temperature flames. *Combustion and Flame*, 49(1–3):101 – 108, 1983. ISSN 0010-2180.

[54] M.K. Denison and B.W. Webb. A spectral line-based weighted-sum-of-gray-gases model for arbitrary rte solvers. *Journal Of Heat Transfer - Transactions Of The AMSE*, 115(4):1004–1012, November 1993. ISSN 0022-1481.

[55] J.H. Ferziger and M. Peric. *Computational Methods for Fluid Dynamics*. Springer Berlin Heidelberg, 2001. ISBN 9783540420743.

[56] *Ansys FLUENT Theory Guide*. ANSYS, inc, release 14.5 edition, October 2012.

[57] Katharina Fischer and Joerg R. Seume. Location and magnitude of heat sources in solid oxide fuel cells. *Journal of Fuel Cell Science and Technology*, 6(1):011002–011002, 11 2008.

[58] P Costamagna, A. Selimovic, and M.D. Borghi. Electrochemical model of the integrated planar solid oxide fuel cell (ip-sofc). *Chemical Engineering Journal*, 102(1):61 – 69, 2004. ISSN 1385-8947.

[59] Zuopeng Qu, P. V. Aravind, S. Z. Boksteen, N. J. J. Dekker, A. H. H. Janssen, N. Woudstra, and A. H. M. Verkooijen. Three-dimensional computational fluid dynamics modeling of anode-supported planar SOFC. *International Journal of Hydrogen Energy*, 36(16):10209–10220, AUG 2011. ISSN 0360-3199.

[60] S.I. Sandler. *Chemical, Biochemical, and Engineering Thermodynamics*. Number v. 1 in Chemical, Biochemical, and Engineering Thermodynamics. John Wiley & Sons, 2006. ISBN 9780471661740.

A

ELECTROCHEMISTRY

Some fundamental fuel cell theory will be discussed in this appendix. The ideal potential (Nernst) potential and the Butler-Volmer equation are important equations when modeling SOFCs. There origins will be discussed.

A.1. NERNST VOLTAGE

The Nernst equation can be derived from basic thermodynamics. For any process occurring at constant temperature and pressure, the manner in which fuel cells are operated, the maximum amount of work that can be obtained is equal to the change of Gibbs energy of the process [60], shown in equation (A.1).

$$W^{max} = \Delta G \tag{A.1}$$

The maximum work is obtained when the reactions are sufficiently slow to have an irreversible process. This implies that the electrical potential produced is just balanced by an external potential, making the current infinitely small. This potential can be referred to as zero-current cell potential, open-cell voltage, or electromotive driving force. Work done by a flow of electrical energy can be expresses as:

$$W_{elec} = \pm EI \tag{A.2}$$

Where it is convention to use a positive sign if work is done on the system and a negative sign if the system is a source of electrical energy. The work done in moving n moles electrons across a potential difference E is given by:

$$W_{elec} = -nFE \tag{A.3}$$

Where F = 96485 [C/mol] is the Faraday constant, which is the magnitude of electric charge of a mole of electrons. Combining these two equations gives:

$$W_{elec} = \Delta G = -nFE \tag{A.4}$$

The Gibbs energy of any species can be written as:

$$G_i(T,P,x) = G_i^0(T,P^0,x_i^0) + RT\ln\left(\frac{f_i(T,P,x)}{f_i^0(T,P^0,x_i^0)}\right) \tag{A.5}$$

Where f_i^0 and G_i^0 are the standard state fugacity and Gibbs energy of species i.

The fugacity of a real gas can be determined using equations of state or an activity coefficient model. In solid oxide fuel cells it is however common to assume all gases to behave like ideal gases. This is reasonable because of the high temperatures and moderate pressures. Fugacity can be thought of as a 'corrected' partial pressure, correcting the ideal gas partial pressure with real gas effects. For an ideal gas the fugacity is thus equal to the partial pressure.

$$f_i = P_i \tag{A.6}$$

For a general reaction:

$$\alpha A + \beta B \rightleftharpoons cC + \delta D\,, \tag{A.7}$$

The Gibbs energy change of reaction is given by:

$$\Delta G = cG_c + \delta G_D - \alpha G_A - \beta G_B\,. \tag{A.8}$$

Substituting equation (A.5) and using the relation in equation (A.6) results in:

$$\Delta G = \Delta G^0 + RT \ln\left(\frac{p_C^c p_D^\delta}{p_A^\alpha P_B^\beta}\right) \tag{A.9}$$

Where ΔG^0 is the standard Gibbs energy change of reaction at $T = 298\ [K]$. The following definition for partial pressure can be subsituted into equation (A.9) to use concentrations instead of pressures.

$$p_i = x_i P \tag{A.10}$$

Equation (A.4) can be subtituted to obtain an expression for the potential.

$$E = \frac{\Delta G}{nF} + \frac{RT}{nF} \ln\left(\frac{p_C^c p_D^\delta}{p_A^\alpha P_B^\beta}\right) \tag{A.11}$$

Where :

$$\frac{\Delta G}{nF} = E^0 \tag{A.12}$$

E_0 the ideal standard potential at $T = 298\ K$. For a fuel cell in which O_2 and H_2 react $E^0 = 1.229\ [V]$ with liquid water product and $E^0 = 1.18\ [V]$ [1]. The difference between those values is the Gibbs energy change of vaporisation at standard conditions. Since SOFC operate under high temperature the water product will always be in gaseous state. For a fuel cell with only H_2 and O_2 the reaction is given by:

$$H_2 + 1/2 O_2 \rightleftharpoons H_2O\,. \tag{A.13}$$

The amount of electrons per oxidized hydrogen atom is 2. The Nernst voltage can be determined with:

$$E = E^0 + \frac{RT}{2F} \ln\left(\frac{p_{H_2} p_{O_2}^{1/2}}{P_{H_2O}}\right) \tag{A.14}$$

This Nernst equation gives ideal open cell voltage and thus represents the maximum achievable by the cell. The real cell voltage will be lower due to reversibilities, which will be discussed in the next section.

In the CFD-code the Nernst voltage is determined locally at the reaction areas, since the temperature, pressure and concentrations vary internally in a fuel cell.

A.2. ACTUAL PERFORMANCE AND CELL EFFICIENCY

The maximum amount of electrical work delivered is given by the change in Gibbs free energy. The efficiency is determined by comparing the electrical energy produced with the heat that would be produced by burning the fuel [4]. This implies that the maximum efficiency is given by equation (A.15).

$$\eta_{max} = \frac{\Delta G}{\Delta H_f} \times 100\% \tag{A.15}$$

Where ΔH_f is the change in 'enthalpy of formation'. The efficiency can be determined using the higher heating value (HHV) or the lower heating value (LHV). The difference between those two is the molar enthalpy of vaporisation of water. Any statement of efficiency should notice whether it is determined using the HHV or the LHV. If it is not given probably the LHV is used since this results in higher efficiency. Since the fuel cells studies in this thesis are high temperature the water vapor will always exit in gaseous state, which means the LHV should be used. For the reaction given in equation (A.13), $\Delta H_f = -241.83\ [kJ/mol]$.

The maximum efficiency as function of temperature is shown in figure A.1a.

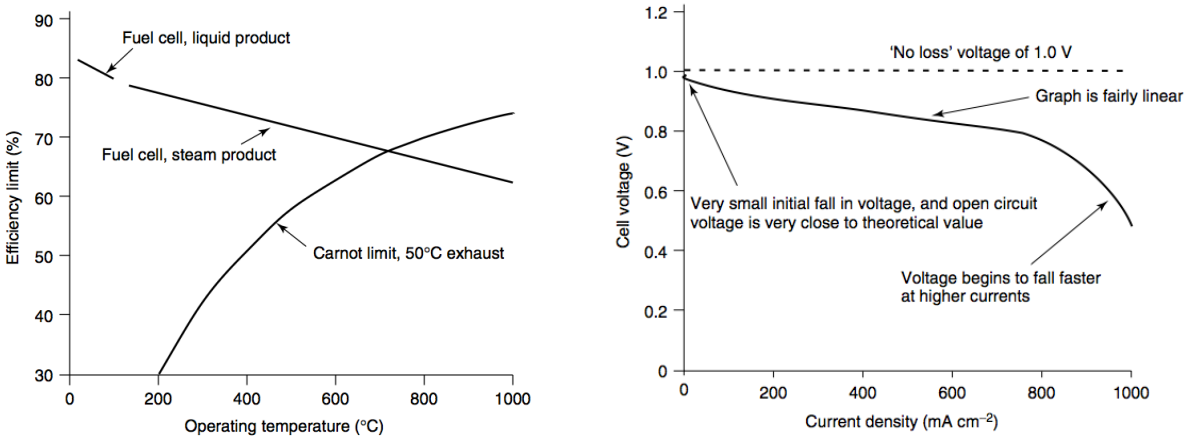

(a) (b)

Figure A.1: (a)Maximum efficiency as function of temperature. Carnot efficiency shown for comparison with $50^{\circ}C$ exhaust temperature. (b) Voltage as function of current density for typical air-pressure operating fuel cell at $800^{\circ}C$ [4].

There are two fuel cell efficiency curves, the liquid product and gaseous product curve. The first one is bases on the HHV and the second one on the LHV. Both curves are compared to the Carnot efficiency with an lower temperature of $T_L = 50[^{\circ}C]$.

The actual voltage of a hydrogen fuel cell operating at $800[^{\circ}C]$ is shown in Fig. A.1b. From this figure it is clear that there is a considerable difference between the ideal (reversible) voltage and the actual voltage, especially at high current density. This is causes by four major irreversibilities in the system which will be explained here.

A.2.1. ACTIVATION LOSSES

Activation losses (or activation overpotential or overvoltage) represent the potential difference generated at an electrode interface. These losses are caused by slowness of the reactions taking place at the electrode surface. This potential difference drives the chemical reaction that transfers electrons to or from the electrode. The activation overpotential is in a non-linear way related to the current density. Tafel observed and reported in 1905 that overvoltage at the surface of an electrode follows a similar pattern for a great variety of electrochemical reactions [4]. This observations are a result of experiments, rather than theoretical observations. For most values of overvoltage its value can be determined with:

$$\eta = A \ln\left(\frac{i}{i_0}\right) \tag{A.16}$$

Where the overvoltage η is the difference between the electrode potential and the electrode equilibrium potential. The constant A is given by:

$$A = \frac{RT}{n\alpha F} \tag{A.17}$$

where α is the charge transfer coefficient. The current density i_0 is the exchange current density. At equilibrium the forward and backward rates of the reactions are equal, in this situation the exchange current density represent the continuous backwards and forwards flow from and to the electrolyte. A high exchange current density means that the surface of the electrode is more 'active', which means the flow of electrons in a particular direction is more likely. In the development of fuel cell electrodes it is vital to make this value as high as possible.

The Tafel equation can be rearranged to give the current instead of the voltage. This results in:

$$i = i_0 \exp\left(\frac{2\alpha F \Delta\eta}{RT}\right). \tag{A.18}$$

This equations holds for high overpotential regions. At lower overpotential regions it was found that the current is influenced by both anodic and cathodic reactions. With other words to accurately predict the current

density in one electrode, the electrochemistry in the other electrode must also be taken into account. This has led to the Butler-Volmer equation:

$$i = i_0 \exp\left(\frac{(1-\alpha)\cdot n\cdot F}{RT}\eta\right) - i_0 \exp\left(-\frac{(\alpha)\cdot n\cdot F}{RT}\eta\right) \tag{A.19}$$

This equation is generally used to relate the current density and the overpotential to each other. The term i_0 is the current density at zero overpotential. Temperature dependence of this term is described using Arrhenius like equations. The current density is also depending on concentration, this dependence can be included in the expression i_0 or in equation (A.19).

A.3. HEAT SOURCES

Heat is released in SOFCs due to electrochemical reactions and irreversibilities. How to determine these heat sources and where they are located will be discussed in this section.

HEAT OF REACTION

The overall reaction is given by:

$$H_2 + \frac{1}{2}O_2 \leftrightarrow H_2O \tag{A.20}$$

The enthalpy change of reaction at standard conditions is $\Delta_R H = -241$ [kJ/mol]. At elevated temperatures the enthalpy values of the different species can be determined using:

$$\Delta_R H(T) = \Delta_R H(T_{ref}) + \int_{T_{ref}}^{T} \Delta C_p(T')dT' \tag{A.21}$$

This can be used to determine the enthalpy change of the overall reaction at all temperatures. The heat capacities are temperature dependent and can be obtained from for example NIST Webbook. This will give an overall enthalpy change of reaction. However, two half-reactions occur in the fuel cell domain. It is difficult to obtain the heat of reaction of the single-electrode reactions since the relation between state variables of electrons and oxygen ions is not known.

There is an empirical method available to estimate the heat sources associated with the single-electrode reactions, namely an analysis using Seebeck coefficients [57].

SEEBECK COEFFICIENT ANALYSIS

From experiments was found that there is a linear relationship between the electromotive force (EMF) and temperature of the electrodes. This ratio $\Delta E/\Delta T$ is the Seebeck coefficient. Single electrode entropy values can be estimated from Seebeck coefficients, which can be experimentally determined. This method requires no knowledge of single ionic species. From this linear relationship between the EMF and the temperature difference an expression for the transported entropy of oxygen ions can be deduced:

$$\frac{\Delta E}{\Delta T} = \frac{1}{2F}\left[-\frac{1}{2}S_{O_2} - 2S^*_{e^-} + S^*_{O^{2-}}\right] = \text{const} \tag{A.22}$$

An expression for the entropy change of reaction at the cathode side can be derived:

$$\Delta_R S^c(T, p_{O_2}) = \Delta_R S^c(T_{ref}, p_{O_2,ref}) + R\ln\left(\frac{p_{O_2}}{p_{O_2,ref}}\right) \tag{A.23}$$

Since the total change of entropy of the electrochemical reactions can be computed from the entropy of the species involved, the change of entropy of the half-reaction at the anode can be determined with:

$$\Delta_R S^a = \Delta_R S(T, p_i) - \Delta_R S^c \tag{A.24}$$

The seebeck coefficient reported in Fischer and Seume [57] is obtained by experiments with YSZ as electrolyte and platinum electrodes at standard pressure and an electrode temperature of 1273 [K]. This value is:

$$\frac{dE}{dT} = -0.463 \quad \left[\frac{\text{mV}}{\text{K}}\right] \tag{A.25}$$

The cathodic entropy change can be determine with:

$$\Delta_R S^c(T, p_{O_2}) = -89.3 \frac{\text{J}}{\text{mol K}} + \frac{R}{2} \ln\left(\frac{p_{O_2}}{p_0}\right) \tag{A.26}$$

The overall entropy change of reaction is:

$$\Delta_R S(1273K, p_i) = -56.7 \frac{\text{J}}{\text{molK}} + R \ln \frac{p_{H_2}\sqrt{p_{O_2}}}{p_{H_2O}\sqrt{p_0}} \tag{A.27}$$

At the end of this appendix a matlab code is included which can be used to determine the electrochemical heat sources associated with single-electrode reactions. At hydrogen partial pressure of 0.8, oxygen 0.21, and water vapor 0.2 [bar], the reaction heat sources at an current density of 4000 $[A/m^2]$ are shown in table A.1. The heat source based on the total entropy change of reaction is shown first. This is often the heat source used

Table A.1: Total reaction heat source and half-reaction heat sources

Q_{total} [W/m^3]	1.24E+09
Q_{anode} [W/m^3]	-9.81E+08
$Q_{cathode}$ [W/m^3]	2.13E+09
Q_{Fluent} [W/m^3]	1.53E+09

in a SOFC model, applied at the anode side. The half-reaction heat sources determined using the Seebeck analysis are shown next. This shows that the anode reaction is endothermic, while the cathode half-reaction is strongly exothermic. The last row shows the average volumetric heat source obtained from Fluent, for the 3D planar cell. This value is slightly higher than the total heat source calculated here, since there are areas with higher and lower current density, and the partial pressures are not constant through the domain as assumed in this simplified analysis.

OVERPOTENTIAL HEATING

These heat sources also occur in the reaction areas, where the potential is not equal to the ideal potential. This difference is used to drive the reactions but is also the reason for irreversibility. The heat released do to overpotential in both the anode and cathode side can be determined with:

$$\dot{Q}^{nc}_{act} = i \cdot \eta^c_{act} \tag{A.28}$$

$$\dot{Q}^{na}_{act} = i \cdot \eta^a_{act} \tag{A.29}$$

The overpotential is related to the current density through the Butler-Volmer equation. Assuming a current density of 4000 [A/m^2], it is possible to determine the overpotentials.

JOULE HEATING

Joule heating occurs in the materials were electrons or oxygen ions are conducted. This heat source is determined using:

$$Q'''_{\Omega} = \frac{1}{\sigma} \cdot i^2 \tag{A.30}$$

The current density squared divided by the material conductivity. A constant volumetric source is applied in each electron or oxygen ion conducting material. Since the current density profiles are not accurately known yet, uniform current density is assumed to determine this heat source.

MATLAB SCRIPT DETERMINE MAGNITUDE OF HEAT SOURCES

```
1 close all
2 clear all
3 clc
4
```

```
%Standard values at 298.15 [K]
Δ_an = 1e-6;        %[m] Thickness anode TPB
Δ_cat = 1e-6;       %[m] Thickness cathode TPB
F = 96485;              %[C/mol] Fahrenheid constant
T = 1073;               %[K] Operating temperature
j = 4000;               %[A/m2] Average Current Density
H0_O2 = 0;              %[kJ/mol] Enthalpy of formation
H0_H2 = 0;              %[kJ/mol] Enthalpy of formation
H0_H2O = -241.826;      %[kJ/mol] Enthalpy of formation
S0_H2  = 130.68;        %[J/mol/K] Standard entropy
S0_H2O = 188.84;        %[J/mol/K] Standard entropy
t = T/1000;

%O2 Enthalpy, data from NIST Webbook
%Between 700 - 2000 [K]
A1 = 30.03235;
B1 = 8.772972;
C1 = -3.988133;
D1 = 0.788313;
E1 = -0.741599;
F1 = -11.32468;
G1 = 236.1663;
H1 = 0.0;
H_O2 = H0_O2 + A1*t + B1 * t^2/2 + C1*t^3/3 + D1*t^4/4 - E1/t + F1 - H1;
S_O2 = A1*log(t) + B1*t + C1*t^2/2 + D1*t^3/3 - E1/(2*t^2) + G1;
%H2 Enthalpy, data from NIST Webbook
%Between 1000 - 2500 [K]
A2 = 18.563083;
B2 = 12.257357;
C2 = -2.859786;
D2 = 0.268238;
E2 = 1.977990;
F2 = -1.147438;
G2 = 156.288133;
H2 = 0.0;
H_H2 = H0_H2 + A2*t + B2 * t^2/2 + C2*t^3/3 + D2*t^4/4 - E2/t + F2 - H2;
S_H2 = A2*log(t) + B2*t + C2*t^2/2 + D2*t^3/3 - E2/(2*t^2) + G2;
%H2O Enthalpy, data from NIST Webbook
%Between 500 - 1700 [K]
A3 = 30.09200;
B3 = 6.832514;
C3 = 6.793435;
D3 = -2.534480;
E3 = 0.082139;
F3 = -250.8810;
G3 = 223.3967;
H3 = -241.8264;
H_H2O = H0_H2O + A3*t + B3 * t^2/2 + C3*t^3/3 + D3*t^4/4 - E3/t + F3 - H3;
S_H2O = A3*log(t) + B3*t + C3*t^2/2 + D3*t^3/3 - E3/(2*t^2) + G3;
%Heat of reaction
H_react = H_H2O - 0.5 * H_O2 - H_H2;        %[kJ/mol]
S_react = (S_H2O - 0.5 * S_O2 - S_H2);      %[J/mol/K]
G_react = H_react - T * S_react/1000;       %[kJ/mol]

Q_total_react = j/(2*F) * -T * S_react;      %[W/m^2]
Q_vol_entropy_based   = Q_total_react/1e-6   %[W/m^3] %Total reaction heat source
Q_total_enthalpy = -j/(2*F)*H_react*1000;    %[W/m^2]
Q_vol_enthalpy_based = Q_total_enthalpy/1e-6 %[W/m^3] %Total enthalpy change of rection

%Single Electrode entropy changes
%Seebeck Coefficient Based Analysis
E_T = -0.463; %[mV/K] Seebeck Coefficient from Fisher2008
%Heat source Cathode
P0 = 101325;    %[Pa]    Operating pressure
P_O2 = P0*0.21; %[Pa] Oxygen partial pressure
P_H2 = 0.8*P0;  %[Pa] Hydrogen partial pressure
P_H2O = 0.2*P0; %[Pa] Water vapor partial pressure
R = 8.314;      %Universal gas constant [J/mol/K]
Delta_S_cath = (-89.3 + R/2*log(P_O2/P0)); %Cathode half-reaction entropy change
Delta_S_Total = -56.7 + R*log((P_H2*P_O2^0.5)/(P_H2O*P0^0.5)); %Total entropy change
Delta_S_an = Delta_S_Total - Delta_S_cath; %Anode half-reaction entropy change
```

```
76 Q_an =   (-T*Delta_S_an) /1000 ;   %[kJ/mol]
77 Q_cat =   (-T*Delta_S_cath) /1000; %[kJ/mol]
78 Q_vol_an = j/(2*F) * Q_an/Δ_an *1000    %[W/m3] %Heat source anode
79 Q_vol_cat = j/(2*F) * Q_cat/Δ_cat *1000 %[W/m3] %Heat source cathode
80 %Activation polarization
81 %Estimating overpotentials using Tafel-equation
82 i0_cat = 1007;  %Exchange current density cathode
83 i0_an  = 7460;  %Exchagen current density anode
84 alpha = 0.5;    %Transfer coefficient
85 eta_an = R*T/(alpha*F) * log(j/i0_an);
86 eta_cat = -R*T/(alpha*F) * log(j/i0_cat);
87 Q_act_cat = j*eta_cat; %[W/m2]
88 Q_act_an  = j*eta_an; %[W/m2]
89 %Joule heating
90 %Electrolyte:
91
92 %Reaction heating from Fluent
93 Volume_tpb = 100e-3*3e-3*3e-6; %[m^3]
94 Q_reactionheating = 1.3745019; %[W/m^3](m^3)
95 Fluent_source = Q_reactionheating/Volume_tpb %[W/m^3]
```

B

SOLUTION PROCEDURE

For both the fuel cell addon modules a certain procedure was found which helped to obtain a converged solution. Since it took a lot of time to get the models converging this procedure is included in this appendix. This will be helpful to people who are planning to use the fuel cell modules in the future.

B.1. SOFC WITH UNRESOLVED ELECTROLYTE ADD-ON

BOUNDARY CONDITIONS

All boundary conditions must be correct. At the air and fuel inlet `mass-flow-inlet` must be used, at the air and fuel outlet `pressure-outlet`. Species concentration, temperature and mass flow must be correctly specified at the inlets. It will help convergence if species concentrations and temperatures are specified at the outlets.

The reaction areas and electrolyte are lumped onto the interface between anode and cathode. The wall must be electrochemically coupled, which is achieved when both a 'wall' and 'shadow-wall' occur in the boundary conditions list.

The interfaces between porous zones and fluid zones must be defined as '`interior`' boundary condition. Any other boundary condition will block the flow.

The external contact area of the anode current collector is called the 'voltage tap surface'. The contact area of the cathode current collector the 'current tap surface'. It is important that these areas are located on the boundaries of the computational domain. This caused problems in the tubular cell discussed in thesis, were the entire cell is surrounded by the air domain. This problem was solve by applying these external contact surfaces on the symmetry wall of the domain.

The following procedure worked for the current model:

- Make sure there are no errors in the mesh
- Double check all properties and boundary conditions
- Initialize with a guessed temperature, no velocity
- Patch fuel and anode domain with the related inlet concentrations
- Patch air and cathode domain with the related inlet concentrations
- Specify the output current as 0 [A] and let the system of equations converge without species source term and without the energy source terms
- Enable species source terms and continue iterating until convergence
- Make sure there is conservation of mass and species
- Stepwise increase the output current and let the system of equations converge until a solution is obtained for the desired current output
- When converged, enable the energy source terms and let the system of equations converge again
- If divergence occurs, try again but increase output current in smaller steps

The command '`/report/species-mass-flow`' can be used to obtain the net species balance. It must be checked whether the amount of consumed hydrogen and oxygen accounts for the correct output current.

SOLVER SETTINGS

The default solver settings in Fluent are not sufficient to obtain a converged solution. The solution is very sensitive to the settings of the species equations. If the relaxation factor is 1 the solution will diverge, but a too low relaxation can also mean that a solution will never be obtained. The solutions in the current models were obtained using 0.99. For density and body forces 0.6 was used, and for the energy discrete ordinates and potential equations 1.

The multigrid settings must also be adjusted. The Cycle type is put on F-Cycle for the flow, energy and potential equations. For all species equations V-cycle is used. The maximum number of cycles must be changed to 50. When the species equations show fluctuating behavior and become unstable the stabilization method BCGSTAB can be used.

B.2. FUEL CELL AND ELECTROLYSIS ADD-ON

At the external surfaces of the anode and cathode the boundary conditions for the potential equations are applied. At the anode current collector a potential of 0 [V] must be applied. At the cathode current collector both either a potential or a current density can be applied[1].

All boundary conditions must be correct. At the air and fuel inlet `mass-flow-inlet` must be used, at the air and fuel outlet `pressure-outlet`. Species concentration, temperature and mass flow must be correctly specified at the inlets. It will help convergence if species concentrations and temperatures are specified at the outlets.

The interfaces between porous zones and fluid zones must be defined as '`interior`' boundary condition. Any other boundary condition will block the flow. The interfaces between triple phase boundary and electrolyte must be a wall with zero species diffusion and coupled electrochemistry.

- Make sure there are no errors in the mesh
- Double check all properties and boundary conditions
- Initialize with a guessed temperature, no velocity
- Patch fuel and anode domain with the related inlet concentrations
- Patch air and cathode domain with the related inlet concentrations
- Start with much lower current density than is planned, start with Tafel-equation and disable Electrochemistry sources, joule heating and reaction heating.
- After convergence, enable species electrochemistry sources and continue iterating until convergence
- Make sure there is conservation of mass and species
- Enable Butler-Volmer and continue iteration
- Enable Joule Heating and Reaction heating and continue iterating
- Stepwise increase the output current and let the system of equations converge until a solution is obtained for the desired current output
- If divergence occurs, try again but increase output current in smaller steps

The command '`/report/species-mass-flow`' can be used to obtain the net species balance. It must be checked whether the amount of consumed hydrogen and oxygen accounts for the correct output current.

SOLVER SETTINGS

The default solver settings in Fluent are not sufficient to obtain a converged solution. The solution is very sensitive to the settings of the species equations. If the relaxation factor is 1 the solution will diverge, but a too low relaxation can also mean that a solution will never be obtained. The solutions in the current models were obtained using 0.99. For density and body forces 0.6 was used, and for the energy discrete ordinates and potential equations 1.

The multigrid settings must also be adjusted to change the convergence behavior. The Cycle type is put on F-Cycle for all equations. The maximum number of cycles must be changed to 50. When the species equations show fluctuating behavior and become unstable the stabilization method BCGSTAB can be used.

[1] The current density is applied in units [A/m^2], but note that current at the cathode side is considered negative, which means the boundary condition must carry a minus sign.